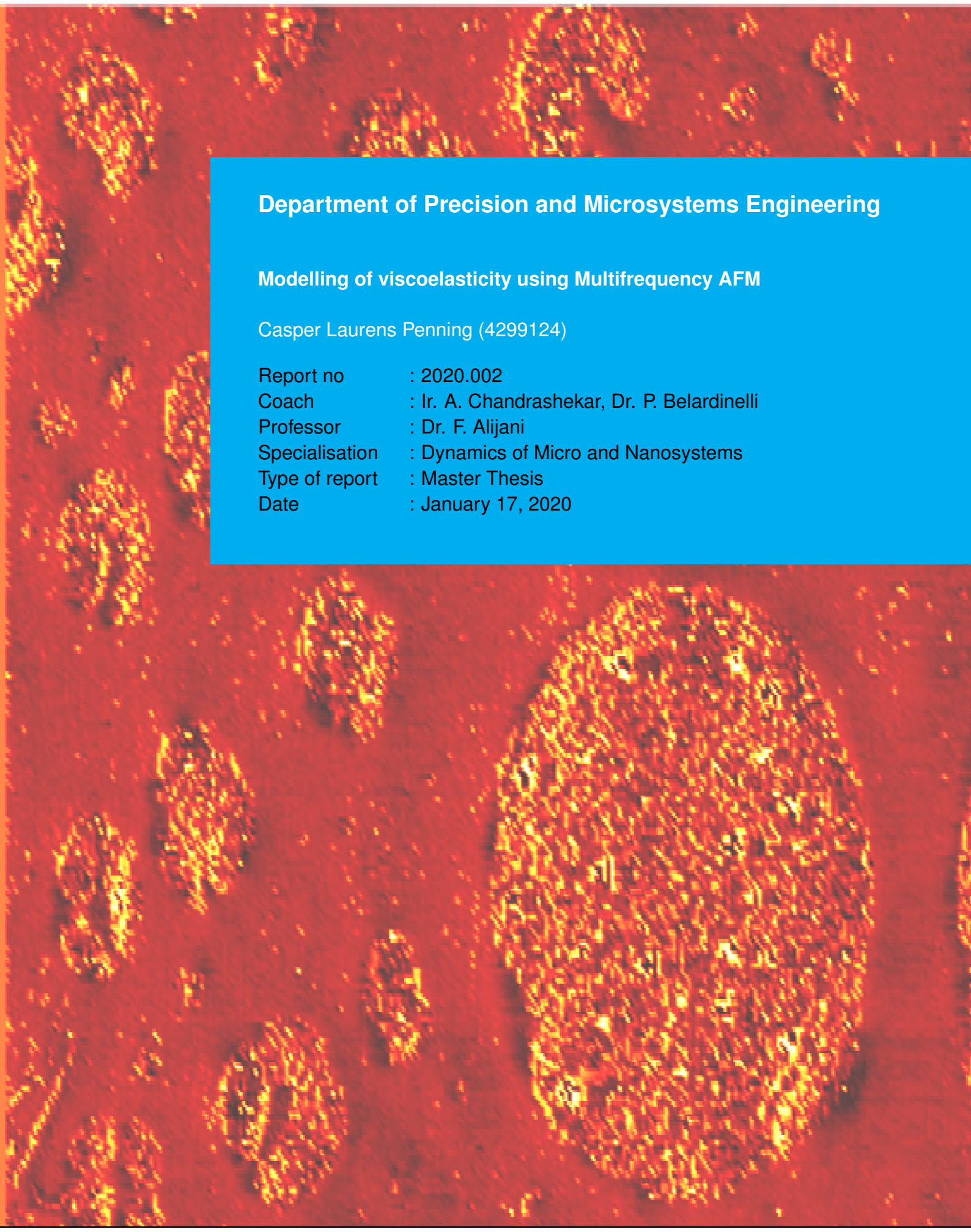

Department of Precision and Microsystems Engineering

Modelling of viscoelasticity using Multifrequency AFM

Casper Laurens Penning (4299124)

Report no : 2020.002
Coach : Ir. A. Chandrashekar, Dr. P. Belardinelli
Professor : Dr. F. Alijani
Specialisation : Dynamics of Micro and Nanosystems
Type of report : Master Thesis
Date : January 17, 2020

Cover image: Phase image of a polymer blend consisting of Polystyrene and Polyolefin Elastomer (PS-LDPE) obtained with Intermodulation AFM under ambient conditions.

Modelling of viscoelasticity using Multifrequency AFM

Department of Precision and Microsystems Engineering

by

Casper Laurens Penning

to obtain the degree of Master of Science

at the Delft University of Technology,

to be defended publicly on Tuesday January 17, 2019 at 12:45 PM.

Student number:	4299124	
Project duration:	October 4, 2018 – Januari 17, 2020	
Thesis committee:	Prof. dr. ir. P. Steeneken,	TU Delft
	Dr. F. Alijani,	TU Delft, supervisor
	Dr. M. Langelaar,	TU Delft
	Dr. P. Pahlavan,	TU Delft
	Dr. P. Belardinelli,	TU Delft, supervisor
	Ir. A. Chandrashekar,	TU Delft, supervisor

This thesis is confidential and cannot be made public until January 17, 2020.

TU Delft Delft University of Technology

Abstract

Viscoelasticity is a material property that is relevant in a variety of nanoscale materials and interfaces in medicine and industry. Therefore, a method of mechanical quantification has become exceedingly desired. In this thesis the Atomic force microscope (AFM) is applied to accurately characterize the mechanical behavior of viscoelastic samples. The goal is to enhance viscoelastic characterization using the so-called Intermodulation AFM (ImAFM) technique by applying, adapting and improving multiple modelling and optimization methods.

In ImAFM force reconstruction is performed by extracting intermodulations around resonance in the cantilever response. These intermodulations present new observables that can be used for characterization. This thesis investigates the potential of this technique in combination with an up-and-coming model describing viscoelastic interaction. A toolbox has been developed for numerical simulations of the model to resemble the experiments. The model has been evaluated in a variety of situations using sensitivity analysis in a large feasibility range, encompassing many complex dynamics. Because of the diversity in model dynamics a global optimization has been performed for experimental reconstruction.

Preface

In this Master Thesis project the work is divided in a diverse set of tasks, switching between modelling, programming and experimenting with (sub)nanoscale mechanisms and sophisticated microscope systems. As a student, the subject of atomic force microscopy has been very appealling from the start as it encompasses the many compoments of the (Art) of Mechanical Engineering practice, such as control, dynamics and signal processing. It is no coincidence that the logo of the student association of the Department of Precision and Microsystems Engineering represents a cantilever tip!

During this project I've been priveleged with the guidence of my supervisors with whom I've had discussions on a weekly basis. Abhilash, Pierpaolo and Farbod: I want to thank you for your time, your attention and your assistance during the project. I have had a great time being your student and I have learned a lot.

Casper Laurens Penning
Delft, January 2020

Contents

1 Introduction

Viscoelastic behavior is relevant for many different materials and interfaces. Nowadays, it plays an important role in medicine with nanomechanical characterization of complex cellular surfaces [1] and (artificial) biological tissue [2] such as coatings on catheters. Also, nanomechanical properties in industrial applications such as the interphases of polymer nanocomposites [3] and 2D materials are being investigated intensively. Hence, the localized viscoelastic characterization of (sub)structures are of great interest in nanometer scale environments.

Since the publication of the Atomic Force Microscope (AFM) in 1986 [4] the research on atomic and nanometer scale characterization has significantly advanced. It was invented to provide surface topography images with atomic resolution by scanning a small cantilever across a surface. While scanning, interaction forces between the cantilever's free-end tip and a surface result in a cantilever deflection which can be measured. In dynamic AFM (dAFM) variations of the dynamics of an oscillating cantilever are measured. With the development of dAFM it became possible to simultaneously obtain topography as well as mechanical property maps of the surface in a variety of operation modes. Moreover, the interaction force and friction are relatively weak in dAFM [1], making it suitable for soft and rather susceptible samples.

Although the dAFM has its obvious advantages, for cantilevers excited at one single frequency direct measurement of dissipation is impossible due to a limited number of experimental observables [5]. Furthermore, the tip-sample interaction force is highly nonlinear, causing many harmonics and lower eigenmodes to be present in the cantilever dynamics. For those reasons, so-called Multifrequency AFM methods were developed, where multiple oscillation frequencies of the cantilever motion are excitated and/or measured [6].

In this thesis a Multifrequency method is examined where the cantilever is driven at multiple frequencies closely spaced around a cantilever resonance. As a consequence of the nonlinear interaction, the cantilever dynamics will include multiple intermodulation products of the drive-frequencies. Accordingly, this technique is called intermodulation AFM (ImAFM) and was invented in 2008[7]. With multiple intermodulations, many experimental observables can be obtained in a narrow band arround resonance far above the measurment noise floor.

As the intermodulations show a high force sensitivity, viscoelastic characterization is performed through force reconstruction. The interaction between a cantilever tip and a soft material taking place at the nanometer scale will be governed by surface forces, causing local miniscus forming of a soft surface around the tip. In AFM a handfull of models of contact mechanics are extensively utilized to describe tip-sample interaction, however they fail to represent soft surfaces with low Young's Moduli [8]. As alternative, models are presented with a solid theoretical basis, describing tip-sample interaction in three dimensional field equations [9]. However, such methods are afflicted by uncertainties and many free parameters. Therefore, in this thesis a reduced model which is recently developed by Haviland et al. [10–13, 8] will be studied. The model is called 'Moving surface model'. In this model the surface dynamics is described independently, representing two-body dynamics between cantilever and surface.

1.1. Thesis Overview

The thesis is outlined as follows, Chapter 1 introduces the basiscs of the AFM system, various modes of AFM operation and gives an introduction to linear viscoelasticity and its characterization at nanoscale utilizing AFM techniques. Chapter 2 summarizes the results of the thesis in the form of a journal article and finally, chapter 3 includes the recommendations and conclusions. All modelling details and results not presented in the article are displayed in the Appendix A-D.

1.2. Fundamental workings of AFM

At the heart of every AFM is a microcantilever with a nano-sized tip at its end interacting with a sample. As a consequence of tip-surface interaction the cantilever tip will deflect from its equilibrium position. As the interaction force is highly distance dependent it is predominant locally in the very front atoms of the cantilever tip [4]. This level of sensitivity is responsible for high resolution in AFM. In general, the tip deflection is detected by focussing a laser beam on the backside of the cantilever and looking at the deviation of the reflected beam on a photodiode. Tip deflection is the essential observable that can be translated into a tip-sample interaction force or oscillation parameters in case of cantilever motion.

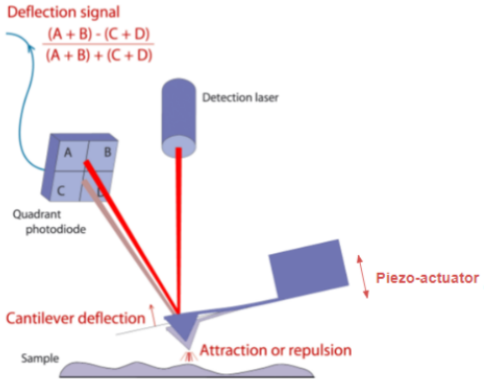

Figure 1.1: Schematic representation of a standard AFM system (adapted from Source: [14]).

Typically, the cantilever or sample position can be adjusted in x, y and z direction by means of a piezoelectric tube actuator [15]. Using feedback control, a piezo-actuator at the cantilever base can move the cantilever in order to maintain a preferred (set-point) force, oscillation amplitude or else depending on the mode of operation. By adjusting for a constant setpoint and monitoring changes in experimental observables, sample topography images and many types of local material properties can be obtained.

Fig. 1.2 gives a schematic representation of the coordinate system for AFM, in accordance with [8]. The cantilever deflection is represented by d, here chosen to be positive in the direction away from the sample. The cantilever rest position is depicted with h and the tip-surface seperation is represented by $z - z_0$, with z_0 the surface rest position often chosen at $z = 0$ such that:

$$z = h + d. \tag{1.1}$$

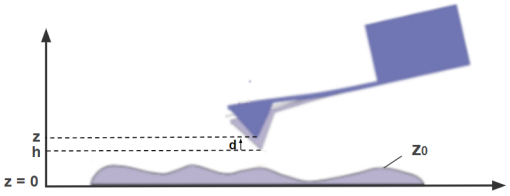

Figure 1.2: Cantilever rest position h, tip deflection d, tip-sample distance z and surface topography z_0 (adapted from Source: [14])

1.3. Tip-sample interactions

Interaction mechanics between a tip and sample is characterized by the interaction potential energy U_{ts}, which depends on the seperation distance z in Eq. 1.1. If the interaction force F_{ts} is conservative, then it can be translated through z as

$$F_{ts} = -\frac{\partial U_{ts}}{\partial z} \,. \tag{1.2}$$

The total interaction force is a combination of various force contributions. These contributions can be categorized as long or short ranged, and are known to have a particular strength [16]. Particular forces may be predominant or negligible depending on operating conditions. The operating conditions in this research will in principle be in ambient conditions. Relevant interaction forces are discussed for these environmental conditions in particular.

The devision between long -and short range forces can be interpreted in terms of microscopic and macroscopic regions of interest. These regions are represented in Fig. 1.3 as Region I and Region II, respectively. The tip can be modelled in terms of a macroscopic bulk with many atoms being far away from the sample, relative to the microscopic region of atoms closest to the surface that actually participate in short range interactions. The short-range forces acting over a microscopic Region I are generally determined by chemical forces between atoms, where in the macroscopic Region II long-range attractive Van der Waals and other electrostatic forces are active [17].

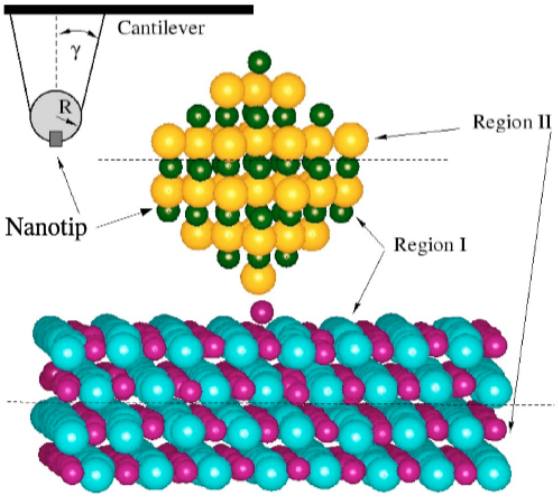

Figure 1.3 Regions of interaction between atoms in the tip, represented by green and yellow particles and atoms in the sample, represented by purple and blue particles. Region I represents a microscopic region, where Region II represents a macroscopic region (Source: [17]).

1.3.1. Total Force

The total interaction force is the sum of the long -and short range force contributions. Under normal ambient circumstances we write [18]

$$F_{\text{tot}}(z) = F_{\text{VdW}}(z) + F_{\text{electrostatic}}(z) + F_{\text{chemical}}(z). \tag{1.3}$$

Since the VdW force is always present in practice, the total tip-sample force should include a VdW force contribution [19]. In most cases the long-range electrostatic interaction can be eliminated by compensating for

the tip-surface contact-potential difference [18]. Neglecting electrostatic forces, the total force can be determined by adding the macroscopic VdW force to the short-range Lennard Jones model [20] in order to account for the long range forces between the atoms in the bulk of the tip and the bulk of the sample. For a spherical tip with radius R interacting with a flat sample, the total force is then described as:

$$F_{tot}(z) = -\frac{HR}{6z^2} + \frac{12U_0}{r_0}\left[\left(\frac{r_0}{z}\right)^{13} - \left(\frac{r_0}{z}\right)^{7}\right]. \tag{1.4}$$

In Fig. 1.4 both the long-range, short range and total force are displayed as a function of the tip-sample seperation distance. The operating force regime is determined by the sign of the interaction force that varies over the tip-sample distance. The repulsive regime describes a positive short range interaction force, whereas the attractive regime describes a negative long-range interaction force. As the interaction force is a sum of long-range and short range forces, the repulsive and attractive force regimes are predominant phenomena in tip-sample interactions.

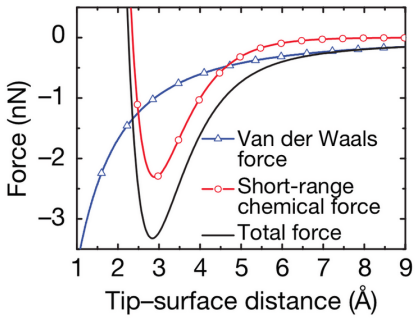

Figure 1.4 Representation of Total Force that as a combination of the long-range Van der Waals Force and short-range chemical force (Source: [21])

1.3.2. Mathematical models to simulate the cantilever and sample mechanics

As the tip approaches the sample just further than the interatomic distance a_0, the tip is roughly said to be in contact with the sample. In AFM the size of the contact region is in the order of nanometers, meaning that the area between the tip and sample surface contains tens or hundreds of atoms, all involved in the tip-surface interaction [22]. Instead of determining inter-atomic interactions individually, one normally considers bulk interaction models, regarding tip and sample to be continuum bodies. These bulk models are described by classic continuum elasticity theory involving contact mechanics as depicted in Fig. 1.5.

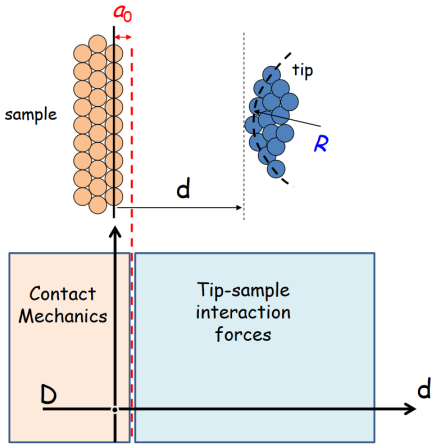

Figure 1.5 When the tip crosses the intermolecular distance a_0, tip-surface interactions are described by contact mechanics (Source: [22])

Mechanical contact results in deformations that depend on external load and material properties [15]. We can distinguish contact models that describe elastic deformations in different ways. In this section these models with their quantities of interest such as interaction force F, adhesion force F_{ad}, contact radius a, penatration depth D and work of adhesion γ, will be highlighted. The force-distance curves of the three classic elasticity models are displayed in Fig. 1.6. In modelling the tip and substrate as two different continuum bodies an Effective Young's modulus E^* is defined to account for dissimilar material characteristics:

$$\frac{1}{E^*} = \frac{1-\nu_{\text{tip}}^2}{E_{\text{tip}}} + \frac{1-\nu_{\text{sample}}^2}{E_{\text{sample}}} , \tag{1.5}$$

where E_{sample}, E_{tip}, ν_{sample}, and ν_{tip}, are the Young's modulus and Poisson's ratio of the tip and sample. Similarly we can define an effective radius R for two convex bodies being the tip and the sample:

$$\frac{1}{R} = \frac{1}{R_1} + \frac{1}{R_2} . \tag{1.6}$$

The contact mechanics is often described as a spherical tip (apex) interacting with a flat sample.

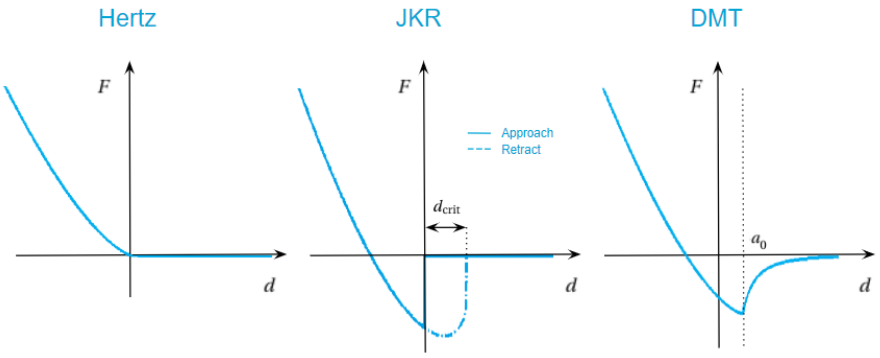

Figure 1.6 Force distance (F-d) curves of classic theories. From left to right: Hertz model, Johnson-Kendall-Roberts (JKR) model and Derjaguin-Müller-Toporov (DMT) model.

1.3.2.1. Hertz and Sneddon model

In the classic Hertz model the tip and sample are regarded as linear elastic semispheres that when pressed against each other describe small reversible deformations. In this model there are no surface forces included and the contact region remains flat and non-adhesive. If the radius of curvature of the sphere R surmounts the contact radius a we can define the interaction force as follows [23]:

$$F(d) = \begin{cases} 0 & , d > 0 \\ \frac{4}{3} E^* \sqrt{R} D^{3/2} & , d \leq 0 \end{cases} , \tag{1.7}$$

$$F_{ad}(d) = 0 \ , \ a = \sqrt[3]{\frac{RF}{E^*}} \ , \ D = \frac{a^2}{R}. \tag{1.8}$$

The Hertz model is most suitable in cases of high loads and low surface forces [15]. However, the shared elastic Hertz interaction might not always resemble the tip-surface interaction since the tip is often much harder than the sample material. This is for example the case for soft surfaces of interest in this research.

The Hertz model has significant limitations as it does not consider long range forces and surface energy effects. The Johnson-Kendall-Roberts (JKR) model is a modification of Hertz theory. The Hertz equation is modified by taking into account tensile edge stresses in the spherical contact region leading to a larger contact area [24]. This surface energy effect [24] results into an adhesive force. In the JKR model long-range

interaction forces are neglected. The JKR theory describes a non-conservative interaction force, and hence, behaves hysteratically due to work of adhesion. The governing equations are described as follows:

$$F(d) = \begin{cases} 0 & ,d > 0 \\ \frac{4E^* a^3}{3R} - \sqrt{8\pi\gamma E^* a^3} & ,d < 0 \text{ or } d < d_{cr} \\ 0 & ,d > d_{cr} \end{cases}, \tag{1.9}$$

where

$$d_{\text{crit}} = \sqrt{2\pi\gamma \frac{a_{\text{crit}}}{E^*}} - \frac{a_{\text{crit}}^2}{R} \ , \ a_{\text{crit}} = \sqrt[3]{\pi R^2 \frac{\gamma}{8} E^*} \ , \tag{1.10}$$

$$F_{ad}(d) = \frac{3}{2}\pi R\gamma \ , \ a = \sqrt[3]{\frac{R}{E^*}\left(\sqrt{F_{ad}} + \sqrt{F + F_{ad}}\right)^2} \ , \ D = \frac{a^2}{R} - \frac{4}{3}\sqrt{\frac{F_{ad}\, a}{RE^*}}. \tag{1.11}$$

The Derjaguin-Müller-Toporov (DMT) model describes an elastic tip deformation following Hertz theory and is accommodated with additional macroscopic VdW forces between the tip and sample. As a consequence an adhesive force is active outside the contact region. Unlike JKR theory, the adhesion force is conservative, and hence, does not describe hysteretic behavior. It is described by:

$$F(d) = \begin{cases} -\frac{HR}{6d^2} & ,d > a_0 \\ -\frac{HR}{6a_0^2} + \frac{4}{3}E^*\sqrt{R}(a_0 - D)^{3/2} & ,d \le a_0 \end{cases}, \tag{1.12}$$

$$F_{ad} = 2\pi R\gamma \ , \ a = \sqrt[3]{\frac{R(F + F_{ad})}{E^*}} \ , \ D = \frac{a^2}{R}. \tag{1.13}$$

Both the JKR and DMT model are approximations describing adhesion forces outside the area or inside the area of contact, respectively. The JKR model is appropriate for large tip radii and for materials with highly adhesive and compliant characteristics. DMT describes the tip-sample interaction for small tip radii and for hard samples with low adhesion [15].

1.3.2.2. Model Selection

As there is no single all-encompasing contact model, the model selection procedure requires a case dependent model evaluation. Tabor (1977) proposed a dimensionless parameter μ that indicates for specific values if DMT or JKR model should be adopted [25]. Maugis (1992) was able to describe a continuous transition from DMT to JKR as a function of a single parameter λ, called the Maugis parameter [26].

Johnson and Greenwood (1997) developed an adhesion map (Fig. 1.7) based on the Maugis-Dugdale model, indicating the applicability of the discussed contact models for distinctive cases [27]. In this map the ratio of applied load to effective adhesive energy $\bar{F}$ is displayed against the Maugis parameter λ:

$$\bar{F} = \frac{F}{\pi\gamma R}, \tag{1.14}$$

$$\mu = \frac{4.27}{a_0}\sqrt[3]{\frac{R\gamma}{\pi E^{*2}}} \ , \ \lambda = \frac{1.65}{a_0}\sqrt[3]{\frac{R\gamma}{\pi E^{*2}}}. \tag{1.15}$$

The analysis so far did not consider the presence of a water layer we encounter in ambient conditions. The Capillary forces can be added in multiple ways ranging from simple to complex models [22]. A well known approach involves usage of the modified Tabor parameter, which incorporates the Capillary effects into the Maugis framework [28]. In addition, Raman et al. provides a provisional interaction model that can be added to any particular contact model [23]. One should also note that the effect of operating conditions on the model selection process is relevant. If for instance the cantilever is sinusoidally excited and touching the

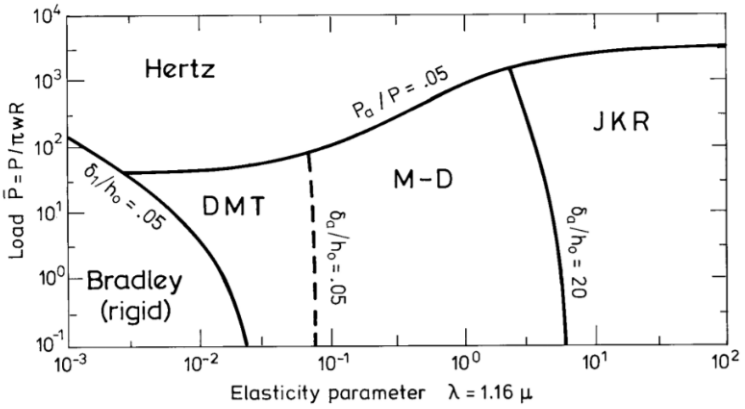

Figure 1.7 Adhesion map indicating for different values of dimensionless force $\bar{F}$ and Maugis parameter λ which contact mechanics model is applicable (Source: [27])

sample, the adhesion energy is typically negligible compared to the kinetic energy. Hence, in those cases Hertz theory is widely used [29].

Although Hertz, JKR and DMT model are widely accepted, they cannot predict viscoelastic behavior. However, several models have been developed around these models with some modifications to determine viscoelastic properties. These modifications will be discussed in section 1.6.2.

1.4. Modes of operation

In AFM we can distinguish many modes of operation. In principle, all modes have a cantilever effectively at rest or with a non-zero velocity and acceleration. These conditions are generally abbreviated as quasi-static or dynamic [30].

In quasi-static operating condition the cantilever motion is slow enough to assume that the tip-surface and cantilever force are described as:

$$F_{\text{ts}} = -F_{\text{cant}}. \tag{1.16}$$

In quasi-static mode the cantilever tip sample force, or restoring force, is given by Hooke's law

$$F_{\text{cant}} = -kd\,, \tag{1.17}$$

where k is the cantilever stiffness. A deficiency of quasi-static operations is the inability to evaluate viscoelastic behaviour which is inherently velocity dependent [30]. Hence, dynamic AFM (dAFM) methods are of much more interest in the measurement of viscoelasticity.

In dynamic AFM the cantilever is driven to oscillate at or around its resonance frequency. The tip-surface force is determined from the resulting steady-state dynamic response. The cantilever is excited by means of base displacements or application of direct force to the tip. The base displacement method is generally known as acoustic excitation mode. In acoustic mode an oscillating voltage is applied to a piezoelectric actuator which in turn produces vibrations in the cantilever [18]. Direct excitation is often executed by applying alternating magnetic forces to a magnetically coated tip by means of a solenoid.

The equations of motion for the vibrating cantilever can be described by the one dimensional Euler–Bernoulli equation describing a continuous and uniform rectangular beam exposed to an external force [18][23]:

$$EI\frac{\partial^4 w(x,t)}{\partial x^4} + \mu\frac{\partial^2 w(x,t)}{\partial t^2} = F(x,t)\,, \tag{1.18}$$

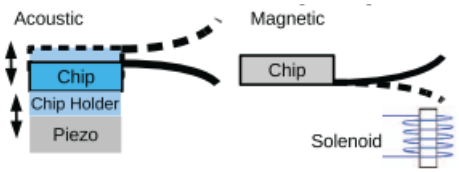

Figure 1.8: Excitation methods in dynamic AFM (Source: [23])

where E represent Young's modulus, I represents moment of inertia, μ represents mass per unit length, $w(x,t)$ represents cantilever deflection as a function of the length coordinate x at time t and $F(x,t)$ represents the driving force as a function of the length coordinate x at time t. Alternatively, in dAFM the microcantilever-tip ensemble is often modelled as a single degree of freedom system [23]. The equation of motion in force excitation mode is given as

$$\frac{\ddot{d}}{\omega_0^2} + \frac{\dot{d}}{Q\omega_0} + d = \frac{F_{\text{ts}}}{k} + \frac{F_{\text{drive}}\cos(\omega t)}{k}\,, \tag{1.19}$$

where Q, ω_0 and k are the quality factor, resonance frequency and stiffness of a single eigenmode in free vibration. The drive frequency is ω, F_{drive} is the driving force and F_{ts} is the tip-sample force.

The free dynamics (i.e., far from the surface $F_{ts} = 0$) of the cantilever can be described by a damped harmonic oscillator having a linear response, such that

$$d(\omega) = \chi(\omega)\, F(\omega), \tag{1.20}$$

with $F(\omega)$ the force experienced by the cantilever and χ a transfer function [11]:

$$\chi(\omega) = \frac{1}{k}\frac{1}{-\omega^2/\omega_0^2 + i\omega/Q\omega_0 + 1}. \tag{1.21}$$

Since in reality the ensemble is a three dimensional body, compensation is required for the model simplification by determining adequate effective quantities ω_0, Q and k of the cantilever [31]. Standard calibrations involve geometric methods and thermal methods [31]. Around resonance the force sensitivity reaches a maximum, which is why in thermal methods the Brownian motion of the cantilever is utilized to perform calibrations within a small frequency band close to resonance [30].

Eq. 1.20 can be presented in terms of its governing amplitude and phase, which are relevant equations as they are used for setpoint control [31]:

$$A_{free} = |d(\omega)| = \frac{F_{\text{drive}}}{k}\frac{1}{\sqrt{(1-\omega^2/\omega_0^2)^2 + (\omega/\omega_0 + Q)^2}}\,, \tag{1.22}$$

$$\phi_{free} = \measuredangle d(\omega) = \tan\left(\frac{\omega/\omega_0}{Q(1-\omega^2/\omega_0^2)}\right)^{-1}. \tag{1.23}$$

1.4.1. Single frequency mode

In dynamic AFM (dAFM) prevelant force measurement techniques only consider a fundamental cantilever mode with an oscillating tip deflection described as

$$d(t) = A\sin(\omega t - \phi)\,, \tag{1.24}$$

where A is the oscillation amplitude and ϕ is the phase lag relative to the excitation force [9].

During tip-sample interaction the tip experiences both conservative and non-conservative surface forces. When in contact, the conservative force $F_{\text{ts,cons}}$ represents a mirror symmetric function with respect to $\omega t - \phi$, while the dissipative force $F_{\text{ts,diss}}$ has an odd function [32]. As a consequence, the Virial (V_{ts}) can be defined as an integrated measure of the conservative energy stored in the tip-sample interaction during oscillation time

$$V_{ts}(h,A) = \frac{\omega_0}{2\pi}\int_0^{\frac{2\pi}{\omega_0}} F_{\text{ts,cons}} \cdot d\,dt\,, \tag{1.25}$$

and the energy dissipated (E_{ts}) in one oscillation cycle is determined as

$$E_{ts}(h,A) = -\int_0^{\frac{2\pi}{\omega_0}} F_{\text{ts,diss}} \cdot \dot{d}\,dt\,. \tag{1.26}$$

For single frequency oscillations around resonance, Eq. 1.25 and 1.26 can be used to determine setpoint quantities for a steady state mode of operation. The amplitude setpoint ratio A_{ratio} is defined as the ratio of the steady state engaged amplitude A and the amplitude of free vibration A_{free} [32]:

$$A^{\text{ratio}} = \frac{A}{A_{\text{free}}} = \frac{1/Q}{\sqrt{\left(\frac{-2V_{ts}(h,A)}{kA}\right)^2 + \left(\frac{1}{Q} + \frac{E_{ts}(h,A)}{\pi k A^2}\right)^2}}\,. \tag{1.27}$$

Another relationship describing the phase lag as a function of V_{ts} and E_{ts} determines the attending regime, i.e. repulsive ($\phi < \pi/2$) or attractive ($\phi > \pi/2$), and couples the 'brightness' of the phase lag to the extend of dissipation and Virial for a specific force regime [32]:

$$\tan\phi = \frac{\frac{1}{Q} + \frac{E_{ts}(h,A)}{\pi k A^2}}{-2\frac{V_{ts}(h,A)}{kA^2}}\,. \tag{1.28}$$

Hence, the Virial and dissipation equation relate the fluctuations in properties of the cantilever dynamics to measured quantities in free oscillation. Besides amplitude and phase, the eigenfrequency ω_0 and especially the quality factor Q [33] are known to be changing. During Feedback control, variation in dynamic parameters can be compensated for and, as such, images can be obtained. In dAFM we can define two general feedback modes: Amplitude Modulated AFM (AM-AFM) or Tapping mode$^{\text{TM}}$ and Frequency Modulated AFM (FM-AFM).

In AM-AFM the cantilever is excited with a fixed drive frequency ω and a fixed drive force F_{drive}. Only the static probe height h is changed to maintain a setpoint oscillation amplitude A. Following Eq. 1.27, the rest position h is adjusted so that V_{ts} and E_{ts} reach values where the desired setpoint amplitude ratio is achieved. As such, the height adjustment of the cantilever rest position h must be directly related to changes in surface height. In this way a topography image can be obtained.

In FM-AFM both the amplitude A and phase ϕ are fixed in the cantilever oscillation. The amplitude is kept constant by adapting the drive force F_{drive}. A so-called Phase-Locked Loop (PLL) adjusts the drive frequency so that a phase lag of $\phi = \frac{\pi}{2}$ is maintained, and hence, the system remains at resonance (See Eq. 1.23 for $\omega = \omega_0$). An adjustment of the cantilever rest position is required to compensate for a shift in eigenfrequency $\Delta\omega_0$, which is then relatable to surface topography [32].

In both AM-AFM and FM-AFM a Lock-in amplifier is used to extract the amplitude and phase of the noisy response signal and PI or PID control is used to adapt the difference between setpoint and extracted value [23]. As FM-AFM requires three feedback loops the measurement can be hard to stabilize [30]. It can therefore be no surprise that the simpler AM-AFM is the most utilized dynamic AFM method.

The capability to extract both a set-point amplitude (Eq. 1.27) as well as monitoring the phase lag (Eq. 1.28) allows the dynamic AFM methods to obtain both topography and surface property images at the same time. However, for single frequency methods direct measurement of dissipation is impossible as the number of

independent dynamic parameters (Q, k and A) exceeds the number of experimental observables (A, ϕ) [5]. This limitation of experimental observables can be overcome with so-called Multifrequency AFM mode.

1.4.2. Multifrequency mode

All information about the properties of a sample is encoded in the dynamics of the probe [6]. Hence, the single frequency approximation discussed includes inaccuracies as the higher harmonics generated by the nonlinear cantilever dynamics are ignored. Multifrequency mode involves either or both excitation and detection of multiple oscillation frequencies of the cantilever motion. This allows for extraction of additional information generated by the nonlinear motion of the cantilever. In multifrequency AFM, higher harmonics are typically introduced by nonlinearities in the tip surface force. The higher harmonics are exact multiples of the angular frequency of the driving force [30], now resulting in

$$d(t) = \sum_{n=1}^{N} A_n \sin(n\omega t - \phi_n), \tag{1.29}$$

where A_n and ϕ_n are the amplitude and phase delay of the *nth* harmonic with angular frequency $n\omega$ [6]. Many higher harmonics do not correspond with the higher eigenmodes of the cantilever. Hence, the amplitude of higher harmonics generally decreases with two orders of magnitude with respect to the fundamental harmonic [9], implying a limited error for single frequency methods and which makes the force detection in multifrequency methods fundamentally cumbersome. This is an important reason why, in many cases, single mode analysis is still used. On the other hand, as multiple eigenmodes are excited simultaneously, the coupling between modes enhances the amplitudes of nearby harmonics resulting in higher force sensitivity [34].

In Multifrequency AFM we can distinguish multiple methods. The Multifrequency method that will be used in this thesis is called Intermodulation AFM (ImAFM).

1.4.2.1. Bimodal AFM

In Bimodal AFM two eigenmodes, typically being the first two flexural modes of the probe, are simultaneously excited by a force

$$F_{\text{drive}}(t) = F_1 \cos(\omega_1 t) + F_2 \cos(\omega_2 t)\ , \tag{1.30}$$

where ω_1 and ω_2 are the resonance frequencies of the probe. Two excitation frequencies gives rise to four observables or 'information channels' (See Fig. 1.9). Bimodal methods typically measure the topography with one observable for the first mode and the surface characteristics with observables from the second mode. Both bimodal AM-AFM and FM-AFM arrangements are possible.

Bimodal AM-AFM has some advantages over (monomodal) AM-AFM. The phase shift associated with the second mode ϕ_2 allows for probing at larger average distances (See Fig. 1.9c) which enhances the force sensitivity in bimodal AFM [34]. In addition, as the phase lag in tapping mode AFM provides information of the material in terms of the ratio between the dissipation to virial (Eq. 1.28) it is unable to describe contrast for conservative material properties only, as this would always give zero outcome. However, the phase lag in bimodal AFM is described differently [34], which allows for contrast imaging to be applicable for conservative interactions.

Although bimodal mode presents twice the amount of observables, the calibration procedure of higher modes is difficult, making it much less accurate then fundamental mode calibration [30]. Therefore, other types of multifrequency detect many frequencies near the fundamental eigenmode.

1.4.2.2. Band excitation AFM

A second relevant multifrequency technique is the Band excitation (BE) method. In the BE method a cantilever oscillation signal is excited and detected within a selected frequency band [5]. The frequency band is typically chosen such that resonance peak is in the center of the band. The excitation signal has a predefined amplitude density and phase contrast within the frequency band of interest. The excitation described

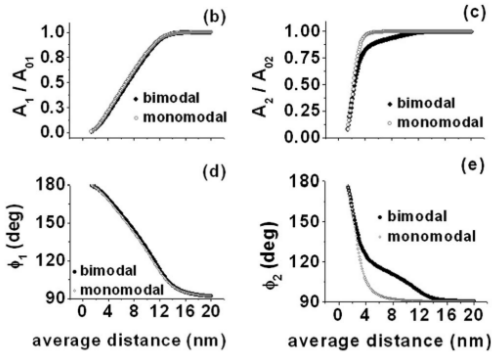

Figure 1.9: Bimodal AFM mode. Section b and c represent the setpoint amplitude as a function of average probe distance for first and second mode, respecitively. Section d and e describe the respective phase shifts as a function of average probe distance. (Source: [34])

in the frequency window is inverse Fourier transformed to generate an oscillatory cantilever excitation (see Fig. 1.10). Subsequently, the cantilever response is measured and Fourier transformed to obtain frequency dependent amplitude $A(\omega)$ and phase $\phi(\omega)$ descriptions for a particular location on the sample. By evaluating multiple points on the sample amplitude and phase images can be generated. Typically, the obtained data is fitted to free dynamics relations Eq. 1.22 and 1.23 to obtain amplitude A_{free}, phase ϕ_{free} and quality factor Q values on a point-by-point basis [5].

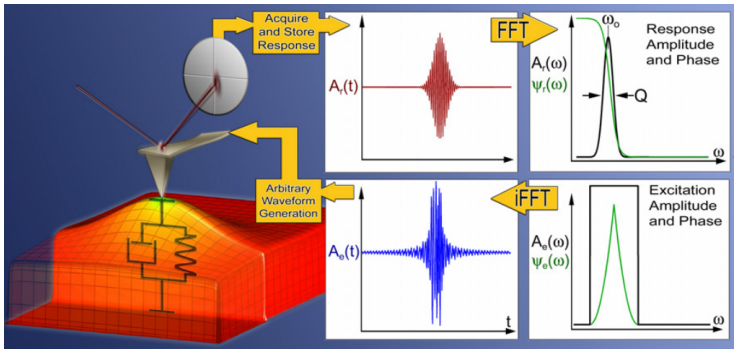

Figure 1.10: Band excitation (BE) mode: A transition scheme showing the process from excitation to response (source: [5])

1.4.2.3. Intermodulation AFM

In Intermodulation AFM (ImAFM) the nonlinearity in the probe dynamics is exploited in a narrow frequency band. Instead of increasing the amount of eigenmodes, ImAFM captures intermodulations generated around resonance. As such, one can profit from the high transfer gain and convenience of using one single eigenmode. Intermodulations represent integer linear combinations of drive tones that occur when exciting nonlinear systems. With many intermodulations it becomes possible to obtain much more observables than with traditional AFM methods.

In ImAFM the cantilever must be excited with at least two frequencies f_1 and f_2 that are almost symmetrically centred around and slightly off resonance. Their seperation amounts $\Delta f = |f_2 - f_1| \approx 500$ Hz, which is several orders of magnitude smaller than the cantilever eigenfrequency f_0. With two drive tones a beat signal is generated in free vibration showing high frequency oscillations at a fast time scale $T_{\text{fast}} = 1/f_0$ and a beat envelope at a slow time scale $T_{\text{slow}} = 1/\Delta f$. The top part of Fig. 1.11 shows experimentally obtained free amplitude spectrum $\hat{d}_{\text{free}}$ and the free motion data .

As the tip engages with the sample, the nonlinear tip-surface interaction forces distort the beating and intermodulation products occur. As the two drive frequencies are seperated by Δf, odd-order intermodulations will exist at integer multiples of Δf [7].

As the tip-sample force is the difference between the force on the cantilever and the drive force the spectrum of the tip-sample force can be obtained using the cantilever transfer function [30]:

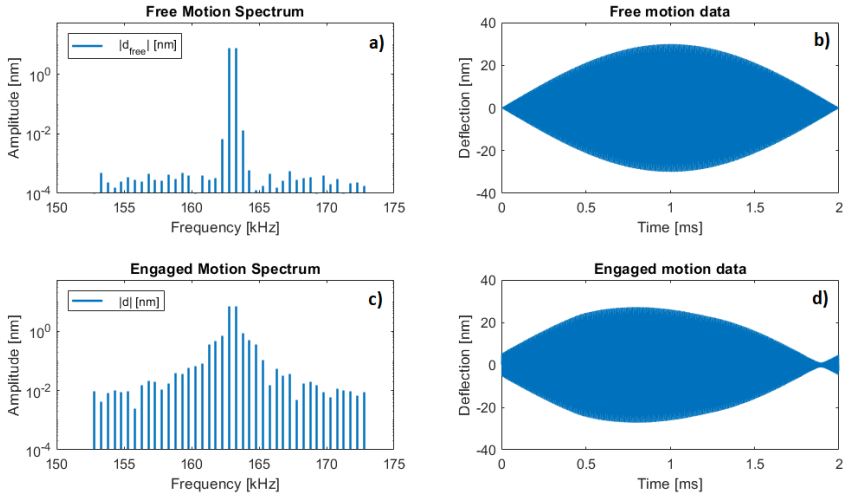

Figure 1.11 The frequency and time spectrum of the cantilever in IMAFM. (a) The free air Intermodulation spectrum around the resonance frequency in frequency domain. (b) Free air beating shape of the cantilever oscillations in time domain. (c) Engaged Intermodulation spectrum around the resonance frequency in frequency domain. (d) Engaged beating shape of the cantilever oscillations in time domain.

$$\hat{F}_{ts} = \chi^{-1}(\hat{d} - \hat{d}_{\text{free}}) \,, \tag{1.31}$$

where $\hat{d}_{\text{free}}$ represents the free motion spectrum and $\hat{d}$ represents the engaged motion spectrum.

Fig. 1.12a shows an amplitude and phase image for one single tone $f_{\text{imp}} = 2f_1 - f_2$ obtained on a polymer blend of polystyrene (PS) and (PB). Fig. 1.12b shows the amplitude and phase for multiple intermodulations to illustrate the many contrasts that can be obtained in ImAFM. The first drive tone was used for feedback, and therefore contrast is less visible there.

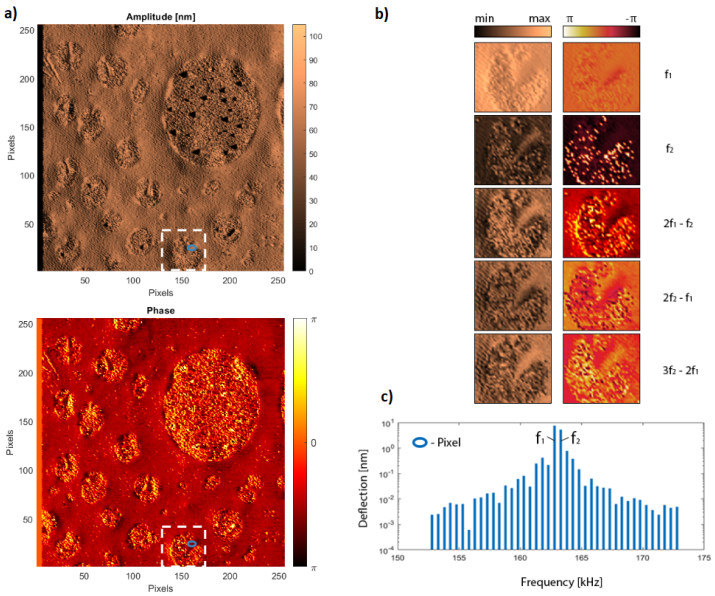

Figure 1.12 Experimental observations in IMAFM. (a) Image obtained from the tone $2f_1 - f_2$ at each of the 256×256 pixels on a $10\mu m \times 10\mu m$ PBPS surface. (b) Images for different tones of a square section depicted in a). f_1 and f_2 represent the drive tones, where other tones represent intermodulation products. (c) Engaged spectrum $\hat{d}$ of a single pixel depicted in (a).

Using the force spectrum information is extracted by analyzing the in-phase $F_I(A)$ and quadrature force

$F_Q(A)$ components as a funtion of amplitude. In this way it is possible to extract information on the conservative and dissipative interaction of the cantilever dynamics with the following formulations:

$$F_I(A) = \frac{1}{T_{\text{fast}}} \int_0^{T_{\text{fast}}} F_{ts}(t) \frac{z(t) - h}{A} dt \,, \tag{1.32}$$

$$F_Q(A) = \frac{1}{T_{\text{fast}}} \int_0^{T_{\text{fast}}} F_{ts}(t) \frac{\dot{z}(t)}{-\omega_0 A} dt \,. \tag{1.33}$$

$F_I(A)$ represents the Virial of the tip motion and $F_Q(A)$ represents the energy dissipation per oscillation cycle [35].

1.5. Introduction to linear viscoelasticity

When a purely elastic solid is deformed it instantaneously stores all obtained mechanical energy. Liquids on the other hand dissipate energy by means of viscous flow. However, not all materials can in all cases be categorized as either an elastic solid or a viscous liquid. The materials that have both elastic and viscous properties are called viscoelastic materials [36]. In fact, all materials show some viscoelastic response [37]. Significant viscoelastic effects are apparent in many polymeric materials and biological tissues, cells and membranes.

Upon loading or stretching, viscoelastic materials have a delayed mechanical response and may pick up permanent deformation. Essential is the possible history dependence or memory characteristic of these materials. Moreover, viscoelastic properties are highly rate dependent and very sensitive to temperature changes. Considering small deformations only, we can build a theoretical framework describing linear viscoelasticity. The practicality of a linear constitutive description cannot be underestimated. For instance, one can apply Hooke's law, assume Newtonian flow, utilize additivity and superposition and exploit Fourier or Laplace analysis. In practice however, nonlinearity has already shown to exist for polypropylene filaments at strains around 1 percent [38]. Hence, the linear models may not always provide satisfactory quantitative results. Therefore, implementation of linear models should be conducted with caution.

The underlying mechanism of viscoelasticity is found in the materials' macromolecular structure [39]. When polymers are subjected to an applied stress the deformation is caused by distortion of interatomic chemical bonds, or by molecule rearrangements in the direction of applied stress [40]. The atomic distortions describe small and fast changes in length and angle of bonds resulting in increase of internal energy. The molecular chain uncoiling, on the other hand, describes a decrease in conformational entropy with a certain rate depending on the molecular mobility within the material. The rate of conformational change can often be described using an Arrhenius expression [40]

$$\text{rate} \propto \exp \frac{-E^\dagger}{\bar{R}T} \,, \tag{1.34}$$

with $E^\dagger$ a particular activation energy, $\bar{R}$ the gas constant and T the present temperature. Fig. 1.13 shows the conformational rate as a function of temperature. The glass transition temperature T_g is found in the leathery or viscoelastic regime. Far above T_g the material will behave rubbery, meaning that the thermal energy is sufficient to reach a state of segmental mobility where the conformational rates become large and almost instantaneous. Far below T_g the glassy regime sets in where entropic motions are frozen and only instantaneous and reversible covalent stretching is possible [40]. Nearby T_g the material will behave viscoelastic, with a response being a combination of viscous fluidity and elastic solidity. We can characterize different types of viscoelastic materials by making a distinction between viscoelastic solids and viscoelastic fluids. Viscoelastic fluids are characterized by macromolecular mobility involving dynamic entanglement effects that are giving a viscous contribution. For large-scale chain motions this term can be represented by an average frictional coefficient per unit length [39]. Viscoelastic solids are characterized by covalently cross-linked segments. As the macromolecules are connected to each other in a cross-linked network there is no bulk mobility possible, and hence, there is a lack of viscous terminal response [41]. Upon stretching, those cross-links cause the

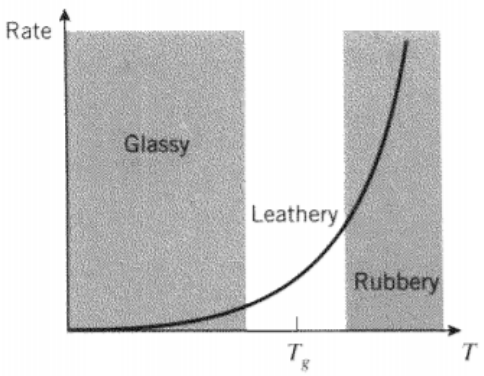

Figure 1.13: Superposition of stress increments (source: [40])

number of molecular conformational states or entropy to decrease, making the system want to go back. In this way the material behaves reversible by the mechanism of an equivalent entropic spring [41].

Viscoelastic behaviour exists on a characteristic time scale which is inherently material-dependent. The ratio between this characteristic time τ of the material and the time-scale of interest t (e.g. time-scale of certain experiment) is defined by the Deborah number:

$$De = \frac{\tau}{t} \tag{1.35}$$

In case of application of a step-load strain $\epsilon_0 h(t)$, with $h(t)$ the Heaviside step function, the time scale of a Hookean solid is infinite whereas it is zero for Newtonian viscous liquid. This means that $De \to 0$ is representitive for liquid-like behaviour and $De \to \infty$ for solid-like behaviour [42]. It can thus be concluded that both ideal elastic and viscous material properties are the limiting cases of viscoelasticity, which acts in an intermediate range depending on the temperature and the time-scale of the experiment. The stress response of a viscoelastic material in time is different for solid-like and liquid-like material and characterized by the following condition [42]

$$\lim_{t\to\infty} \sigma(t,\epsilon_0) = \begin{cases} \sigma_\infty(\epsilon_0) = 0 & \text{,for fluid} \\ \sigma_\infty(\epsilon_0) > 0 & \text{,for solid} \end{cases} \tag{1.36}$$

The constitutive description for linear viscoelastic materials is obtained through entropy inequality mechanisms as introduced above, or by using a phenomenological approach [36]. For engineering applications a phenomenological approach is often preferred where viscoelastic models are established using mechanical analogues in the form of springs and dashpots. These serve as representations of viscous and elastic responses and are combined into a constitutive discription using mathematical formulations. The constitutive relations between stress and strain for linear viscoelasticity can be described by the Generalized Hooke's law

$$\sigma_{ij} = \sum_{kl} \xi_{ijkl} \epsilon_{kl} \tag{1.37}$$

and the general expression for Newtonian media

$$\sigma_{ij} = \sum_{kl} \zeta_{ijkl} \dot{\epsilon}_{kl} \tag{1.38}$$

where ξ_{ijkl} is a modulus tensor and ζ_{ijkl} is a viscosity tensor. However, viscoelasticity is generally modelled by first taking the perspective of a single deformation mode [38]. In this way the characteristic behaviour is captured assuming uniaxial tension or simple shear, direclty relating the material response to the Youngs

modulus E or Shear modulus G. In this literature the one dimensional stress and strain are indicated by σ and ϵ, respectively.

Like the simple theory, most experiments on linear viscoelasticity are performed in a single mode of deformation [38]. We can generally distinguish three such mechanical methods: a creep test, a stress relaxation test or dynamic mechanical analysis (DMA).

1.5.1. Spring dashpot models

By now we have dicussed the behaviour of creep, relaxation and dynamic responses in a qualitative manner. Material loading history phenomena are taken care of by using Bolztmann's superposition principle. However, we have not yet established a method to obtain quantative descriptions of creep and relaxation phenomena.

For engineering purposes, the constitutive models used to describe creep and relaxation are based on spring and dashpot models. By linearity, spring and dashpot elements are independent elastic and viscous components that can be combined into a network describing a material constitutive model. The stress-strain relationship for the linear spring and damper element is described as follows:

$$\sigma(t) = k\epsilon(t), \;\; \sigma(t) = \eta\dot{\epsilon}(t) \,, \tag{1.39}$$

where k is the modulus and η the viscous constant with units Pa and Pa $\cdot$ s, respectively. The spring-dashpot models are mathematically described by Ordinary Differential Equations (ODEs) in time. These equations relate stress to strain with a general discription [36]:

$$P[\sigma(t)] = Q[\epsilon(t)] \,, \tag{1.40}$$

where P and Q are two differential operators

$$P = \sum_{k=0}^{m} p_k \frac{d^k}{dt^k} \;\; , \;\; Q = \sum_{l=0}^{n} q_l \frac{d^l}{dt^l} \,, \tag{1.41}$$

with the coefficients p_k and q_l being stiffness k or damping η parameters. The differential equation is of m^{th}- order for a creep response and of n^{th}-order for a relaxation response. Because of the step change characteristics of creep and relaxation this linear differential equation is conveniently solved using the Laplace Transform method.

The order of the model (ODE) is related to the amount of elements in the network. Multiple element models are generally more realistic, however involve more intricate mathematics and require more fitting parameters. If the mathematical model description becomes too complicated, a numerical solution can also be found by means of a finite difference method [40]. Obviously, there is a great deal of models that we can build by combining different numbers of springs and dashpots in various ways. In this paragraph we will emphasize on the most simplistic and instructive constitutive models.

1.5.1.1. The Maxwell model

The Maxwell material model consists of a spring and dashpot in series. A schematic representation of this model is given in Fig. 1.21.

Since the elements in the Maxwell model are connected in series the stress in each element is equal while the strain varies over the elements. We can add the strain in the individual elements to get the total strain. In this way we can deduce the governing differential equation in the general form of Eq. 1.40:

$$\sigma + \frac{\eta}{k}\frac{d\sigma}{dt} = \eta\frac{d\epsilon}{dt}. \tag{1.42}$$

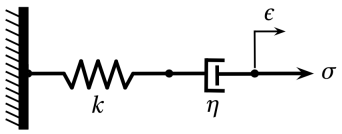

Figure 1.14: The Maxwell material model. A schematic representation of a spring and damper put in series.

This differential equation is solved using the Laplace transform method. The resulting creep response is given as

$$\epsilon(t) = \frac{\sigma_0}{k}(1 + \frac{t}{\tau'}) = J(t)\sigma_0,\ \tau' = \frac{\eta}{k}. \tag{1.43}$$

The relaxation response of the Maxwell model is described by

$$\sigma(t) = k\epsilon_0 \exp(\frac{-t}{\tau}) = G(t)\epsilon_0,\ \tau = \frac{\eta}{k}. \tag{1.44}$$

The strain response expressed in Eq. 1.43 is plotted in Fig. 1.15a. The strain response describes an instantaneous elastic response of the spring and a linear increasing creep function. Hence, the creep behaviour has no characteristic steady state converged strain. Due to the serie configuration the dashpot has no tendency to recover which leads to a permanent strain. Hence, the Maxwell model is unable to correctly describe creep response, shows no anelastic recovery and exhibits permanent deformation. The stress response expressed in Eq. 1.44 is displayed in Fig. 1.15b. We clearly see the characteristic stress decay of stress relaxation is correctly represented. Hence, the Maxwell model is characterized as a viscoelastic fluid [36].

The stress response expressed in Eq. 1.44 is displayed in Fig. 1.15b. We clearly see the characteristic stress decay of stress relaxation is correctly represented.

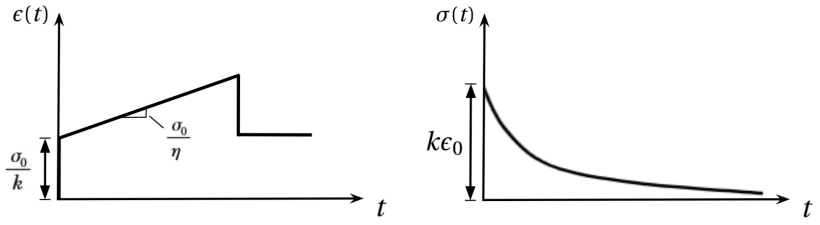

(a) The creep response (source:).

(b) The relaxation response (source:)

Figure 1.15: The creep and relaxation response of the Maxwell model

Analyzing the stress strain relations in the frequency domain we can derive the loss and storage moduli for the Maxwell model:

$$G'(\omega) = \frac{(\omega\eta)^2 k}{(\omega\eta^2 + k^2)}, \tag{1.45}$$

$$G''(\omega) = \frac{\omega\eta k^2}{(\omega\eta)^2 + k^2}. \tag{1.46}$$

1.5.1.2. The Kelvin-Voigt model

The Kelvin-Voigt material model has a spring and damper element organized in parallel as shown in Fig. 1.16.

Since the elements are in parallel the spring and damper experience the same strain and the total stress is the sum of the stress in the spring and damper. In terms of the general form of Eq. 1.40 we can write

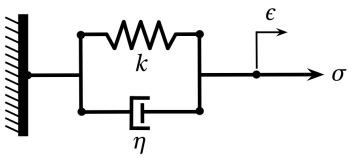

Figure 1.16: The Kelvin-Voigt material model.

$$\sigma = k\epsilon + \eta\frac{d\epsilon}{dt}. \tag{1.47}$$

The resulting creep response is given as

$$\epsilon(t) = \frac{\sigma_0}{k}(1 - \exp(-\frac{t}{\tau'})) = \sigma_0 J(t),\ \tau' = \frac{\eta}{k}. \tag{1.48}$$

If at $t = t'$ unloading occurs the subsequent recovery is described by [38]:

$$\epsilon(t) = \epsilon(t')\exp\left(\frac{t' - t}{\tau'}\right);\quad (t > t'). \tag{1.49}$$

The relaxation response is given as

$$\sigma(t) = k\epsilon_0. \tag{1.50}$$

The stress response of the Kelvin-Voigt model is shown in Fig. 1.17a. Note that there is no instantaneous strain response (i.e. $J_0 = 0$). This is a consequence of the parallel network where the spring is restrained by the retarding dashpot. We do see a transient creep and anelastic recovery where the dashpot initially takes up the stress until the spring totally dominates the stress eventually resulting in a converged strain state or full recovery when unloading. The Kelvin-Voigt model is therefore characterized as a viscoelastic solid [36]. The Kelvin-Voigt model is unable to describe stress relaxation since the response is described by a constant strain. This is shown in Fig. 1.17b.

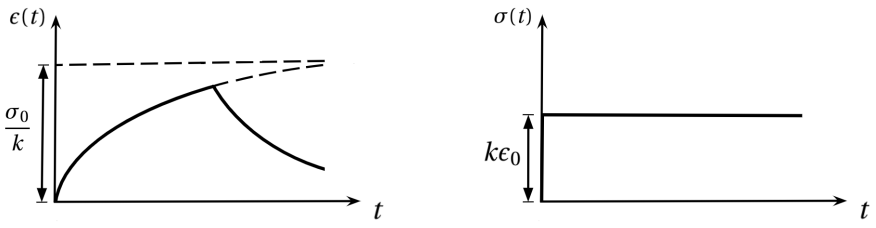

(a) The creep response.

(b) The relaxation response

Figure 1.17: The creep and relaxation response of the Kelvin-Voigt model

The dynamic moduli of the Kelvin-Voigt model are given as

$$G'(\omega) = k, \tag{1.51}$$

$$G''(\omega) = \eta\omega. \tag{1.52}$$

1.5.1.3. The Standard Linear Solid model

The Standard Linear Solid (SLS) model, also known as Zener model, is a well-known three element configuration that consists of a parallel setting between a spring and a Maxwell arm. The SLS model is the simplest viscoelastic model that resembles both creep and stress relaxation and as the name suggests, it describes a solid-like behaviour.

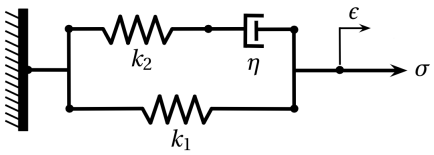

Figure 1.18: The SLS material model.

In the SLS-model the Maxwell arm and the parallel spring endure the same strain and the total stress is the sum of the stress in each arm. One can derive that the general constitutive description is given by

$$\frac{1}{\eta}\sigma + \frac{1}{k_2}\frac{d\sigma}{dt} = \frac{k_1}{\eta}\epsilon + \left(1 + \frac{k_1}{k_2}\right)\frac{d\epsilon}{dt}. \tag{1.53}$$

The creep response of the model is described as follows

$$\epsilon(t) = \sigma_0\left[\frac{1}{k_1} + \frac{1}{k_1 + k_2}\exp(-\frac{t}{\tau'})\right] = J(t)\sigma_0\,, \quad \tau' = \frac{\eta(k_1 + k_2)}{k_1 k_2}. \tag{1.54}$$

The relaxation response is given by

$$\sigma(t) = \epsilon_0\left[k_1 + k_2\exp(-\frac{t}{\tau})\right] = G(t)\epsilon_0\,, \quad \tau = \frac{\eta}{k_2}. \tag{1.55}$$

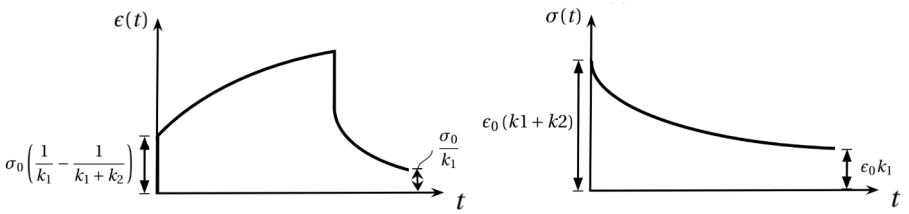

(a) The creep response

(b) The relaxation response

Figure 1.19: The creep and relaxation response of the SLS model

The SLS-model is described by an instantaneous modulus $G_0 = k_1 + k_2$ and a long-term modulus $G_\infty = k_1$ resulting in the following often utilized expression [9]

$$G(t) = G_\infty + (G_0 - G_\infty)\exp -\frac{t}{\tau}. \tag{1.56}$$

The dynamic moduli of the SLS model are represented as follows:

$$G'(\omega) = \frac{\omega^2(k_1 + k_2) + \frac{k_1 k_2^2}{\eta^2}}{\omega^2 + \left(\frac{k_2}{\eta}\right)^2}\,, \tag{1.57}$$

$$G''(\omega) = \frac{\frac{\omega k_2^2}{\eta}}{\omega^2 + \left(\frac{k2}{\eta}\right)^2}\,. \tag{1.58}$$

This specific configuration of the standard linear model has three alternative configurations being solid or fluid-like. In some ocassions four-element models or even more complex alternatives are required.

1.5.1.4. Generalized element models

The models discussed sofar describe creep or relaxation by elegant exponential functions. However, these models do not incorporate multiple relaxation and retardation times that we see in reality. The variety in length of molecular chains in the material causes multiple characteristic times, with longer chains relaxing slower than the shorter ones [40]. Hence, varying chain lengths result in a distribution of relaxation times, which results in a relaxation spectrum over a much longer time than can be modeled with a single relaxation time [40]. By expanding the models with multiple spring dashpot elements we are able to generate multiple relaxation times as well.

One can expand the simple Maxwell model by placing n Maxwell elements in parallel and adding a free spring in series. This model is refered to as the Generalized Maxwell (GMn) model or the Wiechert model. An amount of five (GM5) to ten (GM10) Maxwell elements is generally enough to obtain decent fits from experimental data [43].

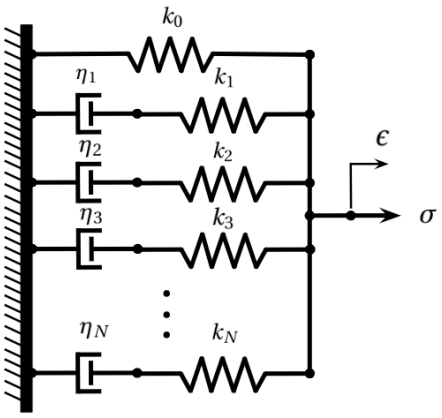

Figure 1.20: The Generalized Maxwell model.

By linearity, the relaxation response is simply given by the following summation which is often referred to as Prony series.

$$\sigma(t) = \epsilon_0 \left(k_0 + \sum_{n=1}^{N} k_n \exp\left(\frac{-t}{\tau_n}\right) \right) = G(t)\epsilon_0 \,, \quad \tau_n = \frac{\eta_n}{k_n}. \tag{1.59}$$

For an unrestricted amount of Maxwell arms we come up with the following integral expression for the relaxation modulus

$$G(t) = G_0 + \int_0^{\infty} F(\tau) \exp\left(\frac{-t}{\tau}\right) \frac{d\tau}{\tau} = G_0 + \phi(t), \tag{1.60}$$

where G_0 represents the steady state static modulus k_0, and $F(\tau)d\tau$ a weighting function defining the concentration of relaxation times within τ and $(\tau + d\tau)$, that is, the distribution of relaxation times. This distribution may be a continuous or a discrete spectrum [44].

The relaxation function $\phi(t)$ in Eq. 1.60 is a functional which depends on all values of the distribution function [44]. This functional can be rewritten as a Laplace integral. When an analytical expression for the relaxation function is known over the entire time interval, inversion of the Laplace integral can be applied to determine the distribution function. However, experiments only provide data over a limited time interval. Hence, the experimentalist requires approximate methods of which the adequacy should be evaluated [44].

Often the relaxation spectrum is slightly redefined in order to exploit a logarithmic time-scale. A logarithmic time scale is convenient since the relaxation curves generally extend over many decades of time [38]. We can now define the relaxation modulus as follows

$$G(t) = G_0 + \int_{-\infty}^{\infty} H(\tau) \exp\left(\frac{-t}{\tau}\right) d(\ln \tau). \tag{1.61}$$

Just like the Maxwell model, the Kelvin-Voigt model can be extended to a generalized Kelvin-voigt model. This model has N Kelvin-Voigt elements in series with an additional free spring in series as well.

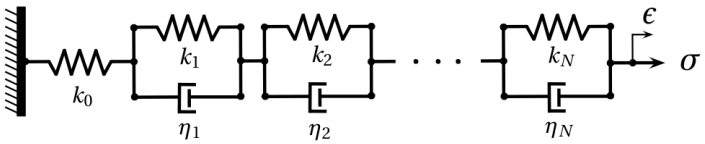

Figure 1.21: The Generalized Kelvin-Voigt model.

The relevant creep response is expressed as follows

$$\epsilon(t) = \frac{1}{k_0} + \frac{t}{\eta_0} + \sum_{n=1}^{N} \frac{1}{k_n}\left(1 - \exp\left(-t/\tau_n\right)\right), \quad \tau_n = \frac{\eta_n}{k_n}. \tag{1.62}$$

Following the same line of reasoning as for the relaxation spectrum we can define the creep compliance as in terms of a retardation spectrum $L(\tau')$

$$J(t) = J_0 + \int_{-\infty}^{\infty} L(\tau') \left[1 - \exp\left(\frac{-t}{\tau'}\right)\right] d(\ln \tau'). \tag{1.63}$$

Fig. 1.22 shows the creep response of the generalized Kelvin-Voigt model. The superposition of creep responses with multiple relaxation times is clearly visible and causes the total response to extend over a large time scale.

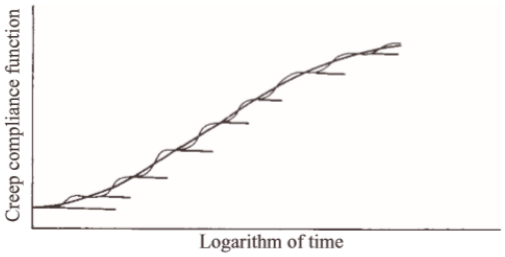

Figure 1.22: The creep response of a generalized Kelvin-Voigt model (Source: [38])

1.6. Viscoelasticity in AFM

1.6.1. Identification of viscoelasiticity on the nanoscale

Characterization of time-dependent viscoelastic material properties with AFM is performed with a variety measurement techniques. The most fundamental measurements determine relaxation and creep behaviour by applying a step change with the piezo drive, indenting the AFM tip into the surface and observing the transient response [45]. Alternatively, the analysis is performed using continuous penetration of the AFM tip with the corresponding loading and unloading branches characterized by a hysteresis loop for viscoelastic materials, as shown in Fig. 1.23. It should be noted that the identification process exhibits some practical

complications. For instance, during the force measurements the piezo-drive of the AFM displays nonlinearities, hysteresis, and velocity dependence as well [46]. In addition, the initial step load or displacement describes a ramp motion in reality, which can be troublesome if the time of the ramp is in the order of the material-dependent time. A subsequent general problem is incorrect modelling. For instance, ignoring the finite thickness effect of the sample in the model results in the discripency that can be seen in the Fig. 1.23.

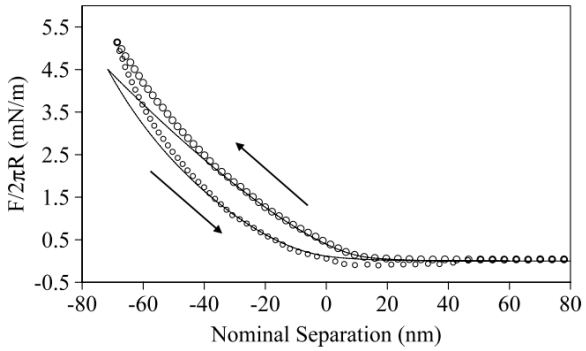

Figure 1.23: Loading and unloading measurement on a PDMS droplet. The symbols are AFM data and the curve is a fit to a viscoelastic theory. The discrepency between theory and experiment is caused by the finite thickness effect. (Source: [46])

Alternative methods involve dynamic measurements of the phase difference between drive and response in an oscillatory experiment [46]. These experiments may generally involve tapping mode AFM, force modulation or contact-resonace (CR-AFM). Depending on the desired viscoelastic property, these operations appear to be more or less favourable over one another.

As the viscoelastic interaction incorporates energy dissipation, the viscoelastic contribution is indentified and distinguished from the elastic interaction by monitoring the dissipation locally. However, the viscoelastic interaction is just a contribution to the overal dissipation process in AFM. It is important to recognize and understand the types and contribution of dissipation sources such that viscoelasticity can be identified and quantified. The dissipation processes of interest can be described on the nanoscale or the atomic scale [47]. Viscoelasticity is more macroscopic in nature, and hence, nanoscale analysis is adopted for the dissipation description. In force modulation or tapping mode the phase lag between excitation and tip response is translated in terms of energy dissipation [32]. Phase contrast imaging with AM-AFM has proven a powerful tool for the observation of energy dissipation variations in local surface regions. In this procedure Garcia et al. distinguishes dissipation originating from surface energy hysteresis, viscoelasticity and long-range dissipative interfacial interactions [48]. By recovering the local dissipation against the amplitude setpoint and its derivative Garcia et al. quantitatively distinguished these dissipation sources. Fig. 1.24a) shows the dissipation contributions as a function of the amplitude set-point, normalized by the maximum value. The short range hysteresis indicitated in black shows an unambiguous plateau which makes it easy to discriminate the short-range contribution. As long-range interactions and viscoelasticity often look similar in experiments, the derivative of the dissipated energy is generally required to distinguish between them (Fig. 1.24b)). To disciriminate the contribution of Capillary forces in the observed dissipation, a set ofpeak force tapping experiments can be conducted under ambient and dry nitrogen flushed environments [9].

Hence, with dynamic AFM we are able to discriminate between multiple dissipation processes, where static methods such as loading and unloading tests do not clarify the nature of the dissipation process [48]. In dynamic analysis the conservative and dissipative characteristics of viscoelasticity are quantified by means of the storage and loss modulus. These quantities are derived from continuous periodic strains or loads with the sample reaching a steady state. Hence, in AFM the dynamic modulus can only be applied in the presence of continuous periodic measurement. As the tip-sample interaction in intermittent contact operations is not continuous, the use of dynamic modulus or any quantities derived from it (e.g. the loss-tangent) is erroneous in this mode [49]. However, the other method, often abbreviated as contact-resonance (CR-AFM), is analogous to DMA. Here a vibrating AFM tip is brought into mechanical contact with the sample and the transfer function between the load and displacement provides a method of calculating the storage and loss modulus of the material. Yablon (2014) investigated the loss tangent values on polymer components using AM-AFM and CR-AFM which was applied in dual resonance tracking mode (DART) and band excitation (BE) mode. It

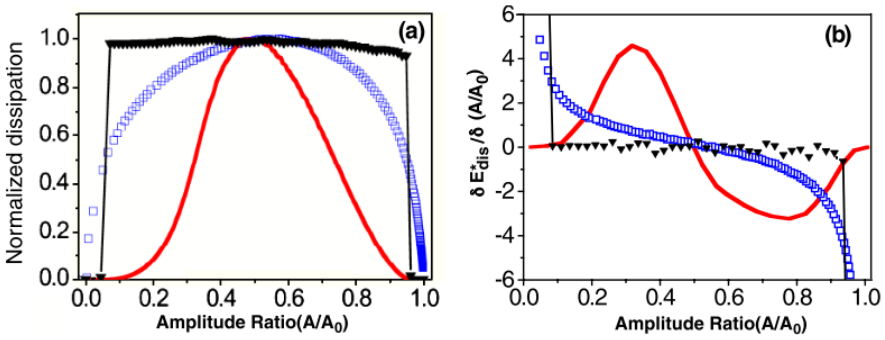

Figure 1.24: Dissipation processes (Source: [48])

was experimentally validated that CR-AFM in BE mode gives the most accurate absolute loss tangent [50].

1.6.2. Viscoelastic interaction modelling

In order to be able to link the experimentally observed phenomena to local viscoelasticity it is important to develop models that appropriately describe the many characteristics of viscoelastic behavior. This involves creep, relaxation, history dependence and ocasionally multiple relaxation times. We have seen that viscoelasticity is often described using a phenomenological approach involving mathematical analogues in the form of spring–dashpot sets. The suitability of the model is different depending on the material under investigation. The type of AFM operation is also important in the determination of a suitable model. In contact-mode operations surface forces can sometimes be neglected, while in intermittent contact operations surface forces and relaxation mechanisms should be described accurately [9]. Some materials and methodologies may require complex models with a variety of fitting parameters in order to characterize the physical properties. Nonetheless, it is always attempted to find the simplest model that offers a correct physical characterization of the material under investigation.

Viscoelasticity is introduced when tip-sample interactions occur in the contact regime [51]. Hence, the viscoelastic interaction model requires a contact mechanics description in terms of viscoelasticity involving time-dependent loads and deformations. The usage of elastic contact mechanics is rather convenient in these circumstances. However, the continuum elastic theory is inapplicable to viscoelastic problems as they are based on an equilibrium assumption that is valid only in the static case for elastic materials [46]. In addition, one should be aware that the nanoscale operation in AFM causes enhanced deformation of the surface of viscoelastic materials, as they are generally 'soft' [49], with the elastocapillary length often approximating the typical radius of an AFM tip [8]. As mentioned in earlier chapters, this nanoscale effect makes the JKR theory more impractical. Polymeric surfaces can also exhibit complex structures with significant variability in multiple directions and therefore prohibit application of continuum treatment [49]. Nevertheless, in many different studies continuum elastic concepts such as DMT and JKR are implemented into the model [51]. Oftentimes these contact theories are modified ad hoc by implementing time-dependent creep compliance or relaxation modulus into the classis elastic interaction equations.

1.6.2.1. Ad hoc models

In practice, the viscoelastic interaction during tip-sample contact is often described by dividing the interaction into a conservative and a dissipative description. In this way a relationship between contact area and sample deformation can be defined for the conservative as well as the time-dependent viscoelastic force. By using nonlinear spring and dashpot elements the changing surface area for the viscoelastic component can be resembled [51]. The dissipative contribution is generally abbreviated as an ad hoc addition of viscoelasticity. The ad hoc component is introduced as F_{ts}^{DISS} such that

$$F_{ts}(d,\dot{d}) = F_{ts}^{CONS}(d) + F_{ts}^{DISS}(d,\dot{d}), \tag{1.64}$$

where the conservative tip-sample force F_{ts}^{CONS} is represented by one of the classic elastic contact models, usually being the DMT model [51]. A vastly utilized ad hoc model introduced by San Paulo and Garcia (2001)

applies the relation between contact area and sample deformation of the Hertz model for a Kelvin-Voigt material [52]. This model is described as:

$$F_{ts}^{DISS}(d,\dot{d}) = -\eta\sqrt{Rd}\dot{d}, \tag{1.65}$$

with d the tip-sample seperation distance. This model is also used in the dissipation characterisation of Garcia et al. (2006) discussed in the previous paragraph. As mentioned earlier, the ad hoc models can be practical under particular circumstances, however remain inherently artificial. An example of practicality is the experiment of Garcia et al. which showed deviations less than 1 % between experiment and simulation in most of the data [48]. Raman et al. [9] showed the physical problems involving the highlighted ad hoc description with an Hertzian conservative contact. Fig. 1.25 shows the force-distance behavior of an oscillating tip indenting and withdrawing from the surface in a single tap. Upon withdrawing, the deformed sample has a delayed response due to relaxation behavior, allowing the tip to detach early from the sample. However, as the repulsive Hertz model cannot describe this, an attractive force is applied to constrain the tip to the sample which is inherently non-physical [9].

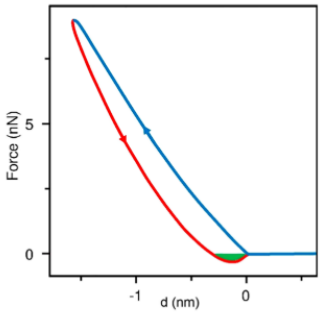

Figure 1.25: Force-displacement (F-d) curve for the ad hoc Hertz model with Kelvin-Voigt viscoelasticity (Source: [9])

1.6.2.2. Spring-dashpot models

López-Guerra and Solares (2014) used one-dimensional models including macroscopic van der Waals (VdW) force to describe the tip-sample interaction in tapping mode operation. As expected, it was shown that the Standard linear solid (SLS) model accounts for the instantaneous interaction force of the tip, as well as describing for surface recovery. Fig. 1.26 describes the transient behavior of this SLS model. As the SLS model is the simplest configuration that provides a qualitatively correct description of viscoelastic behavior, it is extensively utilized in many studies [51].

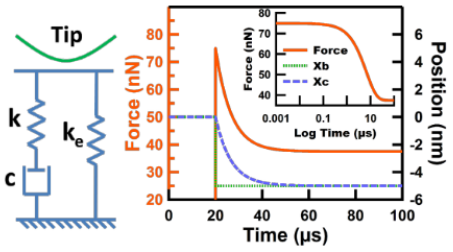

Figure 1.26 Tip-sample interaction: SLS model. One can observe an instantaneous response X_b in the arm of spring k_e and a relaxation X_c in the Maxwell arm. (Source: [51])

In principle, one-dimensional spring-dashpot models have severe simplifications. For instance, stresses and strains are considered uniform throughout the material [49]. In practice this simplification might not result in descent reconstructions of AFM measurements.

1.6.2.3. More elaborate models

A complete description of viscoelastic interaction needs to be described in three dimensions (3D) including the contact area history dependence of the tip. Using the elastic-viscoelastic correspondence principle it becomes possible to derive a viscoelastic solution from contact mechanics. Lee and Radok (1960) used the correspondence principle to determine the viscoelastic solution for the Hertz model for a contact radius that is monotonically increasing with time [53]. Subsequently, Ting (1966) presented the viscoelastic solution for the Hertz model for an arbitrary loading history [54]. However, an obvious limitation is the lack of surface forces and long-range forces in Hertz model. Attard [46] also takes into account the out-of-plane surface motion of the sample by applying the viscoelastic correspondence principle to the elastic half-space approximation (See Fig. 1.27). In this model the long-range interaction is incorporated through a Lennard Jones pressure distribution [55]. Determining the deformation as a function of the tip-sample seperation and the pressure profiles requires many variables and steps, which Attard formulated in terms of an algorithm [56] that has been expedited by Raman et al. [9].

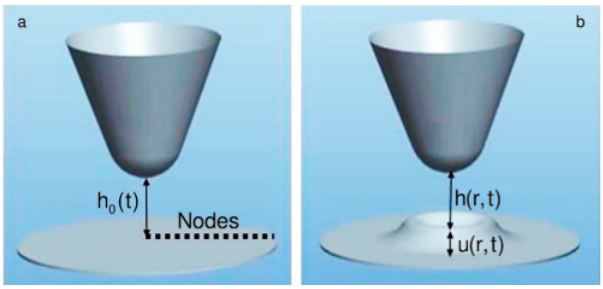

Figure 1.27 Illustration of Attard's model [56]: a) unstressed situation at distance h_0 b) As the tip approaches to a distance h, the material surface disforms upwards with height u, after which it will snap on to the tip. Upon retraction the tip will detach from the surface resulting in a surface motion and subsequent relaxation.(Source: [9])

Although this method gives a theoretical description in 3D it depends on the estimation of many model parameters. This is quite problematic as in AFM experiments there is only one observable to fit many parameters. Secondly, in Attard's model there are multiple uncertainties associated with the parameters such as Hamaker constant and equilibrium distance of the pressure profile [9]. Hence, the model obtained through the viscoelastic correspondence principle is theoretically sound, however it conveys many impracticallities. For this reason it is in many cases interesting to come up with simplified models [8].

Solares (2016) [49] proposed a quasi-three dimensional (Q3D) model where SLS elements are arranged in a polar coordinate partitioning and interconnected with additional linear springs to resemble surface effects (see Fig. 1.28 (a),(b),(c)). By element interconnection more elements will interact with the tip as indentation increases, and hence, surace energy effects for soft materials are better represented. This is clearly made visible by the increase in upward curvature for the Q3D model as the indentation increases in Fig. 1.28(d). By the increased interaction more elements will be in close proximity to the tip upon indentation, resulting in larger VdW interactions upon retraction, also evident from Fig. 1.28(d) [49]. Yet, this model still has eminent limitations, such as the ability to relax in vertical direction only and the negligence of shear stresses.

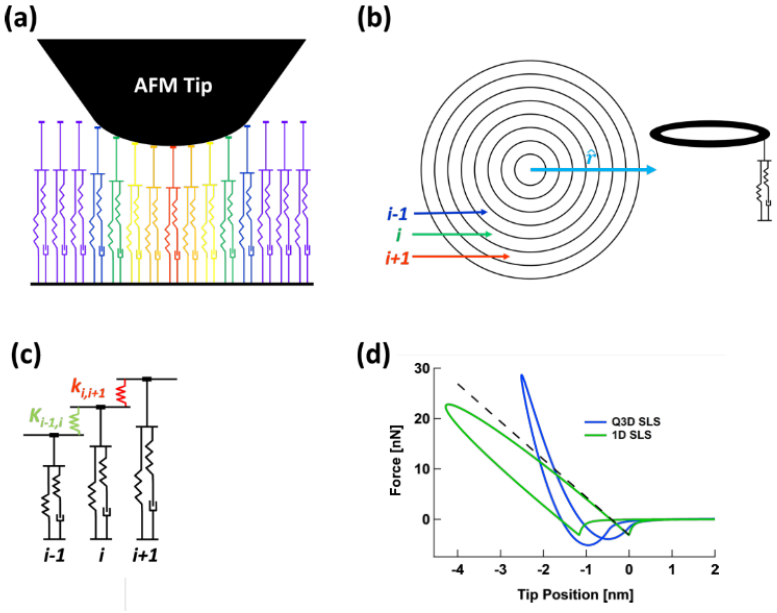

Figure 1.28 Illustration of Quasi-3D model developed by Solares [49]. (a) Cantilever tip interacting with a 'bed' of mechanical spring-damper systems known as SLS model. (b) Polar coordinate of spacing of SLS elements. (c) SLS systems are interconnected using springs. (d) Force-distance curve describing tip-sample interaction with a single SLS element and multiple interconnected SLS models described as Quasi-three dimensional (Q3D) (Source: [49]).

1.7. Conclusion

In this thesis the research objective is to utilize intermodulation technique to extract viscoelastic properties. The advantage of using ImAFM is that many experimental observables can be obtained with high resolution. These observables are channels that provide information about the tip-sample interaction. In order to interpret the data it is required to develop interaction models describing the physics of the interaction. For soft samples it is required to describe the interaction in terms of viscoelasticity.

The literature specifies a variety of models used to perform characterization of viscoelasticity. It was emphasized that surface forces are of great importance in intermittend contact operation. A new model is presented capable of showing independent surface motion in a simple manner [13]. As part of the literature survey numerical simulations are performed to simulate the dynamics of this moving surface model (see Appendix B).

In simulations it was discovered that the moving surface model shows high fluctuations in parameter sensitivity and a lack of proper optimization technique to arrive at the global minimum. In this research it is investigated where this viscoelastic model in relation with the intemodulation technique can be improved for viscoelastic characterization.

2

Viscoelastic characterization with Multifrequency AFM

Viscoelastic characterization with Multifrequency AFM

C.L. Penning

Department of Precision and Microsystems Engineering, Delft University of Technology, Delft, The Netherlands

January 17, 2020

The interaction between an atomic force microscope tip and a soft-material sample is described within the framework of viscoelasticy. Previous studies capture the physical process of experimental phenomena in multiple soft samples. Nevertheless, viscoelastic identification of the physcial sample properties has only been peformed using local optimization techniques, requiring recursive evaluation of the model and good intuition to fit only one single point of a specimen. In this study we introduce a systematic identification of viscoelastic properties of soft samples based on the Multifrequency method and analyze whether a more automatic approach can be performed. A toolbox has been developed to provide numerical simulations, global optimization and sensitivity analysis. The dynamical response of the interacting surface is studied for different parameter sets to accurately characterize the behavior of the moving surface in a more comprehensive manner.

Keywords: Atomic force microscopy, Viscoelasticity, Multifrequency, Sensitivity analysis, Optimization

1. Introduction

In the last decennia, atomic force microscopy (AFM) has emerged as the prominent nanomechanical tool for characterization of soft samples.[1] Recent development of a new field in dynamic AFM methods, called Multifrequency AFM, enables probing with higher sensitivity and resolution.

Multifrequency AFM comprises methods utilizing higher eigenmodes such as bi-modal operations and methods involving excitation within frequency bands of interest. Using Intermodulation AFM (ImAFM) the nonlinearity in the probe dynamics is exploited in a narrow frequency band. ImAFM captures intermodulations generated around resonance as a consequence of the nonlinear tip-sample interaction force. As such, one can profit from a high transfer gain and convenience of using one single eigenmode. The intermodulations that occur introduce many new experimental observables in comparison with conventional dynamic AFM methods. With this advancement, there is a strong motive for the investigation of the tip-sample interaction models as they connect the experimental observables to the physical properties of the material.[6,12]

As a result of the complexity of the tip-sample interaction, deconvolution of the information out of the AFM is a challanging task. When dealing with soft samples, the interaction needs to be described in a viscoelastic framework. At the moment there is no standard model for viscoelastic interaction and oftentimes Hertzian contact mechanics is employed. As such, only the Young's modulus is measured, taking into account elastic contact and neglecting viscoelastic effects.[1] In an attempt to characterize material damping there exist ad hoc formulations combining elastic and viscoelastic forces. However, the physical soundness of these models is oftentimes lacking. Ad hoc models generally neglect the fact that the interaction between a cantilever tip and a soft material taking place at the nanometer scale will be governed by surface forces, causing local miniscus forming of a soft surface around the tip. With a different approach, more complex models include surface phenomena in three-dimensional field descriptions.[3] However, such models involve many free parameters; some characterized by uncertainties.

Haviland et al. (2015)[6] describe a simplified model taking into account surface rheology. In the moving surface model the instantaneous surface position is introduced as independent variable, describing a spatially averaged surface position. Thoren et al. (2018)[2] have presented the ability of the model to resemble diverse behaviors of viscoelastic interaction for multiple of soft samples. The model fits the experimental data using a least-squares optimization local to the solution.

In this research ImAFM is utilized to extract the viscoelastic properties of soft samples. A Toolbox is developed in MATLAB to perform numerical simulations with the moving surface model. During multiple model evaluations it was discovered that intrinsic model behaviors hindered the performance of optimization methods. In this research the model characteristics are investi-

gated further in order to enhance its ability to be used in viscoelastic characterization and instead of local we use global optimization techniques as a more systematic approach.

2. Experimental setup

In ImAFM, a Multifrequency Lock-in Amplifier (MLA)[14] excites a shaker piezo with two drive frequencies f_1 and f_2, which are integer multiples of the measurement bandwith $\Delta f \approx 500$ Hz. When the drive frequencies are integer multiples of Δf, intermodulation products caused by the nonlinear tip-sample interaction will also occur at integer multiples of Δf. Using MLA all tones are locked in by means of the integer value relationship such that many frequencies are extracted in the same measurement time. The MLA measures the amplitudes of the response in-phase and out-of-phase with excitation, coming from the detector at exactly the tones that are locked-in (see Figure 1).

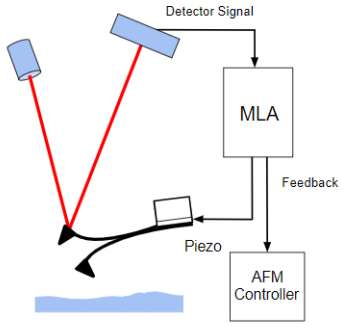

Figure 1: Setup in ImAFM. While scanning, the MLA is regulates cantilever excitation and detection of the response signal. Feedback is managed by the AFM controller.

With two drive frequencies f_1 and f_2 a beat signal is generated in time showing high frequency oscillations at a fast time scale $T_{fast} = 1/f_0$ determined by the canilever eigenfrequency f_0, and a beat envelope at a slow time scale $T_{slow} = 1/\Delta f$.

From the free oscillation spectrum far from the surface $d_{free}(\omega)$, with spectral components indicated by a hat such that $d_{free}(\omega) = \hat{d}_{free}$, the drive force $\hat{F}_{drive}$ is derived from a transfer function $\hat{\chi}$ representing the cantilever body as a linear harmonic oscillator:

$$\hat{F}_{drive} = \hat{\chi}^{-1}\hat{d}_{free}\ , \tag{1}$$

with

$$\hat{\chi}(\omega) = \frac{1}{k}\frac{1}{-\omega^2/\omega_0^2 + i\omega/Q\omega_0 + 1}. \tag{2}$$

The parameters ω_0, Q and k represent the cantilever resonance frequency, quality factor and stiffness, respectively. These quantities are obtained using thermal calibration of the cantilever far from the sample.
When the cantilever is engaging with the surface, the tip-sample force is the difference between the force on the cantilever and the drive force[4] such that

$$\hat{F}_{ts} = \hat{\chi}^{-1}(\hat{d} - \hat{d}_{free})\ , \tag{3}$$

where $\hat{d}$ is the engaged spectrum incorporating intermodulation products (IMPs) at integer multiples of Δf. When imaging, a delayed response of the surface characterizes the viscoelastic interaction, which affects the motion of the cantilever. In this way, without observing the surface motion in an experiment the cantilever distortion can be related to a physical description of viscoelastic surface effects in a simulation.

There are inaccuracies associated with the identification of $\hat{F}_{ts}$. They arise when the tip comes in close proximity of the sample where forces on the whole cantilever body cause shifts mainly in the cantilever's quality factor. Those long-range effects are generally induced by squeeze-film damping or electrostatic forces.[5] One has to eliminate these background forces in order determine the tip-sample interaction force as depicted in Equation 3. Borgani et al. (2017)[5] resolves the background forces by defining an effective driving force $\hat{F}'_D$, where an effective drive force $F'_{drive}(t)$ is defined via the inverse Fourier transform.

The physical behavior of the interaction force $\hat{F}_{ts}$ is related to the cantilever tip position and velocity in Force quadrature curves F_I and F_Q. As amplitude modulation is slow compared to the fast oscillation cycles of the cantilever, the amplitude A can be assumed constant in this time period. As such, the force quadratures are determined for each oscillation cycle as a function of oscillation amplitude A:[10]

$$F_I(A) = \frac{1}{T_{fast}}\int_0^{T_{fast}} F_{ts}(t)\frac{z(t)-h}{A}dt, \tag{4}$$

$$F_Q(A) = \frac{1}{T_{fast}}\int_0^{T_{fast}} F_{ts}(t)\frac{\dot{z}(t)}{-\omega_0 A}dt. \tag{5}$$

A positive F_I represents a prevalent attractive interaction force and a negative F_I represents a prevalent repulsive interaction force. In addition, a negative F_Q quantifies dissipation.[6] Hence, force quadratures are of great advantage as they depict the nature of the tip-sample interaction.

3. The moving surface model

The moving surface model represents a system of two harmonic oscillators as follows

$$m\ddot{d} + \eta\dot{d} + kd = F_{ts}(s, \dot{s}) + F'_{drive}(t), \tag{6}$$

$$\eta_s\dot{d}_s + k_s d_s = -F_{ts}(s, \dot{s}). \tag{7}$$

Equation 6 describes the cantilever eigenmode and Equation 7 the surface dynamics. Moreover, η_s is the surface damping, k_s is the surface stiffnes and $m = \frac{k}{\omega_0^2}$ and $\eta = \frac{k}{Q\omega_0}$.

The tip-sample force F_{ts} depends on the seperation s between the instantaneous cantilever position ($z = d + h$) and surface position ($z_s = d_s + z_0$), such that $s = z - z_s$. Using a Piecewise Linear (PWL) force model, the force profile is linearized during contact:[2]

$$F_{ts}(s, \dot{s}) = -F_{ad} - k_v s - \eta_v \dot{s}, \tag{8}$$

with F_{ad} the adhesion force, η_v the interaction damping and k_v the stiffness describing bulk compression.[2] The PWL-force model is useful as it is the simplest model to represent all elementary characteristics of the tip-sample interaction force in the simplest way. As alternative, interaction forces have been defined in terms of the well-known DMT interaction.[6] The main advantage of using a linearized description is that it allows for analytical analyis of the linear system presenting viscoelastic behavior.

There are multiple viscoelastic mechanisms at play during tip-sample interaction. The process of a moving surface growing on the tip is referred to as 'contact formation',[2] where the surface is lifting up to a maximum asymptotic height δ_∞

$$\delta_\infty = \frac{F_{ad}}{k_s + k_v}\,, \tag{9}$$

in a characteristic time τ_c, given by

$$\tau_c = \frac{\eta_v + \eta_s}{k_v + k_s}\,. \tag{10}$$

The time constant τ_v involved with the deformation of the sample during penetration is represented by[2]

$$\tau_v = \frac{\eta_v}{k_v}. \tag{11}$$

After the cantilever detaches from the surface, meaning $s > 0$, the surface creeps back to its equilibrium state with a retardation time τ_s. For the Kelvin-Voigt surface description, the redardation time is described as

$$\tau_s = \frac{\eta_s}{k_s}\,. \tag{12}$$

Hence, given the calibrated values of the cantilever and the drive force in the experiment, the dynamics of the moving surface is interpreted using Equation 9-12. The force quadratures F_I and F_Q can be exploited for identification purposes. In detail, hysteresis in the quadrature curves is directly related to the model characterisitcs presented by Equation 9-12. High hysteresis is positively related to high retardation times and high surface lift. High dissipation can also be found for low surface damping values, understanding that large amplitude surface lift can also have a significant dissipative contribution.[6] Hence, it is not straightforward to attribute one specific process to one particular response.

Summarizing the aforedescribed formulation, the moving surface model is characterized by 6 free parameters: k_v, k_s, F_{ad}, η_s, η_v and h. This set can be reduced since the maximum attractive interaction force for increasing amplitude will generally give an indication of the static probe height h. Using physical interpretation of quadrature curves and relating it back to the model parameters, it is attempted to represent the observables in the experiment with 5 (6) free parameters. This approach is challenging as it requires at least a number of careful examinations of the model behavior. Moreover, it might be possible that the model simplfy fails to sufficiently represent the experimental data.

4. Optimization

In an optimization procedure the free parameters arranged in a vector $\boldsymbol{p} = \{k_v,\ k_s,\ F_{ad},\ \eta_s,\ \eta_v\}$ are iteratively adapted in order to reconstruct the experimental observables in a simulation. In ImAFM experimental reconstruction can be performed with the spectrum of the tip-sample force $\hat{F}_{ts}$ because of the high force sensitivity around resonance. Forchheimer et al.[8] have

shown image contrast being largest at weakly responding intermodulations farther from resonance. Using force reconstruction, especially weaker tones farthest from resonance are more pronounced, which can be understood by looking at the sharp peak of a linear transfer function around resonance. In this way force reconstruction reinforces the contribution of weak intermodulations in a fitting procedure.

In order to perform force reconstruction, Thoren et al. (2018)[2] find the parameter set of the moving surface model that best resembles the experiments in a local minimization procedure. In local optimization one finds a local minimum from a good initial position. Hence, using trial and error one must come close to the solution before optimization can be performed.

In the optimization procedure the force Fourier components are fitted in a method suggested by Forchheimer et al.[11] Here the least-square-error E^2 of the residual $\hat{\epsilon}$ between n intermodulation products in experiment and simulation is determined as a function of the parameter set $\boldsymbol{p}$:

$$\hat{\epsilon}(\boldsymbol{p})[n] = \hat{F}_{ts,sim}(\boldsymbol{p})[n] - \chi^{-1}[n](\hat{d}[n] - \hat{d}_{free}[n]), \quad (13)$$

$$E^2(p) = \sum_{n=1}^{N} Re\left(\hat{\epsilon}(\boldsymbol{p})[n]\right)^2 + Im\left(\hat{\epsilon}(\boldsymbol{p})[n]\right)^2, \quad (14)$$

such that the objective function $\bar{f}$ is defined as

$$\bar{f}(\boldsymbol{p}) = \min_{\boldsymbol{p}} E^2(\boldsymbol{p}). \quad (15)$$

Unless any knowledge is obtained a priori from the experiment, it is almost impossible to accurately estimate how close the parameters are to the optimum. Therefore, it is hard to impose bounds on parameter values. Hence, if a local optimization scheme is to be examined, unconstrained methods are to be employed. The Levenberg-Marguardt algorithm seems to be suitable as it performs a least-squares optimization and is able to find a local minimum relatively far from the optimum.

In order to validate the performance of the algorithm, one first has to come close to a local minimum that in our case is realistic in an experiment. As it is rather difficult to converge to such a minimum in an experiment, it was attempted to analyze the perfomance for a proposed, namely synthetic, parameter set. As such, we optimize for a specific system dynamics of the moving surface model. Using such a synthetic dataset is supported by the fact that the model should actually resemble dynamics in the experiment.

As we wish to analyze realistic model behavior, parameter values were chosen to be in similar order of magnitude to those in Thoren et al. (2018).[2] Table 1 shows the minimum and maximum orders of magnitude of all parameter values found in their experimental characterization.

The Levenbeg-Marquardt algorithm has been evaluated for 15 synthetic parameter sets within this range. As this method uses gradients to find the optimum, we evaluate the performance of the algorithm for varying finite difference stepsizes. To make a fair comparison, initial parameters start from identical positions. The initial values were chosen to differ no further than $\pm$ 50% of the optimal values. We estimated that $\pm$ 50% is a descent range as for such initial conditions the quadrature curves affiliated with the initial and optimal parameter set still show considerable resemblence.

Figure 2 shows the mean, minimum and maximum percent error in parameter values for two stepsizes (1e-4 and 1e-5) that showed best convergence.

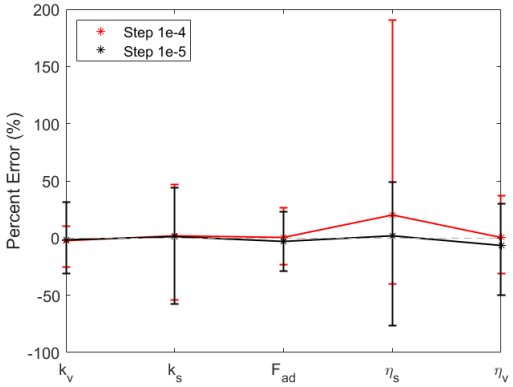

Figure 2: *Error analysis for 15 synthetic parameter sets. Bar plots indicate mean, minimum and maximum error. For stepsize 1e-4 mean values are* $kv = -2.36\%$, $ks = 2.26\%$, $F_{ad} = 0.29\%$, $\eta_s = 20.25\%$, $\eta_v = 0.36\%$, *and for stepsize 1e-5 mean values are* $kv = -1.60\%$, $ks = 0.98\%$, $F_{ad} = -3.21\%$, $\eta_s = 1.69\%$, $\eta_v = -6.48\%$.

A striking observation in Figure 2 is the presence of a relatively low mean error combined with high outliers, diverging to almost 200% for damping parameter η_s. It is of interest to find the reason for those sporadious peaks. Thus it is worth to investigate the relationship between individual parameters and the objective function

Table 1: *Realisitc parameter range of variables, derived from Thoren et al. (2018)[2] (see Appendix A.1).*

Parameter	k_v (N/m)	k_s (N/m)	F_{ad} (nN)	η_s (mg/s)	η_v (mg/s)
Range	10^{-2} - 10^{1}	10^{-2} - 10^{2}	10^{-1} - 10^{1}	10^{-3} - 10^{2}	10^{-2} - 10^{1}

$\bar{f}(\boldsymbol{p})$.

Figure 3 shows how single parameter values are perturbed by $\pm$ 50% from the optimum p for two parameter sets characterized by the highest errors in η_s. Apparent is a discrepancy in parameter sensitivity. Especially for η_s there is minimal influence on the objective, and hence, it locally represents a redundant variable. A relevant question is whether one can establish a consistent behavioral pattern in divergency of parameter sensitivity.

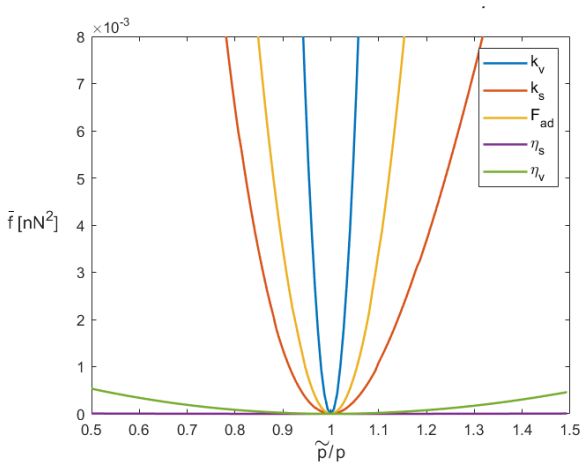

Figure 3: *Parameter Sweep of $\pm$ 50 % for parameter set $\boldsymbol{p}$ characterized with* 123% *error in η_s, obtained with Levenberg-Marquardt optimization routine. The parameter set consists of $k_v = 0.0972$ N/m, $k_s = 7.28$ N/m, $F_{ad} = 9.44$ nN, $\eta_s = 1.13$ mg/s and $\eta_v = 0.0617$ mg/s. The perturbed parameters $\widetilde{p}$ are normalized by their optimal value p.*

5. Sensitivity Analysis

We investigate whether there exists a consistent behavioral pattern in the respective influence of the model parameters. The model dynamics is characterized by the parameter set at hand, and hence, inidividual parameter sensitivity needs to be chracterized as a property of a specific parameter set and its associated dynamics. Each parameter set can be identified by its particular Fourier components of the intermodulations in the tip-sample force. Perturbation of a single parameter value Δp_i will generate a variation in the Fourier spectrum. By redefining Equation 16 as the error of the Fourier components of the initial $\boldsymbol{p}$ and perturbed $\widetilde{\boldsymbol{p}}$ parameter set:

$$\hat{\epsilon}(\boldsymbol{p})[n] = \hat{F}_{ts,sim}(\boldsymbol{p})[n] - \hat{F}_{ts,sim}(\widetilde{\boldsymbol{p}})[n], \qquad (16)$$

we are able to define the sensitivity of a particular parameter with respect ot individual parameters.

The initial parameter set represents a minimum as is evident from the convex function in Figure 3. Hence, at the location of the initial, unperturbed parameter set the first-order derivative is zero by theory and not suitable to characterize its properties. Therefore, it was decided to use the second-order derivative to characterize sensitivity. A second order central differencing scheme is used with stepsize $\Delta p_i = 0.1$ as this proves to be least sensitive to the effect of numerical noise introduced in the numerical integration (see Appendix A.0.3).

Important in this analysis is the definition of the feasible range of model parameters. The solution space was again chosen to encompass the minimum and maximum orders of magnitude depicted in Table 1. In order not to discriminate between the multiple orders of magnitude wherein the parameters can occur, values were collected from a loguniform distribution. A parameter interval sampling size of 5000 was used as this showed to provide reasonable convergence in parameter sensitivities (see Figure 4,5). Within the wide feasibility range of parameter values a large variation of cantilever and surface dynamics can be observed. As a consequence of the random sampling within a wide range, anomalies are sporadically observed in the dynamcis. Such anomalies generally involve phenomena where the cantilever dynamics does not resemble the tapping behavior we see in experiments. Under these circumstances the cantilever remains in contact with the sample during the entire pixel time.

The behavior of the moving surface model is characterized by the calibrated quantities ω_0, Q and k, and the effective driving force F'_{drive} on the cantilever. The

sensitivity analysis was performed with those quantities determined from two cantilevers and scanning conditions used in experiments. The amount of anomalies encompassed 7% and 8% of the entire sample size, respectively. These anomalies show large distortions in cantilever dynamics, and hence, introduce large sensativities having considerable influence on the overal result. As those phenomena are not of interest in Tapping Mode operation they are discarded in the analysis.

In order to make a statistical claim regarding parameter sensitivities it would be necessary to perform the analysis with 5000 samples many times. However, this would be almost impossible. For this reason bootstrap resampling was used to determine 95% confidence intervals for the sensitivity data of the parameters. In accordance with Nossent et al. (2011)[13] the samples were 1000 times resampled. This proved to be sufficient as complementary values were obtained after resampling, as can be validated in Table 3, 2.

Figures 4 and 5 show the mean sensitivity of all parameter values in the analysis for increasing sample size. By insecting both images it is clear that the high quality-factor cantilever with larger driving force shows a higher overall sensitivity to the parameter values. Regarding the parameters, it is clear that both damping parameters η_s and η_v show little influence on the overall mean sensitivity. An obvious correlation is observed between F_{ad} and k_s in both experiments. This hints at the influence of contact formation δ_∞. Figure 5 shows that for higher cantilever eigenfrequency f_0 the effect of F_{ad} en k_s is enforced. This can be attributed to a large contact formation in combination with a relatively slow retardation time. Interestingly, the bulk stiffness seems to have the largest contribution for higher scanning operation with higher driving force, generating larger compressive stresses.

One might argue that the overall low sensitivity of the damping parameters is due to too low parameter values. However, with the purposefully chosen large range of parameter values, the viscoelatic characteristics of importance τ_s, τ_v and τ_c can encompass more than six orders of magnitude being almost symmetrically distributed around the cantilever resonance f_0.

Table 2 and 3 both present a systematic low mean sensitivity for the damping parameters η_s and η_v as 95% confidence intervals of mean sensitivity of both parameters do not show any overlap with the other parameters. As a matter of fact, Table 2 shows a consistent difference between mean sensitivity in k_v, k_s,F_{ad} and η_s,η_v of

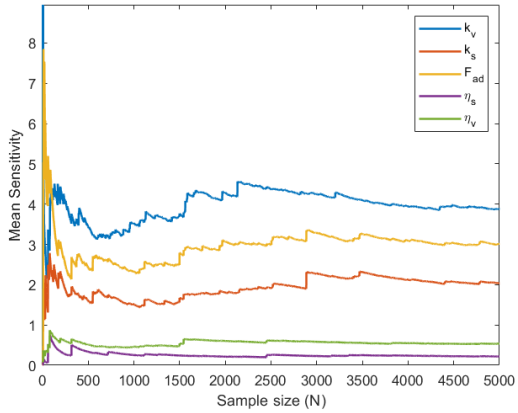

Figure 4: Parameter sensitivity analysis for 5 free parameters k_v, k_s, F_{ad}, η_s, η_v. Displayed is the convergence of mean sensitivity for increasing sample size, representing 5000 parameter sets $\boldsymbol{p}$. Scanning properties: $f_0 = 150$ kHz, $Q = 625$, $k = 27.12$ N/m, $|F'_{\mathrm{D}}(\omega_1)| = 2.091$ nN.

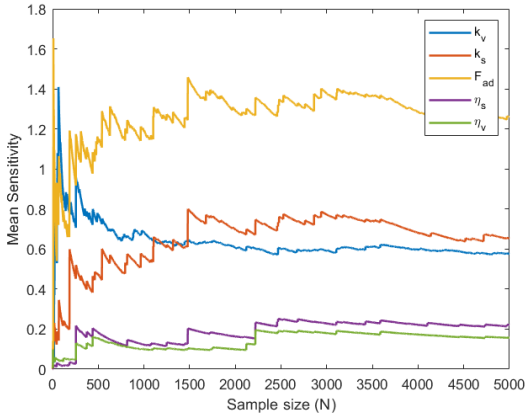

Figure 5: Parameter sensitivity analysis for 5 free parameters k_v, k_s, F_{ad}, η_s, η_v. Displayed is the convergence of mean sensitivity for increasing sample size, representing 5000 parameter sets $\boldsymbol{p}$. Scanning properties: $f_0 = 163$ kHz, $Q = 491$, $k = 23.95$ N/m, $|F'_{\mathrm{D}}(\omega_1)| = 1.385$ nN.

approximately one order of magnitue. The standard deviation data also shows a consistent high variability surmounting the mean values with approximately one order of magnitude, as well. This large variability explains the dispcrepency in parameter sensitivity observed in just 15 parameter sets. These observations with two different scanning modes hint at an inherent

Table 2: *Sensitivity Analysis for N = 5000 samples. Cantilever properties:* $f_0 = 150kHz$, $Q = 625$, $k = 27.12N/m$

Parameter	Mean	Bootstrap average	95% Confidence Interval	Standard Deviation	Bootstrap average	95% Confidence Interval
F_{ad}	3.012	3.012	2.532 - 3.700	20.62	20.24	15.81 - 32.48
k_v	3.879	3.865	3.401 - 4.551	20.41	20.31	15.58 - 31.27
k_s	2.038	2.047	1.657 - 3.061	20.89	19.44	11.32 - 39.79
η_s	0.2201	0.2183	0.1578 - 0.3319	2.955	2.847	1.924 - 4.738
η_v	0.5361	0.5323	0.4597 - 0.7024	4.007	3.832	2.102 - 6.531

Table 3: *Sensitivity Analysis for N = 5000 samples. Cantilever properties:* $f_0 = 163kHz$, $Q = 491$, $k = 23.95N/m$

Parameter	Mean	Bootstrap average	95% Confidence Interval	Standard Deviation	Bootstrap average	95% Confidence Interval
F_{ad}	1.2597	1.2582	1.041 - 1.5714	9.305	9.127	7.288 - 12.89
k_v	0.5760	0.5757	0.5037 - 0.6757	2.865	2.834	2.330 - 3.917
k_s	0.6530	0.6529	0.4888 - 0.8939	7.178	7.015	5.445 - 10.46
η_s	0.1406	0.2191	0.1406 - 0.3640	3.844	3.727	2.507 - 6.868
η_v	0.1569	0.1565	0.1021 - 0.2944	2.843	2.686	1.423 - 5.755

model characteristic, showing low average influence of interaction and surface damping parameters and high variability in parameter sensitivity.

Raman et al. have shown that local dynamic stiffness and damping can be measured from harmonics.[12] As a way to overcome the absence of parameter sensitivity, the sensitivity of higher harmonics generated in the dynamics of the moving surface model could be investigated.

6. Global optimization

The moving surface model can behave in a variety of ways within many different parameter regimes. The behavior of the moving surface model is described by a combination of relations between parameters that often can not be singled out to describe the behavior of one particular response. Now that a feasibility range has been established for all parameter values, it is possible to discard the trial and error procedure associated with local optimization routines and focus on global optimization.

The parameter space encompasses parameter values ranging within many orders of magnitude. It is therefore of great interest to limit these boundaries using a priori knowledge of the model behavior. In this sense, again quadrature curves could be utilized to define a subspace with lower dimensions. However, in the first place it is attempted to evaluate global optimization in the entire parameter range.

Multiple global optimization routines were evaluated for a view standard parameter sets. Two methods were able to find global minima in this large solution space. These methods are so-called heuristic methods inspired by nature: Genetic Algorithm (GA) and Particle Swarm Optimization (PSO). Both methods are non-gradient search algorithms that optimize by evolution and selection of the fittest (GA) or use social interaction among particles (PSO). Both techniques are stochastic methods as their algorithms incorporate randomness in the search procedure.

As it was shown that local parameter redundancy is an inherent property of the model, the performance of both methods is not compared in terms of error in parameter value but rather in final objective function value for the same 15 parameter sets applied for local optimization. For a fair comparison, both particleswarm and genetic algorithm were optimized starting from the same initial 'swarm' or 'population' constisting of a standard amount of 50 identical parameter sets. Figure 6 shows a comparison of the erorr E in final function value obtained for all 15 optimal parameter sets.

By inspecting Figure 6 one could observe that PSO

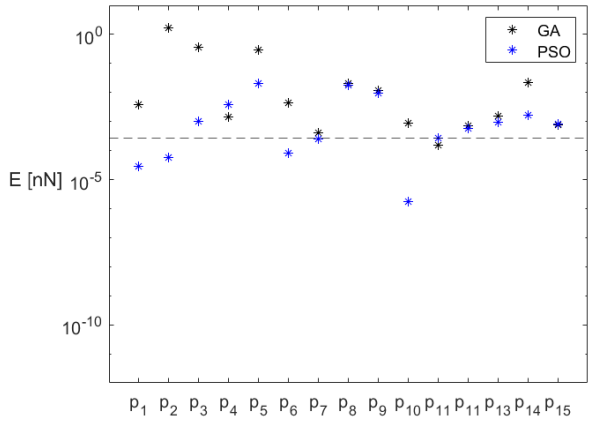

Figure 6: Performance of Genetic Algorithm (GA) versus Particle Swarm Algorithm (PSO) for 15 synthetic parameter sets $\boldsymbol{p}_1$-$\boldsymbol{p}_{15}$. The error E quantifies the difference between the force spectrum $\hat{F}_{ts,sim}$ of the best-fit and optimum. The dotted line indicates the performance of parameter set 11, chosen as indicator of a good fit.

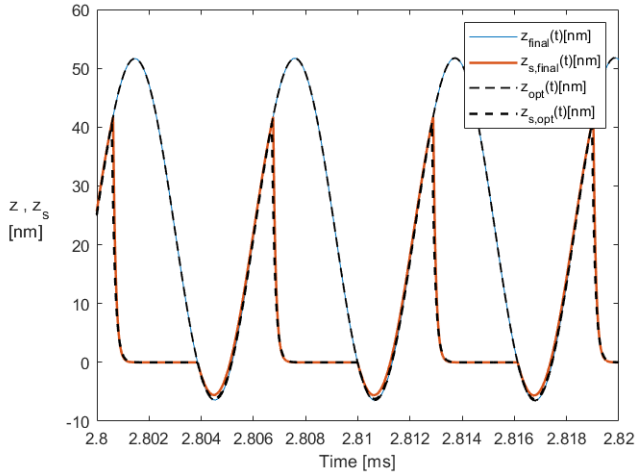

Figure 7: Cantilever and surface dynamics of Parameter set 11. z_{final} and $z_{s,final}$ represent the respective cantilever and surface motion obtained in a global optimization routine using Particle Swarm Optimization (PSO). z_{opt} and $z_{s,opt}$ represent the respective cantilever and surface motion of the optimum, being parameter set 11. With final parameters $k_v = 0.11$ N/m, $k_s = 0.010$ N/m, $F_{ad} = 0.21$ nN, $\eta_s = 0.0010$ mg/s and $\eta_v = 0.156$ mg/s and optimal parameters $k_v = 0.55$ N/m $k_s = 0.010$ N/m, $F_{ad} = 0.22$ nN, $\eta_s = 0.0013$ mg/s and $\eta_v = 0.65$ mg/s.

shows the better performance over 15 examinations. The mean error of GA measures mean$(E) = 0.16$ nN and of PSO amounts mean$(E) = 0.0039$ nN. However, not in all cases the global optimum could be found.

Figure 7 shows the behavior of the model for parameter set 11 and its associated final best-fit. Here, the parameter set is characterized by an error in stiffness k_v and damping η_v with respect to the optimum generating an error in τ_v of 20%. However, with a blind eye the difference in surface motion is almost unnoticable. The error $E = 2.7010^{-4}$ nN associated with this parameter set represents a moderate treshold for a descent fit. Five optimization procedures surpassed this criterion indicated by a dotted line in Figure 6.

In order to improve the efficiency and performance of the optimization it is of interest to reduce the solution space as much as possible. In this way the chance of finding the global minimum is increased and the required amount of function evaluations reduced. In practice, the system behavior can be described by relative contributions of individual parameters. For example, the ratio between stiffness parameters k_s and k_v indicates whether there will be a high surface lift or a more solid-like interaction.[2] However, it is hard to translate such ratios in terms of boundaries for individual parameters.

By looking at the additional information that the force in a simulation can provide over the experimental force it is possible to establish a reasonable estimation of the adhesion force F_{ad} trough the in-phase force quadrature $F_I(A)$ (see Appendix A.1.2). Although in experiments we only obtain a partial force through a linear transfer function, in a simulation the interaction force F_{ts} can be determined from the numerical integration. Hence, in a simulation we are able to describe the interaction force on the fast time scale of oscillation. Due to the rapid oscillations around f_0 combined with a slowly modulation envelope function, the very first tap into the material will generally show insignificant indentation, implying $s = 0$. Because of this, the conservative interaction force will be described solely by F_{ad}. As we are able to estimate the static probe height from the quadrature curves as well we are able to determine $F_I(A)$ during the first interaction. However, there is uncertainty involved with the approximation of the force impulse during interaction. The adhesion force is estimated from the area under the impusle function

described in time. As such the error in the estimation of F_{ad} is directly related to the error in the estimation of the area under the impulse. This error determines the bounds wherein one would need to optimize F_{ad}.

7. Experimental Characterization

In this research two different samples are investigated. One polymer blend consisting of polystyrene and polybutadiene (PS-PB) and one polymer blend consisting of Polystyrene and Polyolefin Elastomer (ethylene-octene copolymer) (PS-LDPE). Images of both samples have been obtained with ImAFM.

7.1. Characterization PS-PB

Figure 8 shows a scan on a PS-PB sample. It is characterized by stiff PS islands surrounded by a soft PB matrix. We analyze the properties of the soft polybutadiene bulk for three different pixels. In the experiment the force-quadrature curves $F_I(A)$ and $F_Q(A)$ are determined from the quadrature components of the intermodulations. Figure 10 (a)(b) show $F_I(A)$ and $F_Q(A)$ obtained on the polybutadiene region. The quadrature-curves show a large attractive force in F_I and large dissipation in F_Q, associated with the soft PB. Using the PSO algorithm, experimental data is reconstructed in a global optimization routine. Table 4 shows the parameters obtained in the optimization for the three different pixels. The optimization outcomes show consistency in the parameters of the interaction force k_v, k_s and F_{ad}. The tip-sample interaction seems to be dominated by high F_{ad} and k_v, representing the interplay of high attractive surface forces and high repulsive forces in the bulk.[2] However, there is a large variability in surface parameters η_s and k_s with values ranging many orders of magnitude. Hence, the retardation time seems to vary between $\tau_s = 0.4\ s$ and $\tau_s = 7.8 \cdot 10^{-11}\ s$. The surface motion with fast retardation time is displayed in Figure 10 (c)(d). For the other pixels with slightly higher error E and slow retardation time, standing surface waves are generated with small amplitudes ($\sim$ 0.2 nm) (see Appendix A.2).

Hence, using global optimization we do obtain descent fits for different optima, where complementary values are obtained for three parameters. However, significant deviations are found in best-fit values for the surface parameters k_s and η_s. As a consequence, the sensitivity values S were analyzed for the optimum found in the fitted pixels. For pixel (144,219) we find $S_{k_s} = 0.09$, $S_{\eta_s} = 0.00012$, in contrast with $S_{k_v} = 4.04$,

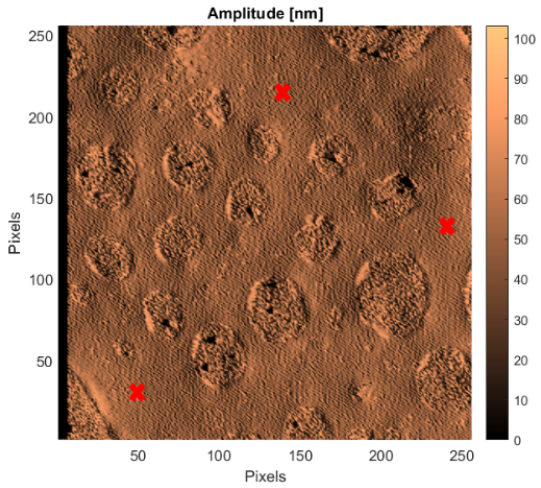

Figure 8: Amplitude image at each of the 256×256 pixels of $10\mu m \times 10\mu m$ PS-PB. Cantilever properties: $f_0 = 163kHz$, $Q = 491$, $k = 23.95N/m$. Crosses $\times$ indicate the pixels that are investigated for reconstruction.

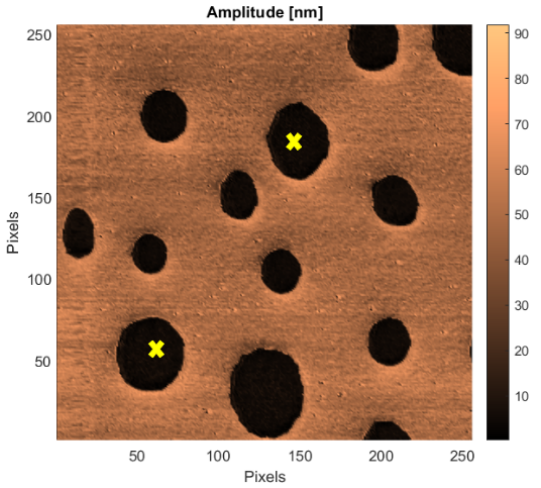

Figure 9: Amplitude image at each of the 256×256 pixels of $10\mu m \times 10\mu m$ PS-LDPE. Cantilever properties: $f_0 = 150kHz$, $Q = 625$, $k = 27.12N/m$. Crosses $\times$ indicate the pixels that are investigated for reconstruction.

$S_{F_{ad}} = 4.41$ and $S_{\eta_v} = 0.59$ showing much higher influence around the optimum. Similarly, for pixel (50,20) we find $S_{k_s} = 0.00060$ and $S_{\eta_s} = 0.0064$, in contrast with $S_{k_v} = 1.39$, $S_{F_{ad}} = 1.17$ and $S_{\eta_v} = 0.30$, as is also made visible in the Appendix A.2. Thus, the discrepancy in k_s and η_s goes hand in hand with a low sensitivity

Table 4: Fitted parameters obtained using PSO for three pixels on PB matrix. Where the driving force is indicated by the force component of the first drive frequency $F_d = |F'_D(\omega_1)|$. The error E defines the error between the Force fourier components in the simulated best-fit and experiment (see Equation 14), and hence, indicates the performance of the optimization.

Pixel	h (nm)	F_d (nN)	k_v (N/m)	k_s (N/m)	F_{ad} (nN)	η_v (mgs^{-1})	η_s (mgs^{-1})	Error E (nN)
(144, 219)	22.11	1.385	6.820	17.65	13.76	0.5283	0.001378	0.1131
(240, 135)	22.74	1.397	6.416	0.004440	12.86	0.4133	1660	0.1437
(50, 20)	22.64	1.376	6.153	0.01273	12.27	0.5436	533.0	0.1567

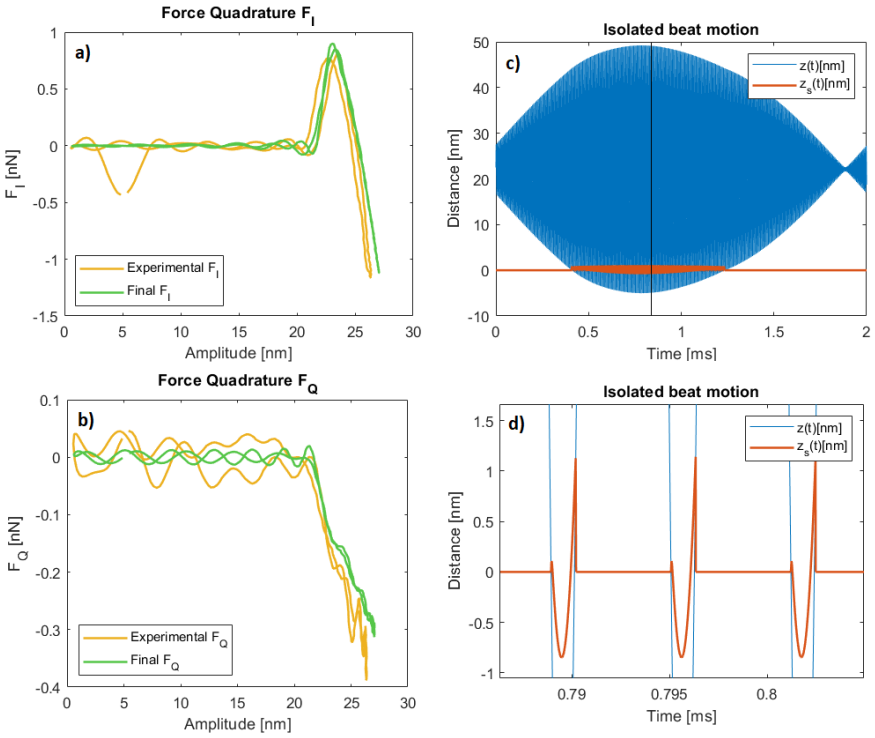

Figure 10: Best-fit results for (144,219) with Error E = 0.1131 nN. Experimental observation of (***a***) In-phase force quadrature $F_I(A)$ describing conservative interaction. Experimental $F_I(A)$ plotted against the final $F_I(A)$ obtained in PSO method. (***b***) Dissipative force quadratures $F_Q(A)$ obtained in experiment and final $F_Q(A)$ obtained in optimization. (***c***) The dynamics of the best-fit simulated tip-sample interaction, (***d***) zoomed in on the surface motion at the black intersection shown in (***c***). Sensitivity analysis: $S_{k_v} = 4.04$, $S_{k_s} = 0.09$, $S_{F_{ad}} = 4.41$, $S_{\eta_s} = 0.00012$ and $S_{\eta_v} = 0.59$.

description of the parameters.

Evidently, the question remains whether the optimization delivered a global optimum. For PB-matrix we find a low Error $E = 0.1131$ nN for pixel (144,37), relative to the other two pixels representing the same material characteristic. It is verified that the best parameter set presents a higher error for the other two pixels with an error $E = 0.1878$ nN for pixel (50,20) and an error of $E = 0.2824$ nN for pixel (240,135). This is a positive indication that we cannot simply rejected that the solutions represents a global minima. Moreover, the magntitude of the errors are in agreement with Forchheimer et al.[7] where minimum errors of $E = 0.172$ nN were reported for experimental fits on PS-LDPE sample obtained in a

Table 5: Fitted parameters obtained using PSO for two pixels on LDPE islands. Where the driving force is indicated by the force component of the first drive frequency $F_d = |F'_D(\omega_1)|$. The error E defines the error between the Force fourier components in the simulated best-fit and experiment (see Equation 14), and hence, indicates the performance of the optimization.

Pixel	h (nm)	F_d (nN)	k_v (N/m)	k_s (N/m)	F_{ad} (nN)	η_v (mgs^{-1})	η_s (mgs^{-1})	Error E (nN)
(174, 186)	24.75	2.091	0.01000	4.741	14.99	1.244	1.538	0.2816
(64, 52)	27.08	2.098	0.01183	1.238	14.99	0.9595	2.6144	0.294

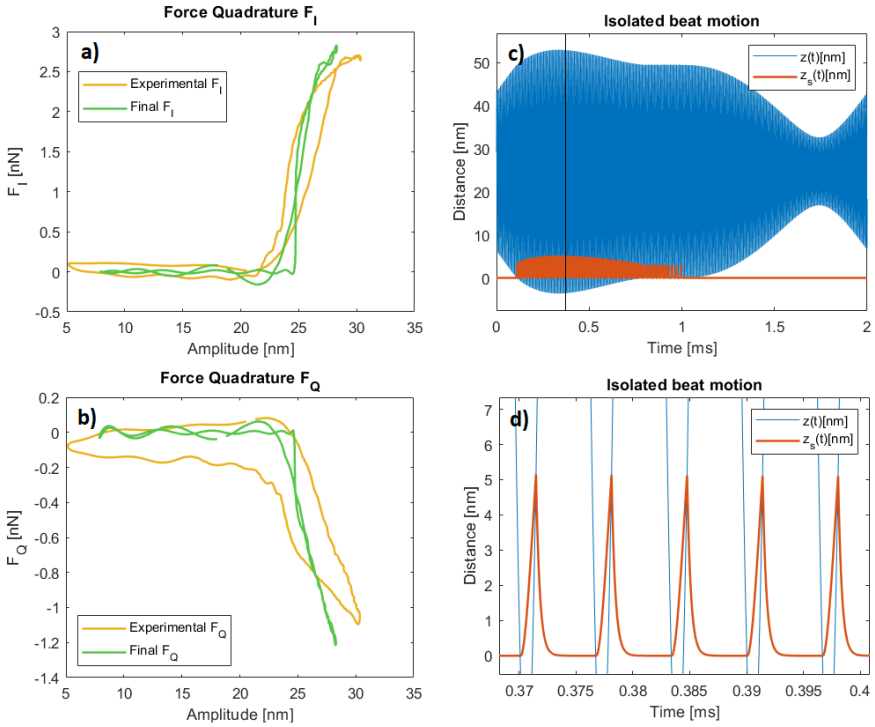

Figure 11: Best-fit results with Error E = 0.2816 nN. Experimental observation of (***a***) In-phase force quadrature $F_I(A)$ describing conservative interaction. Experimental $F_I(A)$ plotted against the final $F_I(A)$ obtained in PSO method. (***b***) Dissipative force quadratures $F_Q(A)$ obtained in experiment and final $F_Q(A)$ obtained in optimization. (***c***) The dynamics of the best-fit simulated tip-sample interaction, (***d***) zoomed in on the surface motion at the black intersection shown in ***c***). Sensitivity analysis: $S_{k_v} = 2.36$, $S_{k_s} = 1.25$, $S_{F_{ad}} = 10.1$, $S_{\eta_s} = 0.60$ and $S_{\eta_v} = 0.608$.

local minimization routine.

7.2. Characterization PS-LDPE

Figure 9 shows a scan on a PS-LDPE sample. We investigate the mechanical properties of the soft polyolefin elastomer (LDPE) islands. While Figure 8 shows lower contrast in amplitude between PS islands and PB matrix, Figure 9 shows strong contrast between PS and LDPE regions. In Figure 11(a)(b) observing force quadratures $F_I(A)$ and $F_Q(A)$ obtained on the polybutadiene pixel (174,186), the interaction is dominated by attractive forces that induce large dissipation.

From Figure 11(a)(b) one can derive that the initial height estimation in this proceeding is off about 2.5 nm. This is explained by the experimental force quadratures that exist at amplitudes of 5 nm, while the fitted model displays interactions at slightly higher amplitudes.

The parameters in Table 5 indicate the parameters

found using PSO optimization to characterize the material at pixel (174, 186) and pixel (64, 52). Here the optimization outcomes again show large consistency in k_v and F_{ad}. Instead of the high bulk stiffness values that were found for suposedly soft PB matrix, LDPE show low bulk stiffness values for k_v.

The viscoelastic behaviors presented at both pixels show identical behaviors. It is also apparent when we compare the sensitivity characteristics of both optima. For pixel (174, 186) we find $S_{k_v} = 2.36$, $S_{k_s} = 1.25$, $S_{F_{ad}} = 10.1$, $S_{\eta_s} = 0.60$ and $S_{\eta_v} = 0.608$, where pixel (64, 52) shows $S_{k_v} = 1.61$, $S_{k_s} = 0.69$, $S_{F_{ad}} = 10.46$, $S_{\eta_s} = 0.75$ and $S_{\eta_v} = 0.698$. It must be noted that the error in the height estimation of about 2.5 nm in these proceedings may affect the correctness of the obtained parameter values.

As the sensitivities indicate, the dynamics is dominated by mostly the adhesion force, resulting in a significant beat distortion of the cantilever motion (see Fig. 11(c)); Even when the cantilever tries to detach from the surface it is pulled back generating a second turn in the beat shape of the cantilever motion.

8. Conclusions

Using ImAFM viscoelastic characterization of soft samples is performed. The simple moving surface model was used to describe independent surface motion, which is essential in viscoelastic materials. It was shown that intrinsic model behaviors hinder the performance of optimization methods. As a consquence, a thorough analysis of the model characteristics was performed, determining parameter sensitivity for a large dataset. Parameter sensitivity characteristics were obtained that showed a systematic low influence of damping parameters and large standard deviations for all parameters approximating ten times the mean sensitivity values. A strong contribution of adhesion force in combination with low interaction and surface damping characteristics implies a dominant contribution of high surface amplitudes in the dissipation mechanism of the model.

The moving surface model possesses at least 5 free parameters. Finding a good fit with experiment using trial and error is not trivial. Hence, a feasible range of parameters was established so that global optimization could be performed. Particle Swarm Optimization proved to be able to show descent convergence, adequatly resembling quadrature curves describing the characteristics of the tip-sample interaction. The fitted parameters showed consistent values for the parameters that showed highest influence on the objective. However, it cannot be confirmed that global minima have been found in the experiments.

Using PSO in a large parameter space requires a lot of function evaluations. By narrowing down this domain the speed and robustness must significantly increase for PSO. It has been attempted to provide a feasible parameter space reduction for a single variable.

Of great interest is the analysis of the adaptation of the surface model on the sensitivity behavior. However, one first needs to establish a feasibility range associated with free parameters of those models.

References

[1] Y.M. Efremov, T. Okajima and A. Raman. Measuring viscoelasticity of soft biological samples using atomic force microscopy, *Soft matter*, 2020.

[2] P. Thoren, R. Borgani, D. Forchheimer, I. Dobryden, P.M. Claesson, H.G. Kassa, P. Leclère, Y. Wang, H.M. Jaeger and D.B. Haviland. Modeling and Measuring Viscoelasticity with Dynamic Atomic Force Microscopy, *Physical Review Applied* 10(2):024017, 2018.

[3] B. Rajabifar, J.M. Jadhav, D. Kiracofe, G.F. Meyers and A. Raman. Dynamic AFM on Viscoelastic Polymer Samples with Surface Forces, *Macromolecules*, 2018.

[4] D.B. Haviland. Quantitative force microscopy from a dynamic point of view, *Current Opinion in Colloid & Interface Science*, 27:74-81, 2017.

[5] R. Borgani, P. Thorén, D. Forchheimer, I. Dobryden, S.M. Sah, P.M. Claesson, D.B. Haviland. Background-force compensation in dynamic atomic force microscopy, *Physical Review Applied* 7(6):064018, 2017

[6] D.B. Haviland, C.A. van Eysden, D. Forchheimer, D. Platz, H.G. Kassa and P. Leclère. Probing viscoelastic response of soft material surfaces at the nanoscale, *Soft matter* 12(2):619-624, 2015

[7] D. Forchheimer. Imaging materials with intermodulation: Studies in multifrequency atomic force microscopy, PhD thesis, KTH Royal Institute of Technology, 2015

[8] D. Forchheimer, R. Forchheimer and D.B. Haviland. Improving image contrast and material discrimination with nonlinear response in bimodal atomic force microscopy, *Nature communications* 6:6270, 2015.

[9] S.S. Borysov, D. Platz, A.S. de Wijn, D. Forchheimer, E.A. Tolén, A.V. Balatsky and D.B. Haviland. Recon-

struction of tip-surface interactions with multimodal intermodulation atomic force microscopy, *Physical Review B* 88(11):115405, 2013.

[10] D. Platz, D. Forchheimer, E.A. Tholén, and D.B. Haviland. Interaction imaging with amplitude-dependence force spectroscopy, *Nature communications* 4:1360, 2013.

[11] D. Forchheimer, D. Platz, E.A. Tholén, Erik A and D.B. Haviland. Model-based extraction of material properties in multifrequency atomic force microscopy, *Physical Review B* 85(19):195449, 2012.

[12] A. Raman, S. Trigueros, A. Cartagena, A.P.Z. Stevenson, M. Susilo,E. Nauman, S. Contera and Antoranz. Mapping nanomechanical properties of live cells using multi-harmonic atomic force microscopy, *Nature nanotechnology* 6(12):809, 2011.

[13] J. Nossent, P. Elsen and W. Bauwens. Sobol' sensitivity analysis of a complex environmental model, *Environmental Modelling & Software* 26(12):1515-1525, 2011.

[14] E.A. Tholén, D. Platz, D. Forchheimer, V. Schuler, M.O. Tholén, C. Hutter and D.B. Haviland. Note: The intermodulation lockin analyzer, *v* 82(2):026109, 2011.

3

Conclusions & Recommendations

3.1. Conclusions

The goal of this thesis was to enhance viscoelastic characterization using ImAFM. Existing techniques require recursive evaluation of the model and good intuition to fit only one single point of a specimen. It was analyzed whether a more automatic approach could be formulated to perform experimental reconstruction. To do so, a toolbox has been developed to perform numerical simulations of the moving surface model and global optimization.

The moving surface model was investigated to obtain a better understanding of the influential and redundant physical processes in the model dynamics. Using sensitivity analysis the model has been evaluated for a large range of model parameter values. Parameter sensitivities were obtained that showed a systematic low influence of damping parameters and large standard deviations in mean sensitivity values. We found that the dissipation mechanism in the moving surface model on average is dominated by high meniscus forming of the surface on the tip, instead of interaction damping.

Global optimization has been performed with a variety of Global Optimization methods available in the Global Optimization Toolbox in MATLAB. Two Heuristic optimization methods known as Genetic Algortihm and Particle Swarm Optimization showed descent performance on standard parameter sets. Hence, both methods were evaluated and Particle Swarm Optimization consistently showed the best performance in synthetic data analysis.

In the experimental procedure two different soft samples were investigated. Using the Particle Swarm Algorithm optimization was performed in a large feasibility range of parameter values. The quality of the fits was quantitatively compared with results in the literature and showed to be competible.

3.2. Recommendations

In this thesis global optimization was performed using Particle Swarm Optimization (PSO). In the experimental characterization PSO algorithm required a minimum and maximum amount of 3450 and 7000 function evaluations, respectively (see Appendix A.1.1). For the simulations the ode 45 solver in MATLAB was employed, so that a minimum amount of approximately 8 seconds was required for each function evaluation (see Appendix C.1.1). However, the numerical solver ocasionally showed to slow down significantly. Therefore, the experimental optimization routines typically took one week to reach the optimum which is highly impractical. It is recommended to try implementing the CVODE solver [13] as it proves to show a large increase in simulation time for the moving surface model.

The PSO algorithm is characterized by an algorithm depicted in Appendix A.1.1. The algorithm describes a scheme that updates particle velocities in a random manner. These particles represent possible solutions in search for a global optimum. Although the method incorporates randomness, it is also characterized by parameters that determine whether individual particles search for the optimum in a more social or individual

manner. These parameters can and have sporadically been adapted in this research as a test case. However, it is worth investigating whether a best set of behavioral parameters could be found by use of an overlaying optimizer in a procedure knwon as Meta-optimization [57].

The moving surface model is simplistic, and hence, there are many things that can be included in the model to make it more comprehensive. However, this would almost most certainly go at the cost of multiple free parameters. As a limitation, it was demonstrated that in the model surface damping and internal damping on average have little effect in the tip-sample interaction. For this reason it might be of interest to investigate the introduction of more fluidic viscoelastic models. So-called Jeffrey models are three element viscoelastic models that incorporate two damper elements. With these models a more balanced effect may be observed in the dissipation process of the model.

From force quadratures F_I and F_Q it is possible to derive the nature of the tip-sample interaction. Solution space reduction is of great interest in optimization procedure. Therefore, it would be useful to exploit the information in the quadrature curves to estimate reasonable parameter values. However, using quadrature curves for this purpose is not straightforward as the interaction is described by a number of processes that are more or less influenced by different parameters. Using a (machine learning) algorithm capable of correlating patterns in F_I and F_Q for many parameter sets, it may be possible to provide reasonable estimates of parameter values. Then, it would be possible to shrink down the optimization domain to regions with narrowness determined by the accuracy of the algorithm.

Raman et al. have shown that local dynamic stiffness and damping can be measured from harmonics [58]. As a way to overcome the absence of parameter sensitivity it was attempted to look into the harmonics generated in the dynamics of the non-smooth two-body impact dynamics of the moving surface model. Especially of interest are the higher harmonics coinciding with higher modes. In Multimodal ImAFM [59] the excitation of multiple eigenmodes might lead to mixed modes in additional frequency bands. Hence, investigating the properties of the harmonics is a reasonable attempt to find new information channels for the parameters. Using one single mode parameter sensitivities were analyzed for the amplitudes of the first 20 harmonics in the cantilever dynamics. The second, third and fourth harmonics show similar sensitivities for all parameters. The other harmonics, however, show a strong sensitivity with respect to paremeters F_{ad} and k_s.

In a sensitivity analysis, sensitivity values of 5 model parameters of the moving surface model have been quantified for the least-square error of all intermodulations combined. However, no attention has yet been payed to contributions of the individual intermodulations. According to the experimental findings of Forcheimer et al., large image contrast was found on PS–LDPE sample especially for off-resonant intermodulations [60]. Hence, once a constistent sensitivity can be found for particular parameters , they can be related to particular tone(s).

A

Sensitivity Analysis

A.0.1. Parameter Range

In a sensitivity analysis the mean sensitivity values of free parameters in the moving surface model have been evaluated. In this analysis a parameter range had to be established wherein the model parameters can exist. As we wish to analyze realistic model behavior, parameter values were chosen to be in similar order of magnitude as the parameters obtained by Thoren et al. (2018)[8], in experimental characterization of different soft samples. Table A.1 shows the minimum and maximum values of the model parameters found in their experimental characterization. The orders of magnitude are derived from the parameter bounds displayed in the Table A.1.

Parameter ranges Thoren et al. (2018)	Order of magnitude
$0.8459 \leq F_{ad}$ (nN) ≤ 4.665	$10^{-1} - 10^{1}$
$0.01400 \leq k_v$ (N/m) ≤ 6.144	$10^{-2} - 10^{1}$
$0.04690 \leq k_s$ (N/m) ≤ 32.53	$10^{-2} - 10^{2}$
$0.004229 \leq \eta_s$ (mgs^{-1}) ≤ 23.92	$10^{-3} - 10^{2}$
$0.01768 \leq \eta_v$ (mgs^{-1}) ≤ 2.067	$10^{-2} - 10^{1}$
$8.969 \leq h$ (nm) ≤ 39.08	-

Table A.1: Parameter range obtained by Thoren et al. [8]. Orders of magnitude are rounded off to the highest positive or negative order.

Particular parameter sets show dynamical behaviors that should not occur during a scanning procedure. In those cases the cantilever will stay immersed into the material during the entire pixel time. These phenomena cannot any longer be characterized as 'tapping mode' and they show high influence in sensitivity analysis with large sensitivity values. Therefore, the associated parameter sets are discarded in the sensitivity analysis. It is worth mentioning that some research procedures in live cells do involve continuous indentation during full oscillation cycles [58].

A.0.2. Histogram of parameter values

Table A.1 shows a feasible range of parameter values used in the moving surface model. In sensitivity analysis and optimization, one needs to collect parameter values within this range. In order to perform unbiased sampling we take a logarithmic uniform distribution:

$$\boldsymbol{p} = 10^{-\hat{\boldsymbol{l}}\boldsymbol{b}+(\hat{\boldsymbol{u}}\boldsymbol{b}-\hat{\boldsymbol{l}}\boldsymbol{b})U[0,1]}, \tag{A.1}$$

where lower bound $\hat{\boldsymbol{l}}_b = 10log(\boldsymbol{l}_b)$ and upper bound $\hat{\boldsymbol{u}}_b = 10log(\boldsymbol{u}_b)$ such that the parameter values $\boldsymbol{p}$ are uniformly distributed in a logarithmic sense over the many orders of magnitudes. The sample size is chosen to be $N = 5000$ parameter sets. Below, we display histograms showing how the obtained parameter sets are distributed throughout the feasible domain. The parameter sets that were initially collected are displayed in gray. The atypical parameters sets, or 'anomalies', showing undesirable surface lifts were removed from the analysis as described in section A.0.1. Furthermore, the analysis is performed under two different operating conditions with different set of scanning parameters.

The first scanning condition is characterized by a cantilever with an eigenfrequency $f_0 = 163$ kHz, a quality factor $Q = 491$, a stiffness $k = 23.95$ N/m an an effective driving force $|F'_{\mathrm{D}}(\omega_1)| = 1.385$ nN. For this operation the histograms are displayed in Fig. A.1 (a-e).

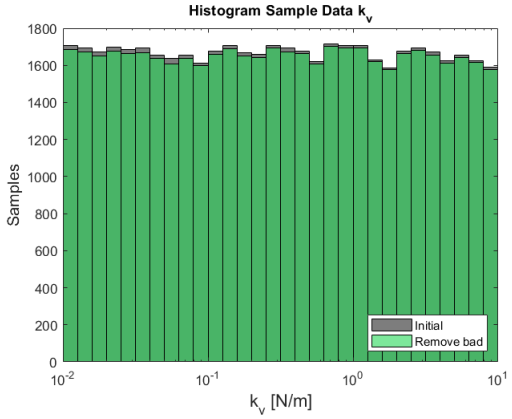

(a) Histogram k_v

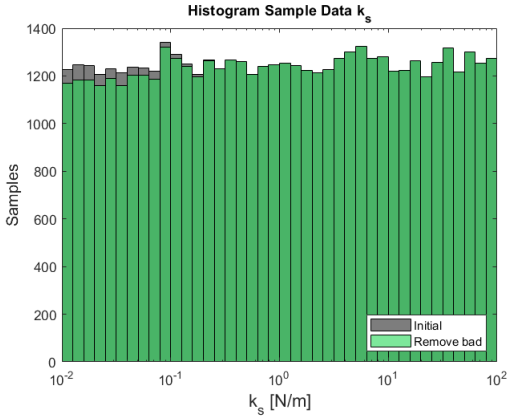

(b) Histogram k_s

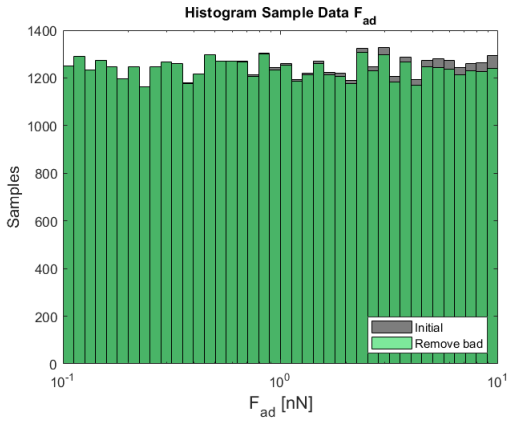

(c) Histogram F_{ad}

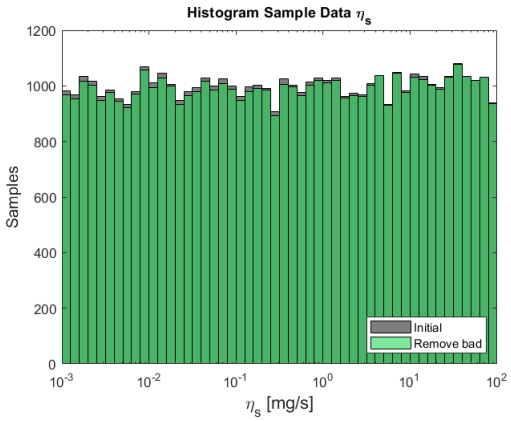

(d) Histogram η_s

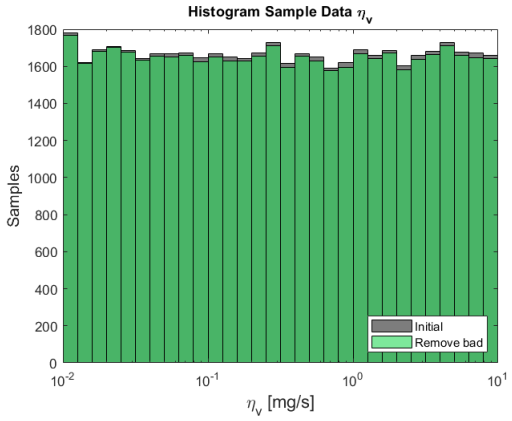

(e) Histogram η_v

Figure A.1 Histograms of parameter values for scanning condition 1 characterized by a cantilever with an eigenfrequency $f_0 = 163$ kHz, a quality factor $Q = 491$, a stiffness $k = 23.95$ N/m an an effective driving force $|F'_D(\omega_1)| = 1.385$ nN. Histograms describe the distribution over feasible domains of parameter values with 5 free parameters (k_v,k_s,F_{ad},η_s,η_v) of the Moving surface model. In gray are displayed the parameter distributions for the initial values collected from a loguniform distribution. Particular parameters sets describing anonomlous behaviors were removed. In green are displayed the histograms after the removal of the anomalies.

The second scanning condition is characterized by a cantilever with an eigenfrequency $f_0 = 150$ kHz, a quality factor $Q = 625$, a stiffness $k = 27.12$ N/m an an effective driving force $|F'_D(\omega_1)| = 2.091$ nN. For this operation the histograms are displayed in Fig. A.2 (a-e).

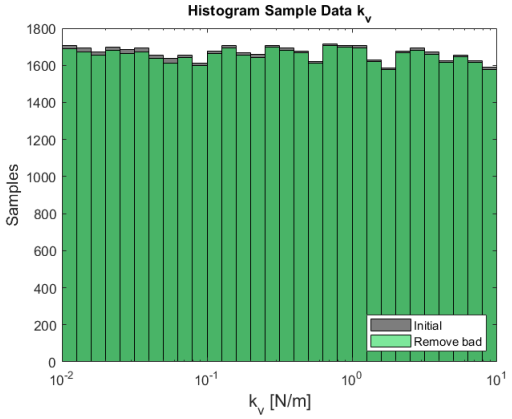

(a) Histogram k_v

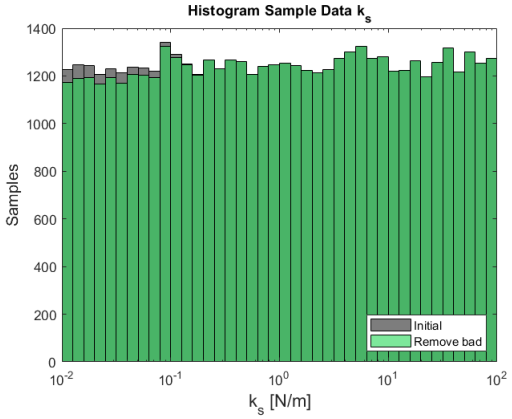

(b) Histogram k_s

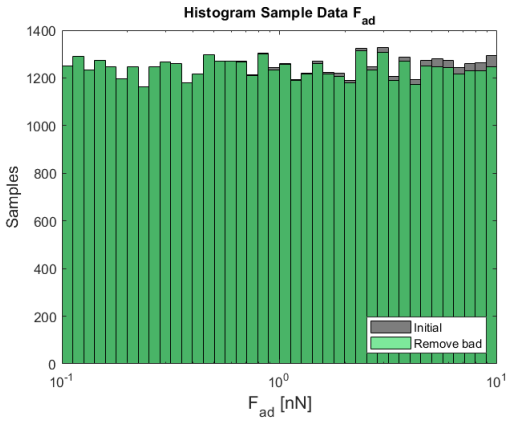

(c) Histogram F_{ad}

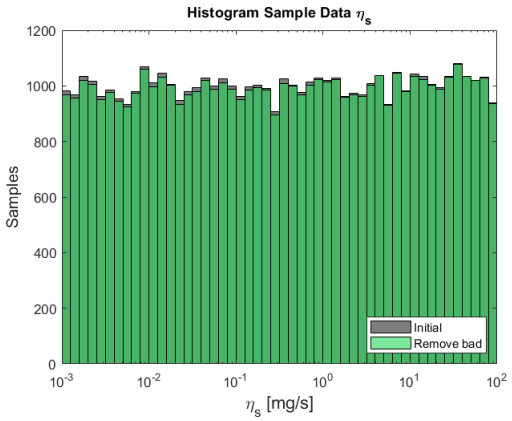

(d) Histogram η_s

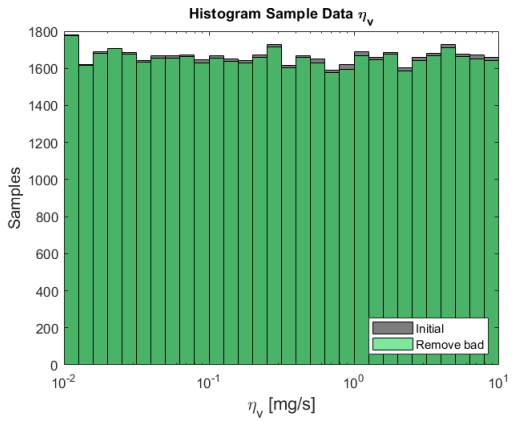

(e) Histogram η_v

Figure A.2 Histograms of parameter values for scanning condition 2 characterized by a cantilever with an eigenfrequency $f_0 = 150$ kHz, a quality factor $Q = 625$, a stiffness $k = 27.12$ N/m an an effective driving force $|F'_D(\omega_1)| = 2.091$ nN. Histograms describe the distribution over feasible domains of parameter values with 5 free parameters (k_v,k_s,F_{ad},η_s,η_v) of the Moving surface model. In gray are displayed the parameter distributions for the initial values collected from a loguniform distribution. Particular parameters sets describing anonomlous behaviors were removed. In green are displayed the histograms after the removal of the anomalies.

One can clearly observe in both Fig. A.1 and A.2 that for two scanning conditions mainly parameter sets with lower k_s values and higher F_{ad} values were removed. This indicates that a large ratio F_{ad}/k_s is influencing the interaction causing anomalous behavior. The asymptotic surface height is the maximum height that the surface approaches when it forms a capillary neck around a tip. This height can for soft interactions be approximated as $\delta_\infty \approx F_{ad}/k_s$ [8]. Hence, this implies a large influence of δ_∞ on the model behavior.

A.0.3. Truncation error / round-off error

In an attempt to determine how a sensitivity analysis can best be performed without influences of noise sources, an error analysis needs to be performed. In the error analysis it is analyzed for what stepsize in a finite differencing scheme truncation and round-off errors are least influential on the outcome.

In the sensitivity analysis a second order central differencing scheme is performed. We analyze the effect a perturbance of a model parameter p_i has on the objective function $\bar{f}(\boldsymbol{p})$ as function of the total parameter set $\boldsymbol{p}$. We present 5 model parameters k_v, k_s, F_{ad}, η_s and η_v. If one single parameter is slightly perturbed, we define a vector $\Delta\boldsymbol{p}$ with one nonzero component Δp. For a single parameter the central differencing scheme is defined as follows for :

$$S = \frac{\bar{f}(\boldsymbol{p}+\Delta\boldsymbol{p}) - 2\bar{f}(\boldsymbol{p}) + \bar{f}(\boldsymbol{p}-\Delta\boldsymbol{p}))}{\Delta p^2}. \tag{A.2}$$

Fig. A.3 shows the error analysis of the finite differencing scheme used to compute parameter sensitivities for 3 parameter sets. The round-off errors are being observed for values difference steps lower than 10^{-1}. At this stepsize truncation error were not observed. Hence, a stepsize of $\Delta p = 10^{-1}$ was taken to describe parameter purturbations in the sensitvity analysis. With this stepsize no negative sensitivities were found in 10^4 model evaluations.

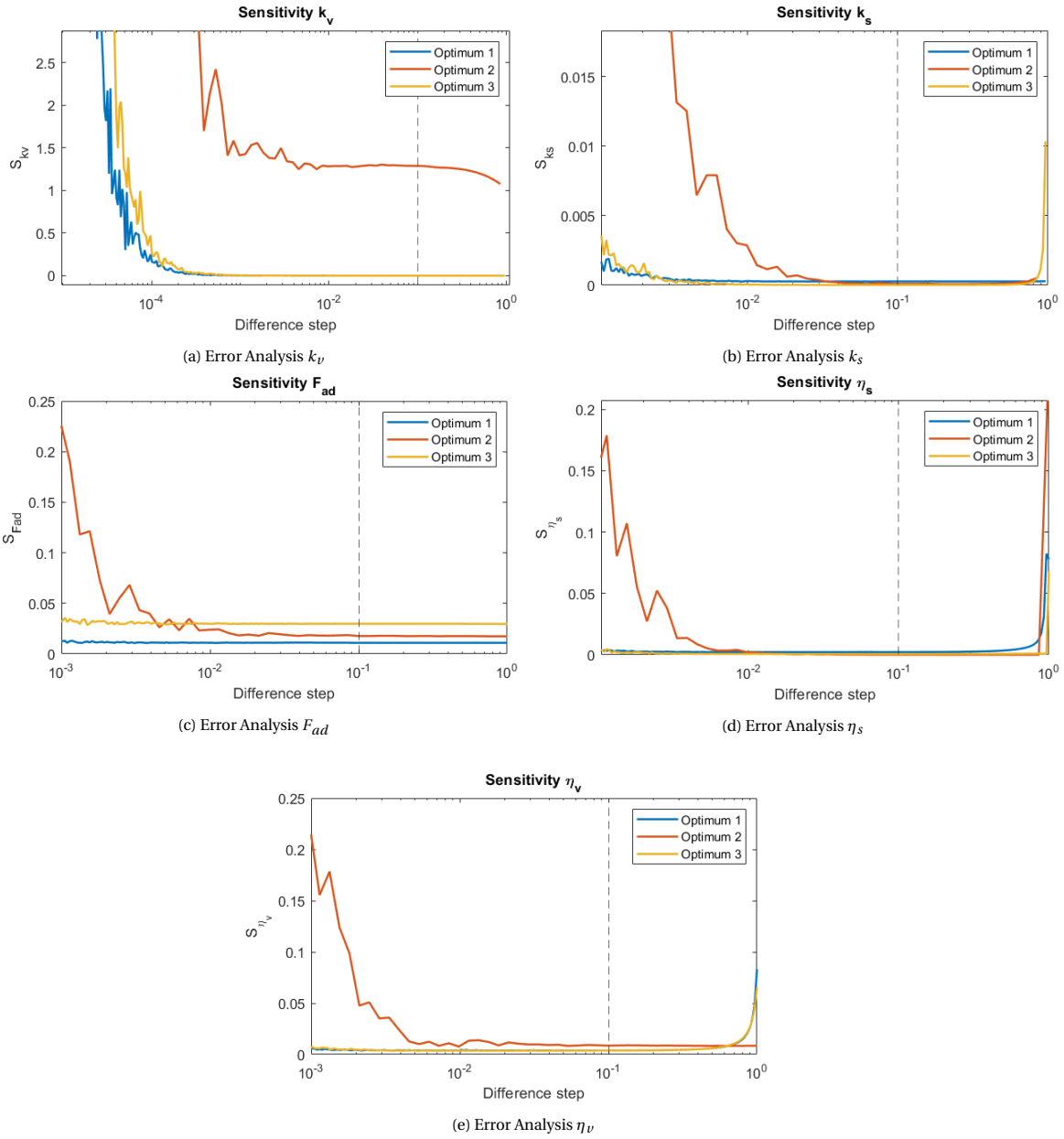

(a) Error Analysis k_v

(b) Error Analysis k_s

(c) Error Analysis F_{ad}

(d) Error Analysis η_s

(e) Error Analysis η_v

Figure A.3 Truncation and round-off error analysis displayed for three realistic parameter sets of the moving surface model. S represents the sensitivity calculated by a second order central differencing scheme for each individual parameter. The finite difference step used in the procedure is shown on the horizontal axis. We analyze 5 free parameters (k_v,k_s,F_{ad},η_s,η_v) of the Moving surface model.

A.1. Optimization

In this thesis optimization has been performed in a large solution space using so-called Global optimization methods. One method in particularly, Particle Swarm Algorithm (PSO) has been used to perform experimental characterization. In this section additional information is provided about the implementation of the algorithm and the strategies applied to improve it.

A.1.1. Particle Swarm Optimization (PSO)

The PSO algoritm adopted in MATLAB optimization toolbox is described in Eq. A.3 and A.4. In PSO, n particles in a swarm are initially positioned at random or predifined positions $\boldsymbol{x}_i$ in the feasible parameter range. In

the optimization procedure the velocities of individual particles $\boldsymbol{v}_i$ are updated to $\boldsymbol{v}_{i+1}$ taking into account personal best $\boldsymbol{p}_i$ and global best position $\boldsymbol{p}_g$ of the swarm. The method is based on swarm communication through $\boldsymbol{p}_g$, individual memory through $\boldsymbol{p}_i$ and randomness $U(0,1)$, in order to search a global minimum in the solution space.

$$\boldsymbol{v}_{i+1} = \omega \boldsymbol{v}_i + \hat{\phi}_p U(0,1)(\boldsymbol{p}_i - \boldsymbol{x}_i) + \hat{\phi}_g U(0,1)(\boldsymbol{p}_g - \boldsymbol{x}_i), \tag{A.3}$$

$$\boldsymbol{v}_{i+1} = \boldsymbol{x}_i + \boldsymbol{v}_i. \tag{A.4}$$

The algorithm incorporates weighting factors represented by the inertia $\hat{\omega}$, self adjustment weight $\hat{\phi}_p$ and social adjustment weight $\hat{\phi}_g$. The optimization has been performed using values depicted below:

$$n = 50,\ \hat{\omega} = [0.1, 1.1],\ \hat{\phi}_p = \hat{\phi}_g = 1.49, \tag{A.5}$$

where $\hat{\omega}$ is allowed to vary within the predefined range.

In this thesis PSO is used to perform viscoelastic characterization. Two different samples are investigated: One polymer blend consisting of polystyrene and polybutadiene (PS-PB) and one polymer blend consisting of Polystyrene and Polyolefin Elastomer (ethylene-octene copolymer) (PS-LDPE). In the experimental characterization procedure three points also known as pixels were investigated on a soft polybutadiene (PB) matrix: Pixel (144,37), (240,135) and (50,20). Two pixels were investigated on soft polyolefin elastomer (LDPE): Pixel (147,186) and (64,52). The moving surface model is used for characterization and includes 5 free variables. These variables exist in a large parameter range (see Appendix A.0.1) wherein the PSO algorithm needs to find the global minimum.

In the optimization an initial swarmsize containing 50 initial guesses is collected from a loguniform distribution within the specified large parameter range. For depicted pixels it is analyzed how many function evaluations are required to converge to a specified error E between the simulated best-fit and the experimental data. Fig. A.4 shows the convergence of E for increasing amount of function evaluations. Pixel (144,219) and (50,20) show a higher initial error E than pixel (240,135). After results for two pixels were obtained it was motivated to use the parameter set of the solution of pixel (50,20) as the initial swarm of the optimization procedure for pixel (240,135). This was done in order to speed up the optimization process using pre-knowledge of the already characterized material behavior in the other material regions. This reduced the required amount of function evaluations by 20 %.

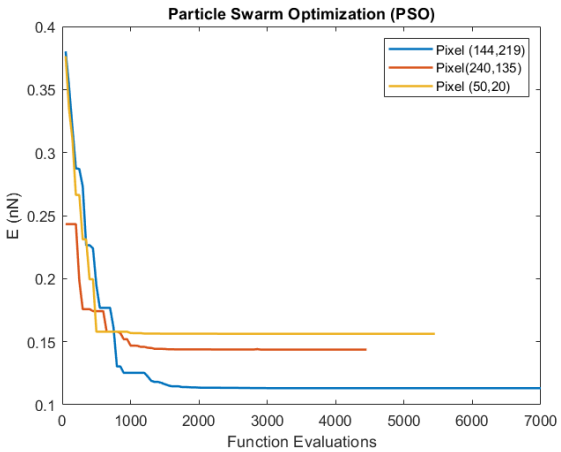

Figure A.4 Error analysis in PSO optimization used for viscoelastic characterization of three pixels on polybutadiene matrix. The error E represents the distinction between simulated best-fit and the experimental data. For each pixel it is shown how many objective function evaluations were required to get to the best-fit in the optimization.

Fig. A.5 shows the convergence of E for increasing amount of function evaluations for depicted pixels on LDPE sample.

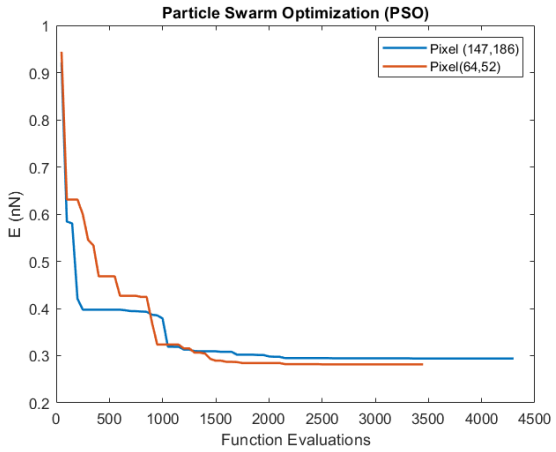

Figure A.5 Error analysis in PSO optimization used for viscoelastic characterization of three pixels on polyolefin elastomer. The error E represents the distinction between simulated best-fit and the experimental data. For each pixel it is shown how many objective function evaluations were required to get to the best-fit in the optimization.

A.1.2. Solution space reduction

In order to improve the efficiency and performance of the optimization it is of interest to reduce the solution space as much as possible. In this way the chance of finding the global minimum is increased and the required amount of function evaluations reduced. We present a strategy to extract the adhesion force F_{ad} of the moving surface model from an experiment.

As the amplitude of the modulated signal changes slow with respect to the eigenfrequency of the cantilever ω_0 we estimate that the tap at the first point of contact shows negligible indentation. Fig. A.6 shows how the first tap of the cantilver motion shows little indentation into the surface.

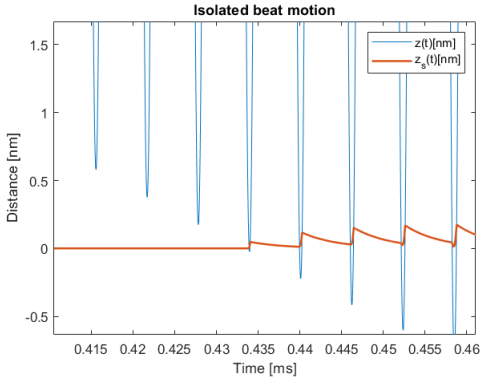

Figure A.6 Simulated cantilever z and surface motion z_s in ImAFM. The first point of contact is highlighted to show little indentation as a consequence of slow amplitude modulation of the tip motion.

At the point of first tap the interaction described by a Piecewise Linear (PWL) Force introduced in Appendix B can be simplified. For low indentation the difference between cantilever and surface position $s = z - z_s \approx 0$. Therefore, the PWL force can be rewritten such that:

$$F_{ts}(s,\dot{s}) = -F_{ad} - k_v s - \eta_v \dot{s} = -F_{ad} - \eta_v \dot{s}\,. \tag{A.6}$$

Since the velocity is $\pi/2$ out-of-phase with the displacement the contribution of $\eta_v \dot{d}$ will be redundant in the conservative force:

$$F_{ts,cons}(s) \approx -F_{ad}. \tag{A.7}$$

As a consequence, the interaction force during the first tap will be described by a short impulse with amplitude F_{ad} as depicted in Fig A.7b. However, the interaction force in the experiment coming from the intermodulation spectrum cannot describe this (see Fig. A.7a).

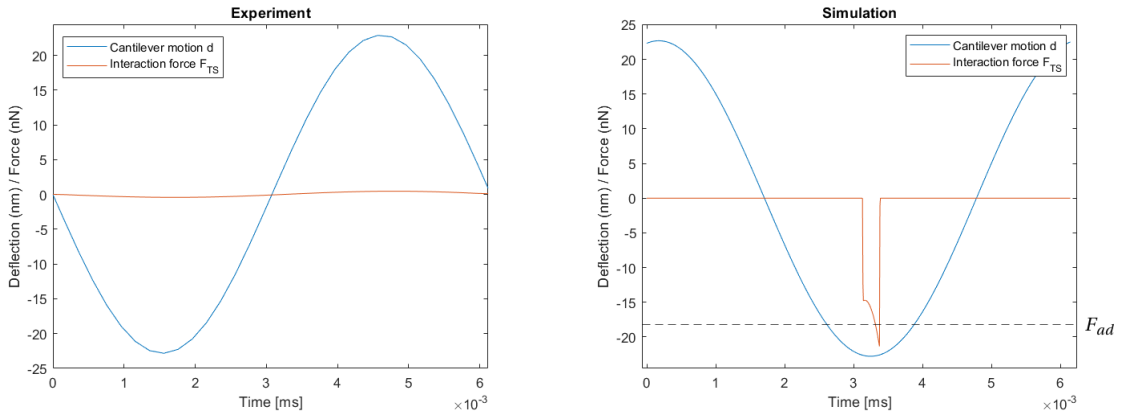

(a) Experimental oscillation cycle

(b) Simulated oscillation cycle

Figure A.7 Illustration of the interaction force and tip motion during the first oscillation cycle of contact. (a) Experimental force and deflection. (b) Simulated force and deflection showing an impusle with amplitude approximating the adhesion force F_{ad}.

Using the Force quadrature curves obtained in experiment and simulation, we are able to relate the adhesion force F_{ad} by determining the integral over the impulse of the interaction force. Assuming a square impulse with amplitude F_{ad} and duration $\hat{\delta}_h$ we define

$$F_I(A) = \frac{1}{T}\int_0^T F_{ts}(t)\frac{d}{A}dt \approx -F_{ad}\cdot\hat{\delta}_h\cdot\frac{min(d)}{A}\,, \tag{A.8}$$

such that

$$F_{ad} = -F_{I,\text{experiment}}(A=h)\cdot\frac{A}{\min(d)\hat{\delta}_h}. \tag{A.9}$$

Here we estimate the duration of the impulse to be shorter than 5% of the oscillation period. We assume a square force profile with area $\hat{\delta_h}\cdot\min(d)$ which is experimentally validated to show low error when $\hat{\delta_h}$ is chosen to be around 0.035 for different cantilevers. The variability in the square-impulse with amplitude F_{ad} assumption is directly related to the uncertainty in the estimation of Fad. This range of uncertainty of Fad can be translated into the total solution space of the variable. However, a thorough analysis is still needed to verify the solidity of the estimation procedure.

.

A.2. Experimental Characterization

In this research two different samples are investigated. One polymer blend consisting of polystyrene and polybutadiene (PS-PB) and one polymer blend consisting of Polystyrene and Polyolefin Elastomer (ethylene-octene copolymer) (PS-LDPE). Images of both samples have been obtained with intermodulation AFM (ImAFM) in AM-AFM mode.

Table A.2 shows the free parameters of the moving surface model that were found using PSO algorithm for a particular pixel on PB material. The cantilever and surface motion can be observed in Fig. A.8 (c)(d). A characteristic of the fitting parameters is that the retardation time $\tau_s = \eta_s / k_s$ is much larger than the slow-time period of the beat signal ($\tau_s >> 2\ ms$), which is why the surface maintains an average surface position smaller than zero. Fig. A.2 (d) demonstrates how standing surface waves occur on the slow time beat period of the cantilever tip.

Pixel	h (nm)	F_d (nN)	k_v (N/m)	k_s (N/m)	F_{ad} (nN)	η_v (mgs^{-1})	η_s (mgs^{-1})	Error E (nN)
(50, 20)	22.64	1.376	6.153	0.01273	12.27	0.5436	533.0	0.1567

Table A.2: Fitted parameters obtained using Particle Swarm Optimization (PSO) for three pixels on polybutadiene (PB) matrix. Where the driving force is indicated by the force component of the first drive frequency $F_d = |F_D^t(\omega_1)|$. The error E defines the error between the Force fourier components in the simulated best-fit and experiment, and hence, indicates the performance of the optimization.

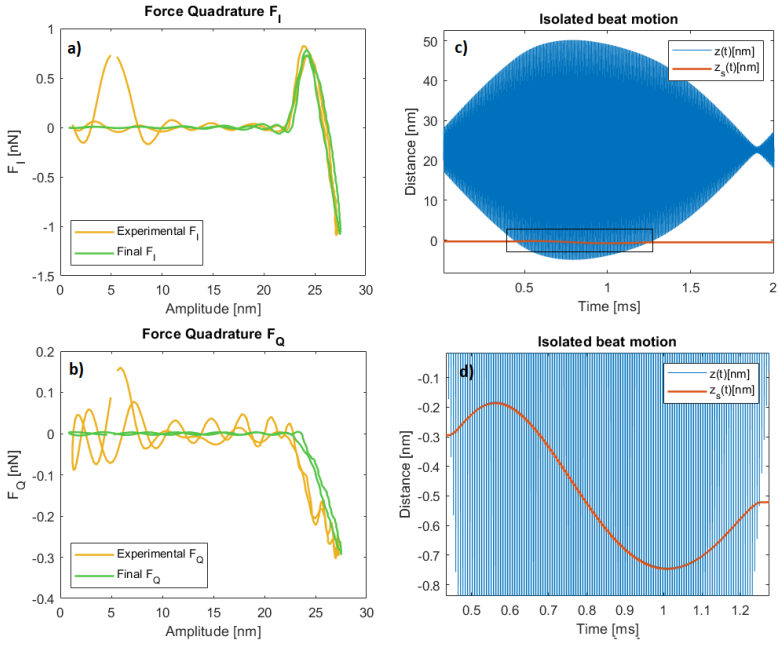

Figure A.8 Best-fit results for Pixel (50,20) with Error $E = 0.1567$ nN. Experimental observation of ***a***) In-phase force quadrature $F_I(A)$ describing conservative interaction. Experimental $F_I(A)$ plotted against the final $F_I(A)$ obtained in Particle Swarm Optimization (PSO) method. ***b***) Dissipative force quadratures $F_Q(A)$ obtained in experiment and final $F_Q(A)$ obtained in optimization. ***c***) The dynamics of the best-fit simulated tip-sample interaction, ***d***) zoomed in on the surface motion at the black square shown in ***c***). Sensitivity analysis for the characterized parameter set: $S_{k_v} = 1.39$, $S_{k_s} = 0.00060$, $S_{F_{ad}} = 1.2$, $S_{\eta_s} = 0.0063$ and $S_{\eta_v} = 0.30$.

B

Moving Surace Model

In AFM, the tip-sample interaction force is generally described in terms of one variable, i.e. the vertical tip position z. However, for soft viscoelastic samples surface rheology is significant, and hence, should also be taken into account in a model. Haviland et al. (2015) [13] showed that attractive forces already cause surface rheology before repulsive forces set in. Hence, in order to comprehend the viscoelastic response a proper analysis of both the cantilever dynamics and the surface dynamics is required. In the Moving surface model the instantaneous surface position is introduced as independent variable s [8], as can be seen in Fig. B.1. This variable is a one-dimensional spatially-averaged vertical position as alternative to a three-dimensional dynamics discription.

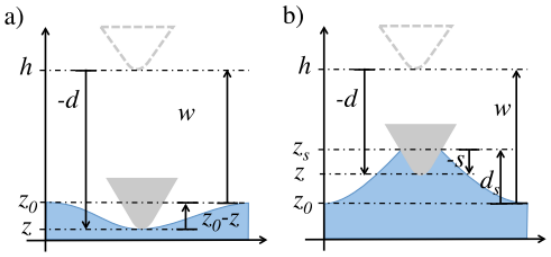

Figure B.1 Coordinates of moving surface model. The cantilever deflection $d = z - h$ is measured by the atomic force microscope detector, where $z(t)$ is the instantaneous tip position and the constant h is the equilibrium (zero force) tip position. z_0 is the equilibrium position of the sample surface. (a) The traditional view of contact forces in AFM has the tip and surface moving together when they are in contact, $z = z_s$, and interaction force is considered to be a function of the surface indentation $(z_0 - z)$. (b) The moving-surface model treats the surface position $z_s(t)$ as an independent dynamic variable. The model introduces elastic and viscous forces that depend on surface deflection $d_s = z_s - z_0$ and velocity $\dot{d}_s$, and an interaction force that depends on the separation $s = z - z_s$ and $\dot{s}$. Forces are balanced in the inertial reference frame where the cantilever has a fixed working distance to the sample, $w = h - z_0$. (Source: [8])

Haviland et al. (2016) proposes two different approaches for modelling of the tip-sample interaction force F_{ts}: a piecewise linear force model [8] and a nonlinear force model [13]. The tip-sample force couples the dynamics of the cantilever and the surface through the tip-surface seperation s. The cantilever and surface are both defined as harmonic oscillators:

$$\frac{1}{\omega_0^2}\ddot{d} + \frac{1}{Q\omega_0}\dot{d} + d = \frac{1}{k}F_{ts}(s,\dot{s}) + \frac{1}{k}F_{drive}(t), \tag{B.1}$$

$$\frac{1}{\omega_s^2}\ddot{d}_s + \frac{\eta_s}{k_s}\dot{d}_s + d_s = -\frac{1}{k_s}F_{ts}(s,\dot{s}), \tag{B.2}$$

where Eq.B.1 models the cantilever eigenmodes with parameters that can be independently calibrated and Eq.B.2 represents the surface dynamics with stiffness k_s and damping η_s. Assuming the surface mass to be

negligible [13], Eq.B.2 is translated into

$$\eta_s \dot{d}_s + k_s d_s = -F_{ts}(s, \dot{s}).,\tag{B.3}$$

Thoren et al. (2018) [8] represent the tip-sample interaction force F_{ts} as a Piecewise Linear (PWL) force:

$$F_{ts}(s, \dot{s}) = -F_{ad} - k_v s - \eta_v \dot{s},\tag{B.4}$$

with F_{ad} the adhesion force, η_v interaction damping and k_v a stiffness term describing bulk compression [8].

Using the intermodulation AFM (ImAFM) technique, the multifrequency response of the tip-sample interaction can directly be translated into amplitude-dependent force quadratures $F_I(A)$ and $F_Q(A)$. By analyzing the force quadrature properties it is possible to perceive the underlying tip-sample interaction in the experiment. A positive F_I implies the cantilever undergoes a prevalent attractive force during the single oscillation cycle, and negative F_I a represents prevalent repulsive force. Equivalently, a negative F_Q corresponds to dissipated energy in the single oscillation cycle of cantilever motion [13]. Moreover, a slow relaxation of the sample gives rise to hysteresis observed in the F_I and F_Q curves.

Fig. B.2a,b show dynamics of a simulation of the moving surface model, clearly illustrating a steady state surface position $z_s = 10$ nm occuring as a consequence of interplay between high surface-lift and fast retardation time. Fig. B.2c,d show the force quadratures indicating hysteretic, attractive and dissipative interaction characteristics.

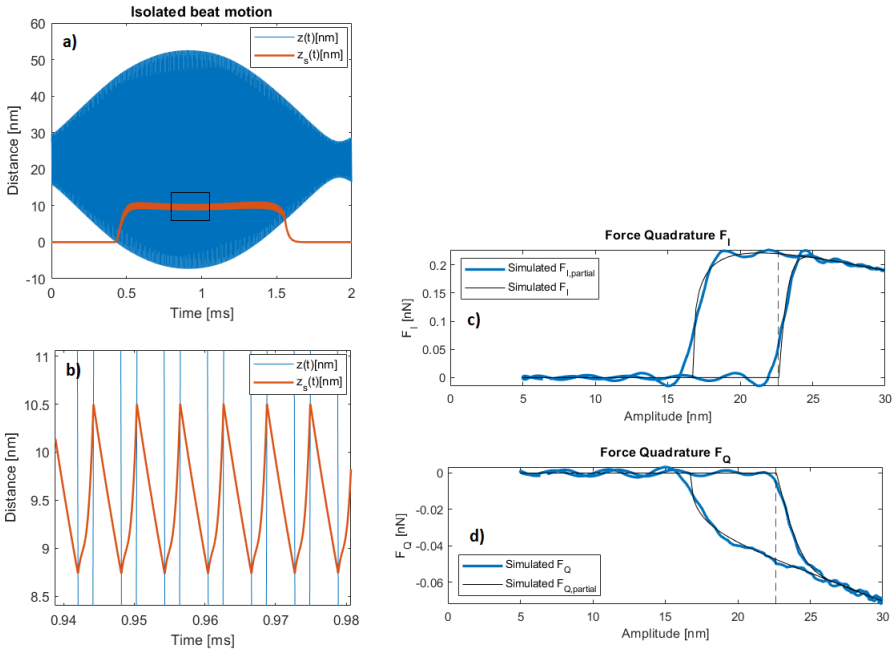

Figure B.2 Simulation of the moving surface model. (a) Dynamics of the tip-surface interaction. The cantilever position z and surface position z_s in time domain. (b) Focus on a time interval of the surface motion z_s indicated by square region in (a) representing a steady state surface elevation of approximately 10 nm. (c) In-phase force quadrature cruve $F_I(A)$ or Virial. (d) Dissipative force quadrature curve $F_Q(A)$. Model parameters used in simulation: $k_v = 0.034$, $k_s = 0.027$, $F_{ad} = 1.1$, $\eta_s = 0.58$ and $\eta_v = 0.018$.

C

Numerical modelling with Matlab

In this thesis multiple surface models have been incorporated and evaluated in the moving surface model. These models represent linear viscoelastic models such as Kelvin-Voigt, Standard Linear Solid (SLS) and the Generalized Maxwell model. Below are displayed state space descriptions where these models represent surface behavior the moving surface model. With these state space descriptions it is possible to perform numerical intergration to simulate model dynamics.

C.1. State Space models

C.1.0.1. Kelvin-Voigt, no mass

$$s > 0, \tag{C.1}$$

$$\dot{x}_1 = x_2 \tag{C.2}$$

$$\dot{x}_2 = -\frac{1}{Q}x_2 - x_1 + \frac{F_{drive}(t)}{kh} \tag{C.3}$$

$$\dot{x}_3 = -\frac{x_3}{u_s} \tag{C.4}$$

$$\dot{x}_4 = 0 \tag{C.5}$$

$$s \leq 0, \tag{C.6}$$

$$\dot{x}_1 = x_2 \tag{C.7}$$

$$\dot{x}_3 = \frac{\eta_s}{\eta_v + \eta_s}\left(\frac{-x_3}{u_s} + \frac{F_{ad}}{hk_s u_s} + \frac{k_v s}{u_s k_s} + \frac{\eta_v x_2}{\eta_s}\right) \tag{C.8}$$

$$\dot{x}_2 = -\frac{x_2}{Q} - x_1 - \frac{F_{ad}}{kh} - \frac{k_v s}{k} - \frac{u_v(x_2 - \dot{x}_3)kv}{k} + \frac{F_d}{kh} \tag{C.9}$$

$$\dot{x}_4 = -\frac{F_{ad}}{h} - k_v s - \eta_v \omega_0 (x_2 - \dot{x}_3) \tag{C.10}$$

$$\tag{C.11}$$

C.1.0.2. Smooth Kelvin-Voigt, no mass

$$\dot{x}_1 = x_2 \tag{C.12}$$
$$\dot{x}_2 = -\frac{1}{Q}x_2 - x_1 + \frac{F_{drive}(t)}{kh} \tag{C.13}$$
$$\dot{x}_3 = \left(\frac{1}{\eta_s} + \frac{\eta_v}{(exp(hs/s_0)+1)}\right)\left(\frac{k_v s/\omega_0 + \eta_v x_2 + F_{ad}/h/\omega_0}{exp(hs/s_0)+1} - \frac{k_s x_3}{\omega_0}\right) \tag{C.14}$$
$$\dot{x}_4 = (-\frac{F_{ad}}{h} - k_v s - \eta_v \omega_0 (x_2 - \dot{x}_3))/(1 + exp(hs/s_0)) \tag{C.15}$$
$$\tag{C.16}$$

C.1.0.3. Standard Linear Solid

The Standard Linear Solid model consists of two springs and one damper. Representing solid-like behavior, the model can be arranged in two ways. These variations are called Zener model and Poynting-Thomson model.

• Zener model

$$s_d = x_2 - x_4 \tag{C.17}$$
$$s > 0, \tag{C.18}$$
$$\dot{x}_1 = x_2 \tag{C.19}$$
$$\dot{x}_2 = -\frac{1}{Q}x_2 - x_1 + \frac{F_{drive}(t)}{kh} \tag{C.20}$$
$$\dot{x}_3 = \frac{-k_{s1}k_{s2}x_3}{\eta_s(k_{s1}+k_{s2})\omega_0} \tag{C.21}$$
$$\dot{x}_4 = \frac{-k_{s1}k_{s2}\dot{x}_3}{\eta_s(k_{s1}+k_{s2})\omega_0} \tag{C.22}$$
$$\dot{x}_5 = 0 \tag{C.23}$$
$$s \leq 0, \tag{C.24}$$
$$\dot{x}_1 = x_2 \tag{C.25}$$
$$\dot{x}_2 = -\frac{1}{Q}x_2 - x_1 + \frac{F_{drive}(t)}{kh} \tag{C.26}$$
$$\dot{x}_3 = x_4 \tag{C.27}$$
$$\dot{x}_4 = \frac{k_v k_{s2} s}{\eta_v \eta_s \omega_0^2} + \frac{k_{s2} s_d}{\eta_s \omega_0} + \frac{F_{ad} k_{s2}}{\eta_v \eta_s h \omega_0^2} + \frac{k_v s_d}{\eta_v \omega_0} + \dot{x}_2 - \frac{k_{s2}k_{s1}x_3}{\eta_s \eta_v \omega_0^2} - \frac{k_{s2}x_4}{\eta_v \omega_0} - \frac{k_{s1}x_4}{\eta_v \omega_0} \tag{C.28}$$
$$\dot{x}_5 = -\frac{F_{ad}}{h} - k_v s - \eta_v \omega_0 s_d \tag{C.29}$$

• Poynting-Thomson model

$$s_d = x_2 - x_4 \tag{C.30}$$
$$s > 0, \tag{C.31}$$
$$\dot{x}_1 = x_2 \tag{C.32}$$
$$\dot{x}_2 = -\frac{1}{Q}x_2 - x_1 + \frac{F_{drive}(t)}{kh} \tag{C.33}$$
$$\dot{x}_3 = \frac{-k_{s2}x_3}{\eta_s \omega_0} \tag{C.34}$$
$$\dot{x}_4 = \frac{-k_{s2}\dot{x}_3}{\eta_s \omega_0} \tag{C.35}$$
$$\dot{x}_5 = 0 \tag{C.36}$$
$$s \leq 0, \tag{C.37}$$
$$\dot{x}_1 = x_2 \tag{C.38}$$
$$\dot{x}_2 = -x_2/Q - x_1 - \frac{F_{ad}}{kh} - \frac{k_v s}{k} - \frac{\eta_v s_d}{m\omega_0} + \frac{F_{drive}(t)}{kh} \tag{C.39}$$
$$\dot{x}_3 = x_4 \tag{C.40}$$
$$\dot{x}_4 = \frac{k_{s1}+k_{s2}}{\eta_s \eta_v}\left(\frac{k_v s}{\omega_0^2} + \frac{\eta_v s_d}{\omega_0} + \frac{F_{ad}}{h\omega_0^2} + \frac{\eta_s k_v s_d}{(k_{s1}+k_{s2})\omega_0} + \frac{\eta_s \eta_v \dot{x}_2}{k_{s1}+k_{s2}} - \frac{k_{s1}k_{s2}x_3}{(k_{s1}+k_{s2})\omega_0^2} - \frac{k_{s1}\eta_s x_4}{(k_{s1}+k_{s2})\omega_0}\right) \tag{C.41}$$
$$\dot{x}_5 = -\frac{F_{ad}}{h} - k_v s - \eta_v \omega_0 s_d \tag{C.42}$$

The Zener (Z) model and Poynting-Thomson (PT) model are equivalent when the following conditions hold [61]:

$$k_{s1,\,\mathrm{PT}} = k_{s1,\,\mathrm{Z}} + k_{s2,\,\mathrm{Z}} \tag{C.43}$$
$$k_{s2,\,\mathrm{PT}} = k_{s1,\,\mathrm{Z}}\left(1 + \frac{k_{s1,\,\mathrm{PT}}}{k_{s2,\,\mathrm{Z}}}\right) \tag{C.44}$$
$$\eta_{s,\,\mathrm{PT}}\, k_{s2,\,\mathrm{Z}}\, k_{s1,\,\mathrm{Z}} = \eta_{s,\,\mathrm{Z}}\, k_{s2,\,\mathrm{PT}}\, k_{s1,\,\mathrm{PT}} \tag{C.45}$$

C.1.0.4. Generalized Maxwel (GM2) - Wiechert Model

Following Zerpa et al. (2015) we define short-hand notations:

- $\tau_1 = \frac{\eta_{s1}}{k_{s1}}$, $\tau_2 = \frac{\eta_{s2}}{k_{s2}}$, $\alpha_1 = \frac{\eta_{s1}}{k_{s0}}$, $\alpha_2 = \frac{\eta_{s2}}{k_{s0}}$,
- $\nu_1 = \tau_1 + \tau_2 + \alpha_1 + \alpha_2$, $\nu_2 = \tau_1\tau_2 + \alpha_1\tau_2 + \alpha_2\tau_1$,
- $\chi_1 = \tau_1 + \tau_2$, $\chi_2 = \tau_1\tau_2$.

Such that:

$s > 0$, (C.46)

$$\dot{x}_1 = x_2 \tag{C.47}$$

$$\dot{x}_2 = -\frac{x_2}{Q} - x_1 - \frac{F_{ad}}{kh} - \frac{k_v s}{k} - \frac{\eta_v \dot{s}}{m\omega_0} + \frac{F_{drive}(t)}{kh} \tag{C.48}$$

$$\dot{x}_3 = -\frac{x_3}{Q} - x_2 - \frac{k_v \dot{s}}{k} - \frac{\eta_v \ddot{s}}{m\omega_0} + \frac{\dot{F}_{drive}(t)}{kh} \tag{C.49}$$

$$\dot{x}_4 = x_5 \tag{C.50}$$

$$\dot{x}_5 = x_6 \tag{C.51}$$

$$\dot{x}_6 = \dot{x}_3 + \frac{k_v}{\eta_v \omega_0}(\dot{x}_2 - x_6) + \frac{\chi_1}{\chi_2}\left(\frac{k_v}{\eta_v \omega_0^2}\dot{s} + \frac{(\dot{x}_2 - x_6)}{\omega_0}\right) + \frac{1}{\chi_2}\left(\frac{F_{ad}}{\eta_v h \omega_0^3} + \frac{\dot{s}}{\omega_0^2} + \frac{k_v}{\eta_v \omega_0^3}s - \frac{k_{s0}}{\eta_v \omega_0^3}x_4 - \frac{k_{s0}\nu_1}{\eta_v \omega_0^2}x_5 - \frac{k_{s0}\nu_2}{\eta_v \omega_0}x_6\right) \tag{C.52}$$

$s \leq 0$, (C.53)

$$\dot{x}_1 = x_2 \tag{C.54}$$

$$\dot{x}_2 = -\frac{1}{Q}x_2 - x_1 + \frac{F_{drive}(t)}{kh} \tag{C.55}$$

$$\dot{x}_3 = -\frac{\dot{x}_2}{Q - x_2} - \frac{\dot{F}_{drive}(t)}{kh} \tag{C.56}$$

$$\dot{x}_4 = x_5 \tag{C.57}$$

$$\dot{x}_5 = -\frac{\nu_1 x_5}{\nu_2 \omega_0} - \frac{x4}{\nu_2 \omega_0^2} \tag{C.58}$$

$$\dot{x}_6 = -\frac{\nu_1 \dot{x}_5}{\nu_2 \omega_0} - \frac{x_5}{\nu_2 \omega_0^2} \tag{C.59}$$

(C.60)

C.1.1. ODE Solver speed

Initially MATLAB's general purpose non-stiff solver known as ode45 was employed for the numerical integration of the state space models. However, as the variability in timescale can be significant in the moving surface model it was motivated to investigate the performance of the more stiff branch of basic solvers as well. Table C.1 shows the achievements of all basic solvers.

		Succesful steps	Failed attempts	Function evaluations	Elapsed time (s)
Nonstiff	ode45	32967	4078	222271	5.842
	ode23	272395	4128	8.260e5	26.72
	ode113	39184	9281	8.765e4	24.13
Stiff	ode15s	68029	5639	137337	25.13
	ode23s	341562	4654	2.744e6	108.7
	ode23t	497836	2807	5.066e5	65.20
	ode23tb	372033	4198	8.109e5	41.74

Table C.1: ODE Solver performance

ode45 shows to be the quickest solver available. The speed is rather important as the duration of the optimization is highly dependent on the simulation time. It was found that oftentimes when values of the surface damping parameter $\eta_s < 10^{-8}$ the simulation time of the solver increased significantly. A second important notion is that the amount of failed attempts for all solvers is substantial. This can be attribiuted to the inherent non-smoothness of the moving surface model.

Following Nyquist-Shannon sampling Theorem the frequency of steps in the numerical integration should at least be higher than twice the largest frequency of interest. However, in order to reduce simulation time it is attempted to limit the number of steps whithout losing valuable information. The limiting factor appeared to be the inherent non-smooth tip-sample force showing errors larger than 1nN below a step frequency 150 MHz ($\approx 1000 \cdot f_0$), as is indicated in Fig. C.1. However, it is more relevant to evaluate the error in the tip-sample force spectrum $\hat{F}_{ts}(\omega)$ as this is employed for force reconstruction. The least-square error E is evaluated with respect to the ideal shape achieved with highest frequency $5000 \cdot f_0$. The minimum error obtained by Daniel Forchheimer [11] in experimental force reconstruction performed on PS-LDPE sample amounts 0.172 nN. As those values were presented with 3 significant numbers it was chosen to use a frequency $\geq 250 f_0$, including an inherent error less than 1e-3 nN.

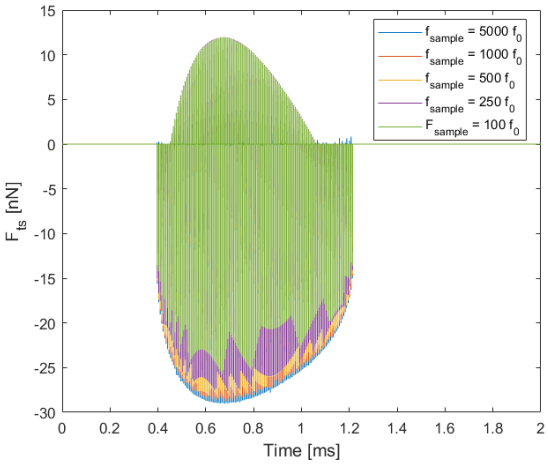

Figure C.1: Effect of sampling frequency on interaction force in numerical integration.

	Error E (nN)	Time (s)
$1000 f_0$	3.6417e-04	13.03
$500 f_0$	6.6285e-04	9.290
$250 f_0$	0.004	7.861
$100 f_0$	0.0113	7.114

Table C.2: Least-square Errors and duration of the numerical simulations

Since in the optimization non-smoothness was occasionally found in the objective function as well, the smoothening effect of the sigmoid or logarithmic function [12] became of interest. Using a logartihmic function the PWL force can be rewritten as:

$$F_{ts}(s, s_0) = S(s, s_0) \cdot \left(-k_v s - \eta_v \dot{s} - F_{ad}\right), \tag{C.61}$$

where

$$S(s, s_0) = \frac{1}{e^{\frac{s}{s_0}} + 1}. \tag{C.62}$$

Using the smooth PWL-model it was evaluated for what values of s_0 convergence occured to a small eror E: Again with respect to frequency components of a normal simulation with highest accuracy $5000 f_0$. Fig. C.2 shows this convergence for 5 different parameter sets. Representative behavior occurs after $s_0 = 10^{-10}$, however at this point the amount of failed attempts in the numerical iteration has already reached same orders of magnitude as values presented in Table C.1.

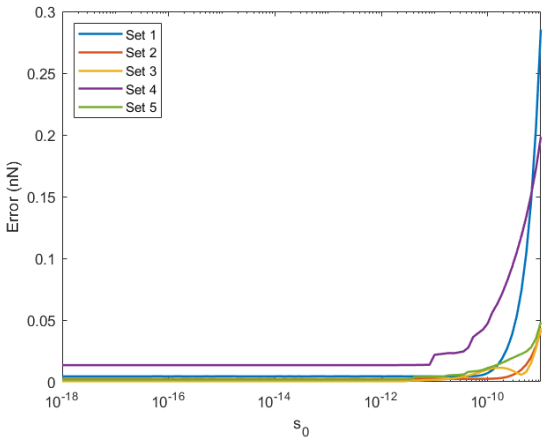

Figure C.2 Convergence of Error E between expensive simulation and simulation incorporating a smooth transition. For decreasing smoothness parameter s_0 in numerical simulations, the error is analyzed.

Bibliography

[1] Yves F Dufrêne, Toshio Ando, Ricardo Garcia, David Alsteens, David Martinez-Martin, Andreas Engel, Christoph Gerber, and Daniel J Müller. Imaging modes of atomic force microscopy for application in molecular and cell biology. *Nature nanotechnology*, 12(4):295, 2017.

[2] Yuri M Efremov, Takaharu Okajima, and Arvind Raman. Measuring viscoelasticity of soft biological samples using atomic force microscopy. *Soft matter*, 2020.

[3] Hui Huang, Illia Dobryden, P-A Thorén, Lina Ejenstam, Jinshan Pan, ML Fielden, DB Haviland, and Per Martin Claesson. Local surface mechanical properties of pdms-silica nanocomposite probed with intermodulation afm. *Composites Science and Technology*, 150:111–119, 2017.

[4] Gerd Binnig, Calvin F Quate, and Ch Gerber. Atomic force microscope. *Physical review letters*, 56(9):930, 1986.

[5] Stephen Jesse, Sergei V Kalinin, Roger Proksch, AP Baddorf, and BJ Rodriguez. The band excitation method in scanning probe microscopy for rapid mapping of energy dissipation on the nanoscale. *Nanotechnology*, 18(43):435503, 2007.

[6] Ricardo Garcia and Elena T Herruzo. The emergence of multifrequency force microscopy. *Nature nanotechnology*, 7(4):217, 2012.

[7] Daniel Platz, Erik A Tholén, Devrim Pesen, and David B Haviland. Intermodulation atomic force microscopy. *Applied Physics Letters*, 92(15):153106, 2008.

[8] Per-Anders Thorén, Riccardo Borgani, Daniel Forchheimer, Illia Dobryden, Per M Claesson, Hailu G Kassa, Philippe Leclère, Yifan Wang, Heinrich M Jaeger, and David B Haviland. Modeling and measuring viscoelasticity with dynamic atomic force microscopy. *Physical Review Applied*, 10(2):024017, 2018.

[9] Bahram Rajabifar, Jyoti M Jadhav, Daniel Kiracofe, Gregory F Meyers, and Arvind Raman. Dynamic afm on viscoelastic polymer samples with surface forces. *Macromolecules*, 2018.

[10] Daniel Platz. *Reconstructing force from harmonic motion*. PhD thesis, KTH Royal Institute of Technology, 2013.

[11] Daniel Forchheimer. *Imaging materials with intermodulation: Studies in multifrequency atomic force microscopy*. PhD thesis, KTH Royal Institute of Technology, 2015.

[12] Per-Anders Thorén. *Investigating nano-scale viscous and elastic forces withintermodulation: Studies in multifrequency atomic force microscopy*. PhD thesis, KTH Royal Institute of Technology, 2018.

[13] David B Haviland, Cornelius Anthony van Eysden, Daniel Forchheimer, Daniel Platz, Hailu G Kassa, and Philippe Leclère. Probing viscoelastic response of soft material surfaces at the nanoscale. *Soft matter*, 12 (2):619–624, 2015.

[14] JPK Instruments. *Nanowizard AFM Hanbook*, volume Version 6.0. JPK Instruments, 2018.

[15] Brunero Cappella and Giovanni Dietler. Force-distance curves by atomic force microscopy. *Surface science reports*, 34(1-3):1–104, 1999.

[16] Franz J Giessibl. Advances in atomic force microscopy. *Reviews of modern physics*, 75(3):949, 2003.

[17] Werner A Hofer, Adam S Foster, and Alexander L Shluger. Theories of scanning probe microscopes at the atomic scale. *Reviews of Modern Physics*, 75(4):1287, 2003.

[18] Ricardo Garcıa and Ruben Perez. Dynamic atomic force microscopy methods. *Surface science reports*, 47(6-8):197–301, 2002.

[19] Thomas Stifter, Othmar Marti, and Bharat Bhushan. Theoretical investigation of the distance dependence of capillary and van der waals forces in scanning force microscopy. *Physical Review B*, 62(20): 13667, 2000.

[20] Franz J Giessibl. Forces and frequency shifts in atomic-resolution dynamic-force microscopy. *Physical Review B*, 56(24):16010, 1997.

[21] Yoshiaki Sugimoto, Pablo Pou, Masayuki Abe, Pavel Jelinek, Rubén Pérez, Seizo Morita, and Oscar Custance. Chemical identification of individual surface atoms by atomic force microscopy. *Nature*, 446 (7131):64, 2007.

[22] R. Reifenberger. Fundamentals of atomic force microscopy, part 1: Fundamental aspects of afm. https://nanohub.org/courses/AFM1/. Accessed: 2019-02-7.

[23] Daniel Kiracofe, John Melcher, and Arvind Raman. Gaining insight into the physics of dynamic atomic force microscopy in complex environments using the veda simulator. *Review of Scientific Instruments*, 83(1):013702, 2012.

[24] Kenneth Langstreth Johnson, Kevin Kendall, and AD Roberts. Surface energy and the contact of elastic solids. *Proc. R. Soc. Lond. A*, 324(1558):301–313, 1971.

[25] D Tabor. Surface forces and surface interactions. In *Plenary and Invited Lectures*, pages 3–14. Elsevier, 1977.

[26] Daniel Maugis. Adhesion of spheres: the jkr-dmt transition using a dugdale model. *Journal of colloid and interface science*, 150(1):243–269, 1992.

[27] KL Johnson and JA Greenwood. An adhesion map for the contact of elastic spheres. *Journal of colloid and interface science*, 192(2):326–333, 1997.

[28] Dewei Xu, Kenneth M Liechti, and K Ravi-Chandar. On the modified tabor parameter for the jkr–dmt transition in the presence of a liquid meniscus. *Journal of colloid and interface science*, 315(2):772–785, 2007.

[29] Andong He and John S Wettlaufer. Hertz beyond belief. *Soft matter*, 10(13):2264–2269, 2014.

[30] David B Haviland. Quantitative force microscopy from a dynamic point of view. *Current Opinion in Colloid & Interface Science*, 27:74–81, 2017.

[31] Ronald G Reifenberger. *Fundamentals of Atomic Force Microscopy: Part I: Foundations*. World Scientific Publishing Company Pte Limited, 2016.

[32] A. Raman. Fundamentals of atomic force microscopy, part 2: Dynamic afm methods. https://nanohub.org/courses/AFM2/. Accessed: 2019-02-7.

[33] Riccardo Borgani, Per-Anders Thorén, Daniel Forchheimer, Illia Dobryden, Si Mohamed Sah, Per Martin Claesson, and David B Haviland. Background-force compensation in dynamic atomic force microscopy. *Physical Review Applied*, 7(6):064018, 2017.

[34] Jose R Lozano and Ricardo Garcia. Theory of multifrequency atomic force microscopy. *Physical Review Letters*, 100(7):076102, 2008.

[35] Daniel Platz, Daniel Forchheimer, Erik A Tholén, and David B Haviland. Interaction imaging with amplitude-dependence force spectroscopy. *Nature communications*, 4:1360, 2013.

[36] Junuthula Narasimha Reddy. *An introduction to continuum mechanics*. Cambridge university press, 2013.

[37] Roderic S Lakes. *Viscoelastic solids*, volume 9. CRC press, 1998.

[38] Ian Macmillan Ward and John Sweeney. *An introduction to the mechanical properties of solid polymers*. John Wiley & Sons, 2004.

[39] William W Graessley. Viscoelastic properties of entangled flexible polymers. In *Faraday Symposia of the Chemical Society*, volume 18, pages 7–27. Royal Society of Chemistry, 1983.

[40] David Roylance. Engineering viscoelasticity. *Department of Materials Science and Engineering–Massachusetts Institute of Technology, Cambridge MA*, 2139:1–37, 2001.

[41] Abhijit P. Deshpande. Rheology of complex materials. https://onlinecourses.nptel.ac.in/noc18_ch07/preview. Accessed: 2019-02-7.

[42] Kwang Soo Cho. *Viscoelasticity of Polymers: Theory and Numerical Algorithms*, volume 241. Springer Series in Materials Science, 2016.

[43] Críspulo Gallegos and FJ Martínez-Boza. Linear viscoelasticity. *Rheology: encyclopaedia of life support systems (EOLSS), UNESCO. Eolss, Oxford*, pages 120–143, 2010.

[44] Bernhard Gross. *Mathematical structure of the theories of viscoelasticity*, volume 1190. Hermann, 1953.

[45] Marius Chyasnavichyus, Seth L Young, and Vladimir V Tsukruk. Probing of polymer surfaces in the viscoelastic regime. *Langmuir*, 30(35):10566–10582, 2014.

[46] Phil Attard. Measurement and interpretation of elastic and viscoelastic properties with the atomic force microscope. *Journal of Physics: Condensed Matter*, 19(47):473201, 2007.

[47] Noriaki Oyabu, Pablo Pou, Yoshiaki Sugimoto, Pavel Jelinek, Masayuki Abe, Seizo Morita, Rubén Pérez, and Oscar Custance. Single atomic contact adhesion and dissipation in dynamic force microscopy. *Physical review letters*, 96(10):106101, 2006.

[48] R Garcia, CJ Gómez, NF Martinez, Shivprasad Patil, Christian Dietz, and R Magerle. Identification of nanoscale dissipation processes by dynamic atomic force microscopy. *Physical review letters*, 97(1): 016103, 2006.

[49] Santiago D Solares. Nanoscale effects in the characterization of viscoelastic materials with atomic force microscopy: coupling of a quasi-three-dimensional standard linear solid model with in-plane surface interactions. *Beilstein journal of nanotechnology*, 7:554, 2016.

[50] Dalia G Yablon, Jean Grabowski, and Ishita Chakraborty. Measuring the loss tangent of polymer materials with atomic force microscopy based methods. *Measurement Science and Technology*, 25(5):055402, 2014.

[51] Enrique A López-Guerra and Santiago D Solares. Modeling viscoelasticity through spring–dashpot models in intermittent-contact atomic force microscopy. *Beilstein journal of nanotechnology*, 5:2149, 2014.

[52] Alvaro San Paulo and Ricardo Garcia. Amplitude, deformation and phase shift in amplitude modulation atomic force microscopy: a numerical study for compliant materials. *Surface science*, 471(1-3):71–79, 2001.

[53] EH Lee and Jens Rainer Maria Radok. The contact problem for viscoelastic bodies. *Journal of Applied Mechanics*, 27(3):438–444, 1960.

[54] TCT Ting. The contact stresses between a rigid indenter and a viscoelastic half-space. *Journal of Applied Mechanics*, 33(4):845–854, 1966.

[55] Phil Attard. Interaction and deformation of elastic bodies: origin of adhesion hysteresis. *The Journal of Physical Chemistry B*, 104(45):10635–10641, 2000.

[56] Phil Attard and John L Parker. Deformation and adhesion of elastic bodies in contact. *Physical Review A*, 46(12):7959, 1992.

[57] Magnus Erik Hvass Pedersen. *Tuning & simplifying heuristical optimization*. PhD thesis, University of Southampton, 2010.

[58] Arvind Raman, S Trigueros, A Cartagena, APZ Stevenson, M Susilo, E Nauman, and S Antoranz Contera. Mapping nanomechanical properties of live cells using multi-harmonic atomic force microscopy. *Nature nanotechnology*, 6(12):809, 2011.

[59] Stanislav S Borysov, Daniel Platz, Astrid S de Wijn, Daniel Forchheimer, Eric A Tolén, Alexander V Balatsky, and David B Haviland. Reconstruction of tip-surface interactions with multimodal intermodulation atomic force microscopy. *Physical Review B*, 88(11):115405, 2013.

[60] Daniel Forchheimer, Robert Forchheimer, and David B Haviland. Improving image contrast and material discrimination with nonlinear response in bimodal atomic force microscopy. *Nature communications*, 6:6270, 2015.

[61] Herbert Kolsky. *Stress waves in solids*, volume 1098. Courier Corporation, 1963.